

# MODELING OF LIQUID SLOSH AND CAVITATION IN AUTOINJECTORS

by

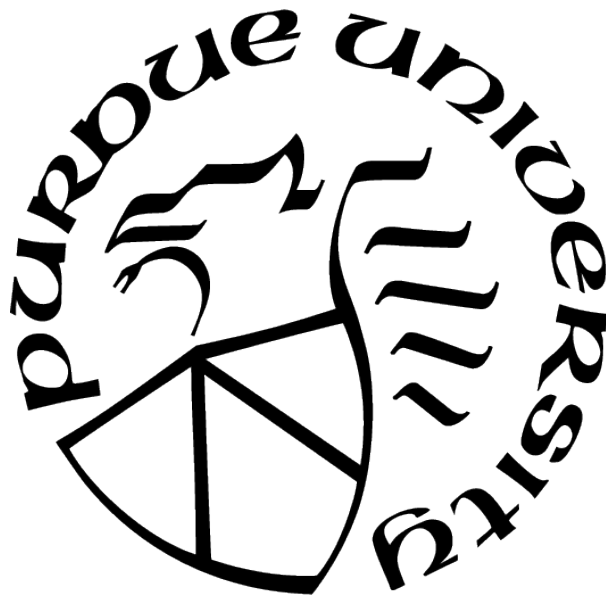
Yuchen Zhang

A Dissertation

*Submitted to the Faculty of Purdue University*

*In Partial Fulfillment of the Requirements for the degree of*

**Doctor of Philosophy**



School of Mechanical Engineering

West Lafayette, Indiana

May 2021

**THE PURDUE UNIVERSITY GRADUATE SCHOOL  
STATEMENT OF COMMITTEE APPROVAL**

**Dr. Arezoo M. Ardekani, Chair**

School of Mechanical Engineering

**Dr. Pavlos P. Vlachos**

School of Mechanical Engineering

**Dr. Hector Gomez**

School of Mechanical Engineering

**Dr. Sadegh Dabiri**

School of Agricultural and Biological Engineering

**Approved by:**

Dr. Nicole L. Key

## ACKNOWLEDGMENTS

First and foremost, I would like to thank my supervisor, Arezoo M. Ardekani, who has actively helped my research and provided important feedback for my dissertation. She is patient in correcting my mistakes and insightful in discovering new research topics. She has also provided me with the resources required to complete the work and established the collaboration with other research groups. With her support and help, I am able to become an independent researcher and explore the interesting phenomena in fluid dynamics and autoinjectors. I also would like to express my gratitude to the rest of my thesis committee, Professors Sadegh Dabiri, Pavlos P. Vlachos, and Hector Gomez.

I am also grateful to Eli Lilly and Company and National Science Foundation for their financial support of my research. Eli Lilly and Company has provided the opportunities for teamwork among several research teams, which led to our investigation of the fluid dynamics of autoinjectors.

Last and not least, I express my special thanks to Dr. Zhongwang Dou, and Tianqi Guo, who worked on the experimental part of the current research. We also exchanged ideas and had fruitful discussions on the research related to autoinjectors.

# TABLE OF CONTENTS

LIST OF TABLES . . . . .	7
LIST OF FIGURES . . . . .	8
ABSTRACT . . . . .	15
1 INTRODUCTION . . . . .	17
1.1 Motivation: trends of autoinjectors . . . . .	17
1.2 Concern of protein aggregation in autoinjectors . . . . .	19
1.3 Jet formation and liquid slosh induced during the insertion process . . . . .	21
1.4 Cavitation at the start of the insertion process . . . . .	21
2 VELOCITY SCALING AND BREAKUP CRITERIA FOR JETS FORMED DUE TO ACCELERATION AND DECELERATION PROCESS . . . . .	23
2.1 summary . . . . .	23
2.2 Introduction . . . . .	24
2.3 Method . . . . .	26
2.3.1 Experimental Setup . . . . .	26
2.3.2 Numerical Method . . . . .	27
2.4 Results . . . . .	30
2.4.1 Experimental validation of numerical simulations . . . . .	30
2.4.2 Jet formation process . . . . .	31
2.4.3 Effects of the time of acceleration and deceleration process . . . . .	33
2.4.4 Scaling laws for the jet velocity . . . . .	36
2.4.5 Effects of gravity . . . . .	38
2.4.6 Criteria for jet breakup . . . . .	44
2.5 Conclusion . . . . .	47
3 THE INTERFACE MOTION AND HYDRODYNAMIC SHEAR OF THE LIQUID SLOSH IN SYRINGES . . . . .	49

3.1	Summary . . . . .	49
3.2	Introduction . . . . .	50
3.3	Method . . . . .	53
3.3.1	Experimental Setup . . . . .	53
3.3.2	Numerical model . . . . .	53
3.3.3	Simulation setup for slosh dynamics in syringes . . . . .	55
3.4	Results and discussions . . . . .	58
3.4.1	Validation against Rayleigh-Taylor instability . . . . .	58
3.4.2	Simulation results for different mesh resolutions . . . . .	59
3.4.3	Comparison with experiments . . . . .	60
3.4.4	Investigation of interface area and strain rate . . . . .	61
3.4.5	Distribution of the strain rate and the flow type . . . . .	71
3.4.6	Analysis of invariants of the rate-of-strain and rate-of-rotation tensors . . . . .	73
3.5	Discussion: effects of slosh on drug . . . . .	77
3.6	Conclusions . . . . .	81
4	MODELING CAVITATION BUBBLE DYNAMICS AND ITS IMPLICATION TO PROTEIN MOLECULES . . . . .	83
4.1	Summary . . . . .	83
4.2	Introduction . . . . .	83
4.3	Method . . . . .	88
4.3.1	Problem Definition . . . . .	88
4.3.2	Ex-situ experiment . . . . .	91
4.3.3	One-dimensional equation for bubble dynamics . . . . .	93
4.3.4	Axisymmetric and 3D simulations of bubble collapse . . . . .	95
4.4	Results . . . . .	97
4.4.1	Validation against experiments using axisymmetric simulations . . . . .	97
4.4.2	1D calculation of bubble dynamics . . . . .	100
4.4.3	Mesh dependence of axisymmetric simulations . . . . .	103
4.4.4	Axisymmetric simulation for a non-spherical collapse . . . . .	105

4.4.5	3D simulations of bubble dynamics . . . . .	111
4.5	Discussion . . . . .	114
4.5.1	Implication to drug molecules . . . . .	114
4.6	Conclusion . . . . .	116
5	SUMMARY AND FUTURE WORK . . . . .	119
5.1	Overview . . . . .	119
5.2	Liquid jet due to acceleration-deceleration motion . . . . .	119
5.3	Liquid slosh . . . . .	120
5.4	Cavitation . . . . .	120
5.5	Mitigation . . . . .	121
5.6	Future work . . . . .	122
	REFERENCES . . . . .	124
	VITA . . . . .	134
	PUBLICATIONS . . . . .	135

## LIST OF TABLES

3.1	Parameters for the baseline simulation . . . . .	63
4.1	Parameters and fluid properties in the current work. . . . .	90
4.2	Non-dimensionalization in the 1D calculation. . . . .	93

## LIST OF FIGURES

1.1	Self-injection therapies and devices reproduced with the permission from ref. [2]	17
1.2	(a) Structure of a spring-driven autoinjector. (b) The motion of each component during the subcutaneous administration. The figures are produced with the permission from ref. [6]. . . . .	18
2.1	(a) A schematic of the experimental setup. The working fluid (Sigma-Aldrich 317667 silicone oil, viscosity 5 cSt, surface tension 20 mN/m, density 913 kg/m <sup>3</sup> ) is completely wetting with the glass tube. . . . .	26
2.2	The displacement (left), velocity (middle) and acceleration (right) of the tube for three different spring compressions with We corresponding to 348 (top), 505 (middle), and 799 (bottom). . . . .	28
2.3	The interface velocity at the tube center is independent of (a) the max CFL in the simulation, (b) the density ratio between the liquid and gas $\rho_l/\rho_g$ and (c) the viscosity ratio between the liquid and gas $\mu_l/\mu_g$ . Here, Bo = 0, Oh = 0.001, We = 1000, $\tau_d = 2$ , $\tau_a = 0.1$ . . . . .	29
2.4	(a) Comparison of surface profiles between experimental and numerical (red line) results for two Weber numbers. The jet breaks up for We = 799, but does not for We = 505. Dimensionless time $\tau = tU/R$ is denoted at the top of each frame. (b) Time evolution of the jet height $h_j$ from simulations and experiments. $h_j$ is defined as the interface height at the center of the tube, and the initial jet height is set to zero. The experimental data for small jet height is missing because the jet is inside a cavity and is not visible in images. For We = 348, 505, and 799, $\tau_d$ are 1.57, 1.47 and 1.46, respectively, and $\tau_a$ are 0.21, 0.25 and 0.33, respectively. Bo = 14.5. Viscosity ratio between inner and outer outer fluids in simulations is 50 which is about 5 times smaller than that in experiments. Here, Oh = 0.014. . . . .	30
2.5	(a) The time evolution of the liquid-gas interface. Dashed lines show the streamlines at $\tau = 3$ . The color bar indicates the time corresponding to different profiles. (b) The corresponding time evolution of the velocity field in the liquid jet. The time is annotated at the top of each frame. The scale of the velocity vector is denoted by the arrow on the right. Here, Oh = 0.014, We = 2000, $\tau_d = 2$ , $\tau_a = 0.1$ and Bo = 0. (c) The interface velocity at the tube center $V$ is independent of the refined grid size near the liquid-gas interface $\Delta x$ . Here, Oh = 0.014, We = 1000, $\tau_d = 2$ , $\tau_a = 0.1$ and Bo = 14.5. (d) The velocity of the interface near the tube wall in the tube reference frame $V_{cl}$ follows the tube velocity in the laboratory reference frame (dashed line) for small $\tau_d$ and Oh, corresponding to the inviscid limit for the motion of contact line. $V_{cl}$ is slightly lower than the tube velocity for larger $\tau_d$ and Oh due to the effect of fluid viscosity. Here, We = 2000, $\tau_a = 0.1$ and Bo = 14.5. . . . .	32

2.6	(a) The interface velocity at the tube center and (b) the total kinetic energy of the liquid for different acceleration time $\tau_a$ at $\tau_d = 2$ . In our experiments, the time of the acceleration induced by the rod impact is much smaller than the deceleration time, which corresponds to the limit of very small acceleration time $\tau_a < 0.2$ . (c) The interface velocity at the tube center $V$ and (d) the total kinetic energy of the liquid for different deceleration time $\tau_d$ at $\tau_a = 0.1$ . Here, $Oh = 0.014$ , $We = 1000$ , and $Bo = 14.5$ . . . . .	34
2.7	Jet velocity without gravity effects ( $Bo=0$ , $\tau_a = 0.1$ ). (a) The interface velocity at the tube center for different $Oh$ and $\tau_d$ . When the jet forms ( $\tau \approx 2.6$ for $\tau_d = 2$ , and $\tau \approx 3.2$ for $\tau_d = 4$ ), the interface velocity reaches a maximum value, which is defined as the jet velocity $V_j$ . (b) The jet velocity $V_j$ versus $Oh$ for different $We$ and $\tau_d$ . (c) The jet velocity for small $Re$ collapses on a single curve when $V_j\tau_d^{2/3}$ is plotted versus $Oh^{-1}We^{1/2}$ . (d) For large $Oh$ , $[1 - (V_j/V_{j,0})^2]$ scales with $[Ohf_0(We)]^{2/3}$ , where $f_0(We)$ evaluates the effect of $We$ to the viscous dissipation at $Bo = 0$ . (b-d) shares the same legend in (d). The red dashed lines show the 10% error away from the scaling (black dashed line). . . . .	37
2.8	The time evolution of (a) the velocity at the center of the interface and (b) the liquid kinetic energy when the initial interface is modified by gravity, whose magnitude is indicated by $Bo$ . The solid line includes the gravitational force, while for the dashed line, the gravitational force is excluded. Here, $Oh = 0.014$ , $We = 1000$ and $\tau_d = 2$ and $\tau_a = 0.1$ . . . . .	39
2.9	(a) The inviscid jet velocity $V_{j,0}$ and (b) the dimensionless time when the maximum interface velocity occurs for different $We$ , $Bo$ and $\tau_d$ . (c) The time evolution of the interface for $Bo = 16$ (left) and $Bo = 100$ (right). A slight surface wave occurs at $\tau = 2$ for $Bo = 16$ and this surface wave is more obvious for $Bo = 100$ . Here, $We = 2000$ , $Oh = 0.014$ , $\tau_d = 2$ , $\tau_a = 0.1$ . (d) The jet velocity $V_j$ as a function of $Oh$ for different $Bo$ , $We$ . (e) The jet velocity data are collapsed on a single curve in the plot of $[1 - V_j^2/V_{j,0}^2]$ versus $Ohf(We, Bo)$ , where $f(We, Bo) = (Bo^{1.48} + 7.17)We^{-0.406} + 0.20$ is an empirical function that evaluates the focusing effect of the flow and is obtained by using a least square fit. Red dashed lines indicate 10% error from the scaling. Here, $\tau_d = 2$ , $\tau_a = 0.1$ . . . . .	41
2.10	Study of breakup criteria at $Bo = 14.5$ and $\tau_a = 0.1$ . (a) Phase diagram of jet breakup at $\tau_d = 2$ . Insets are two snapshots of the jet shape before breakup for $Oh = 0.014$ , $We = 400$ (left) and $Oh = 0.14$ , $We = 1800$ (right). (b) Phase diagram at $Oh = 0.014$ . Insets show the jet shape before breakup for $\tau_d = 1$ , $We = 350$ (left) and $\tau_d = 4$ , $We = 1200$ (right). (c) The jet velocity shows a non-monotonic dependence on $\tau_d$ at $We = 1000$ . . . . .	44

2.11	The neck radius at the breakup point $r_b$ plotted versus the time before breakup $\tau_b - \tau$ , where $\tau_b$ is the time when the jet breaks. At Oh=0.014, $r_b$ scales with $(\tau_b - \tau)^{2/3}$ , corresponding to the scaling for inviscid pinch-off where liquid inertia (I) is balanced by surface tension (ST) [46], [47]. At Oh=0.05, $r_b$ scales with $(\tau_b - \tau)$ , corresponding to the scaling for viscous pinch-off where inertia (I), surface tension (ST) and viscous (V) effects balance each other [48]. At Oh=0.14, $r_b$ scales with $(\tau_b - \tau)^{1/2}$ where gravity (G) is balanced by viscous (V) effects [49]. The panels on the right shows the interface profile before pinch-off. Here, Bo = 14.5, We = 2000, $\tau_d = 2$ , and $\tau_a = 0.1$ . . . . .	46
3.1	(a) Schematic of a spring-driven autoinjector and (b) the motion of each component during administration. (c) Experimental images of the liquid slosh during the insertion process. Here, the liquid in the syringe is water. t=0 is set to the beginning of insertion process when the driving rod hits the plunger. . . . .	51
3.2	(a) The geometry of the needle entrance of the syringe. Dimensions are given in millimeter. The length of the syringe $L_1$ can range from 20mm to 40mm, corresponding to the syringe volume from 1mL to 2mL. (b) The bottom (left) and top (right) view of the mesh in the simulations. (c) The displacement, velocity and acceleration of the syringe measured from experiments for two different spring strengths. The acceleration used as an input to the simulations is a simplified form of the experimentally measured kinematics caused by a 30 N spring with spring stiffness of 409 N/m. . . . .	56
3.3	Schematics of (a) the initial interface setup and (b) the slosh dynamics in the syringe frame of reference for a non-zero tilt angle. . . . .	57
3.4	(a) The interface evolution due to Rayleigh-Taylor instability at time 0, 1, 1.25, 1.5, 1.75, 2, and 2.25 s. The present results (left panel, yellow and cyan) is compared with those computed using a diffusive interface method [65] (right panel, red and blue). Only half of the simulation domain is showed. (b) The center of the interface goes down while the interface near the boundary goes up. The transient behavior of the tip position agrees with the published numerical results by Ding et al.[65], Guermond and Quartapelle [66] and Tryggvason [67]. . . . .	58
3.5	(a) The cross section of the liquid-air interface, (b) the total interfacial area and (c) volume fraction of liquids with strain rate $ \mathbf{D}  > 10^4$ for three different mesh resolutions $\delta x = 1/8, 1/0, 1/12$ mm. . . . .	59
3.6	The kinematics (a)displacement, (b)velocity and (c)acceleration of the syringe measured in experiments for different fluid viscosities (a) 4.565 cp, (b) 19 cp and (c) 48 cp. . . . .	61
3.7	The ensemble-averaged interface area calculated using the edge detection method for 4.565 cp. Error bar indicates the standard deviation. Snapshot for one run is shown in the bottom panel. (b) Air gap height in the experiments. (c) The interfacial area in the simulation shows a good agreement with experimental results. . . . .	62

3.8	The interface shape in simulations (labeled by “sim”) and experiments (labeled by “exp”) for different liquid viscosities. . . . .	63
3.9	(a) The cross section of the air-liquid interface, (b) the total interfacial area and (c) volume fraction of liquids with strain rate $ \mathbf{D}  > D_0$ for different liquid viscosities $\mu_l$ . . . . .	64
3.10	(a) The cross section of the interface, (b) the total interfacial area and (c) volume fraction of liquids with strain rate $ \mathbf{D}  > D_0$ for three different air gap heights $h_a = 2,4,6$ mm. . . . .	65
3.11	(a) The cross section of the interface, (b) the total interfacial area and (c) volume fraction for liquids with strain rate $ \mathbf{D}  > D_0$ for three different maximum syringe velocities $U_s = 2.7,5.4,8.1$ m/s. . . . .	66
3.12	(a) The cross section of the interface, (b) the total interfacial area and (c) volume fraction for liquids with strain rate $ \mathbf{D}  > D_0$ for three different tilt angles $\theta_t = 0^\circ, 30^\circ, 60^\circ$ . Here, the air gap height is 4 mm, while the other parameters are the same as Table 3.1 . . . . .	67
3.13	The cross section of the interface, (b) the total interfacial area and (c) volume fraction for liquids with strain rate $ \mathbf{D}  > D_0$ for three different contact angles between the air-liquid interface and the syringe wall $\theta_c = 80^\circ, 100^\circ, 130^\circ$ . . . . .	68
3.14	(a) The cross section of the interface, (b) the total interfacial area and (c) volume fraction for liquids with strain rate $ \mathbf{D}  > D_0$ for surface tensions $\sigma = 40, 50, 60$ dyn/cm. . . . .	69
3.15	(a) The cross section of the interface, (b) the total interfacial area and (c) volume fraction for liquids with strain rate $ \mathbf{D}  > D_0$ for three fill volumes $V_f = 1,1.5,2$ mL. . . . .	70
3.16	The spatial distribution of strain rate (left), vorticity (middle) and flow type (right) on the cross section at $t = 6$ ms for (a) baseline, (b) high viscosity $\mu_f = 20$ cp, (c) large volume gap $h_a = 6$ mm, (d) large tilt angle $\theta_t = 60^\circ$ and (e) large contact angle $\theta_c = 130^\circ$ . The air-liquid interface is indicated by the white line. . . . .	71
3.17	Fig. 15. Continuation of Fig. 14. . . . .	72
3.18	(a) $(Q_w, -Q_s)$ and (b) $(R_s, Q_s)$ map with the physical meanings for each zone. Pure extensional flow with large $Q_s$ , zero $Q_w$ , and negative $R_s$ is considered most possible to unfold protein molecules. . . . .	74
3.19	Joint PDFs on maps of $(Q_w, -Q_s)$ and $(R_s, Q_s)$ at $t = 4$ ms for (a) baseline simulation, (b) higher viscosity $\mu = 5$ cp, and (c) large tilt angle $\theta_t = 60^\circ$ . The contour levels from blue to yellow are $2 \times 10^{-5}, 6 \times 10^{-5}, 1.4 \times 10^{-4}, 2 \times 10^{-4}, 4 \times 10^{-4}, 6 \times 10^{-4}, 10^{-3}$ . $\langle Q_w \rangle$ is the average $Q_w$ for all the fluids, and is $3.43 \times 10^5, 2.73 \times 10^5, 7.72 \times 10^5$ s $^{-2}$ for plot (a) (b) and (c), respectively. . . . .	75

3.20	The trajectories of conditional mean on maps of (a) $(Q_w, -Q_s)$ and (b) $(R_s, Q_s)$ for tilt angle $\theta_t = 60^\circ$ . The cross-sectional strain rate field for states 1~4 are shown in (c). . . . .	77
3.21	The summary of dependence of (a) the maximum interfacial area and (b) the volume fraction of liquids with $ \mathbf{D}  > D_0$ on the liquid viscosity $\mu u_l$ , the air gap height $h_a$ , the maximum syringe velocity $U_s$ , the tilt angle $\theta_t$ , contact angle $\theta_c$ , surface tension $\sigma$ , and the fill volume $V_f$ . . . . .	79
3.22	The summary of dependence of (a) max interfacial area and (b) the volume fraction of liquid with $ \mathbf{D}  > D_0$ on dimensionless numbers. In (a), the interfacial area is scaled by the square of syringe inner radius. . . . .	80
4.1	(a) The administration process is comprised of 3 stages: the activation, the insertion and the injection. The figure is reproduced with permission from [6]. (b) Schematic showing the structure of an autoinjector and the name of each components. (c) Cavitation at the start of the insertion process recorded by a high-speed camera for two different autoinjectors. The lifetime of cavitation bubbles is on the order of 0.1 ms. . . . .	85
4.2	A schematic of pressure wave propagation in the syringe after the driving rod strikes the plunger. . . . .	88
4.3	(a) Schematic of cavitation generation in the syringe. When the bottom syringe wall (near the needle) gains speed, the pressure variation due to pressure waves leads to the bubble growth and collapse. The geometry setup in axisymmetric and 3D simulations are shown in (b) and (c), respectively. . . . .	89
4.4	Experimental setup for simultaneous measurement of displacement and acceleration of syringe using a high-speed camera and accelerometer, respectively. (a) Snapshot of ex-situ autoinjector setup with an accelerometer mounted at the bottom of the syringe. (b) and (c) show the example data of displacement (from the camera) and acceleration (from the accelerometer) of the syringe, respectively. . . . .	91
4.5	(a) Displacement of the plunger and the syringe bottom recorded by the camera in ex-situ experiments. When the driving rod impacts the plunger, the plunger is pushed and the air on top of the solution is compressed. Later, the plunger and syringe move together with the same speed. (b) The syringe displacement, velocity and acceleration upon impact. . . . .	97
4.6	Experimental images of a cavitation bubble compared with the simulation results (green line). Passive tracers (green dots) are added in the simulations to illustrate the protein migration on the bubble surface. . . . .	99

4.7	(a) The dimensionless syringe velocity $v_s$ normalized by the dimensionless atmosphere pressure $p_r$ . $v_s/p_r = 1$ corresponds to the velocity change to induce a pressure drop of one atmosphere pressure. (b) The pressure variation in the liquid column with height $L = 34\text{mm}$ due to the propagation of the pressure wave. (c) The pressure change at the syringe bottom, $x = 0$ . The maximum acceleration occurs at $t = 4.6$ , inducing the strongest pressure drop (red dashed line). The oscillation of pressure wave causes the pressure inside the syringe to oscillate with a period of $4L/c$ . Pressure wave induced by the first acceleration peak can be reflected by the syringe bottom inducing subsequent pressure drops (green dashed line). . . . .	100
4.8	Pressure variation experienced by the nucleus, radius and the maximum radius for different (a) nucleus location $x_b$ , (b) liquid column height $L$ , (c) air gap pressure $P_g$ and (d) nucleus size $R_0$ . The second row shares the legend with the first row. Default parameters are $x_b = 0.2$ , $L = 34$ mm, $P_g = 1.4$ bar, $R_0 = 0.1$ mm. The pressure is greatly underestimated here, because 1D calculation assumes the bubble to be spherical. Scaling of the dimensionless variables are listed in Table 4.2. $r$ and $r_{max}$ are dimensionless radii normalized by $R_0$ . . . . .	102
4.9	Mesh dependence of the axisymmetric simulations. (a) The interface shape and tracer locations for different grid sizes and (b) the corresponding bubble radius, (c) jet velocity and (d) maximum liquid pressure. . . . .	104
4.10	Time evolution of the bubble surface and tracers (indicated by dots) for (a) baseline simulation, (b) larger distance of the nucleus from the wall, $x_b = 0.05$ , (c) larger liquid column height $L = 44$ mm, (d) larger air gap pressure $P_g = 2$ bar and (e) larger nucleus size $R = 0.2$ mm. The bottom syringe wall is indicated by the horizontal dashed line, which is $x = -0.648$ in (a) and (c-d), and $x = -1.8$ in (b). Length is in unit of millimeter. Default parameters are $x_b = 0.018$ , $L = 34\text{mm}$ , $R = 0.05\text{mm}$ . . . . .	105
4.11	The pressure, flow and strain rate fields at the instant when the pressure peaks are generated: (a) The jet impacts the bubble surface for a large distance to the wall $x_b = 0.05$ at $428.4 \mu\text{s}$ , (b) The jet impacts the bottom syringe wall in the baseline simulation at $432 \mu\text{s}$ and (c) the toroidal bubble collapses into the minimum size in the baseline simulation at $450 \mu\text{s}$ . Streamlines are indicated by black curves. . . . .	107
4.12	Time evolution of equivalent bubble radius, re-entrant jet velocity, maximum liquid pressure for different values of (a) distance to the bottom syringe wall, (b) liquid column height, (c) air gap pressure and (d) nucleus size. The first and third columns share the same legend as the second column. . . . .	108
4.13	The dependence of bubble radius $R_{max}$ , jet velocity $v_j$ , and liquid pressure $P_{max}$ on the nucleus location $x_b$ , liquid column height $L$ , air gap pressure $P_g$ and nucleus size $R_0$ . Other parameters are the same as the baseline simulation ( $x_b = 0.018$ , $L = 36$ mm, $P_g = 1.4$ bar, $R_0 = 0.05$ mm). . . . .	110

4.14	The interface shape and passive tracers (black dots) for a bubble collapse in a 3D simulation. The face color of the interface indicates the magnitude of the flow velocity. Length is in the unit of millimeter. Here, $x_b = 0.018$ , $L = 34\text{mm}$ , $P_g = 1.4\text{bar}$ , and $R_0 = 0.2\text{mm}$ . . . . .	112
4.15	The interface shape and passive tracers (black dots) for a bubble cloud consisting of 4 nuclei of size $R_0 = 0.2$ mm. The face color of the interface indicates the magnitude of the flow velocity. Length is in unit of millimeter. . . . .	113
4.16	The maximum liquid pressure for a single nucleus and a bubble cloud of 4 nuclei.	114
4.17	Schematic demonstrating the proposed protein aggregation process during the collapse of a cavitation bubble near the syringe wall. . . . .	115

## ABSTRACT

Today, autoinjectors are developed for more viscous drug solutions, which require larger forces for actuating the syringe and impose larger stresses on the drug solution during the administration of autoinjectors. We developed experimentally validated high-fidelity simulations to investigate the liquid jet formation, liquid slosh and cavitation during the insertion process of an autoinjector.

The jet formed due to an acceleration-deceleration motion of syringe is found to be governed by the interplay between inertial, viscous, surface tension and gravitational forces. A scaling for the jet velocity and a criterion for the jet breakup in a simplified geometry are proposed.

When the syringe accelerates and decelerates during the insertion, liquid slosh occurs and there is a vehement motion of the air-liquid interface. Here, we quantified the area of air-liquid interface and hydrodynamic strain rate, which increase with the air gap size, syringe velocity, tilt angle and inner wall hydrophobicity, and decrease with the solution viscosity and hardly change with the liquid column height and surface tension. The strain rate is not sufficient to unfold the protein and the air-liquid interface is more likely to cause protein aggregation.

In a spring-driven autoinjector, the plunger is actuated by the impact of a driving rod, which generates a strong pressure wave and can cause cavitation inception. The cavitation bubbles can be impeded by the syringe walls and form a re-entrant jet shooting toward the syringe wall. During the process, the protein molecules are focused in the jet, pushed toward the syringe wall and spread across the wall, which can be the reason for the protein aggregation and adsorption on the syringe walls. The impedance effects of the wall decreases with the wall distance and increases with the maximum bubble size. The maximum bubble radius also increases with the liquid column size and nucleus size and decreases with the air gap pressure. Since inertia effects dominate in the cavitation process, the liquid viscosity and surface tension hardly changes the cavitation bubble dynamics. Small bubbles can also form in the bulk, which may generate aggregates in the bulk solution. Bubbles in the cavitation bubble cloud may coalesce with nearby bubbles and induce a higher pressure at the collapse

(up to 1000 bar). This high pressure can potentially generate hydroxyl radicals that oxidize the protein molecules.

The current study presents a detailed picture of fluid flows in autoinjectors and provide recommendations for mitigating the liquid slosh and cavitation generated in syringes. The results can be combined with future experiments to understand the implications of fluid flows on protein drugs and the performance of autoinjectors.

# 1. INTRODUCTION

Autoinjectors and pens are devices designed for the self-administration of a fixed small dose, typically less than 2mL, of pharmaceuticals for patients. Today, most of the autoinjectors are designed for subcutaneous injection with very simple administration procedures that prevent needle stick injury and alleviate needle phobia among patients. The administration of autoinjectors does not require the patient to visit hospitals and reduces their dependencies on healthcare professionals. Auto-injectors have become the gold-standard in the treatment of various indications including diabetes, anaphylaxis, sclerosis, rheumatoid arthritis and others due to their simplicity, convenience and low prices [1] (fig. 1.1).

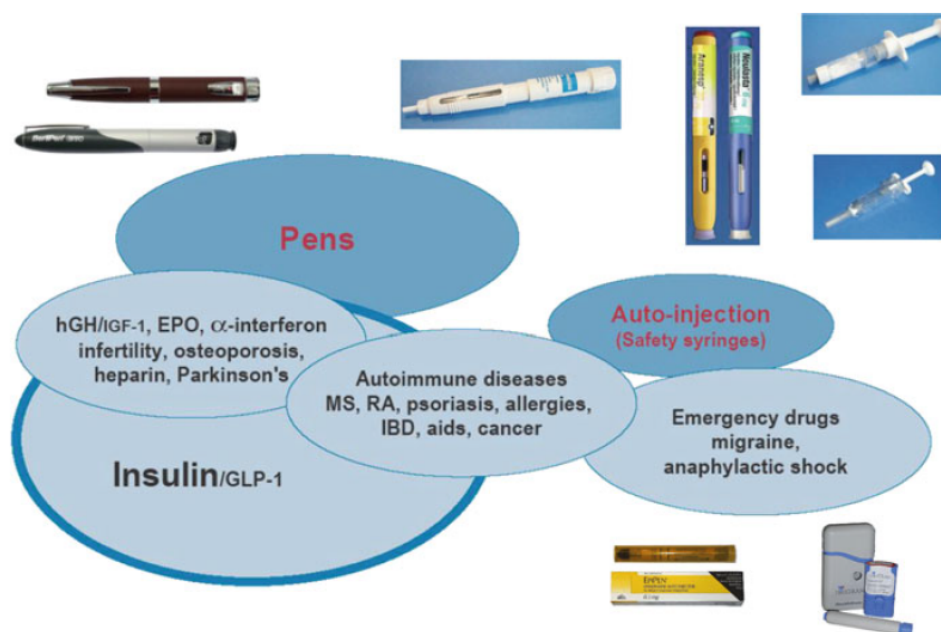


**Figure 1.1.** Self-injection therapies and devices reproduced with the permission from ref. [2]

## 1.1 Motivation: trends of autoinjectors

The global market of autoinjectors and their sales have seen a dramatic growth in recent years [2], [3]. A market research in 2017 has indicated that the Compound Annual Growth Rate (CAGR) of the autoinjector industry is anticipated to be 15.1% between 2016 and

2026 and the projected value of autoinjector market is over \$7billion by the end of 2026 [4]. One reason for the fast-growing demand of autoinjectors is the trend toward the parenteral drugs that cannot be administered orally, such as the insulin for diabetes and epinephrine for anaphylaxis [5]. On the other hand, as more generic versions of autoinjectors are approved, the prices of autoinjectors have decreased in the recent years, making them more accessible to the patients [4].

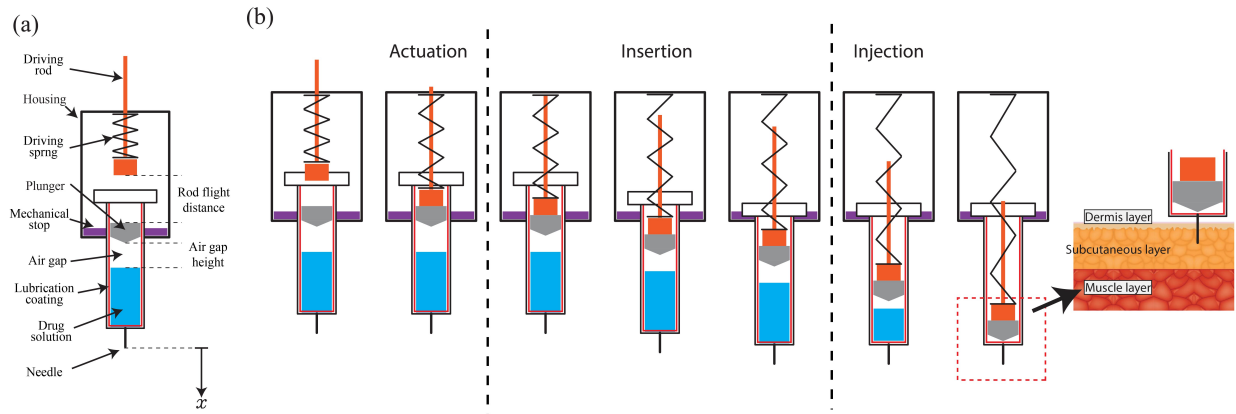


**Figure 1.2.** (a) Structure of a spring-driven autoinjector. (b) The motion of each component during the subcutaneous administration. The figures are produced with the permission from ref. [6]

Today, most autoinjectors in the market are disposable with a prefilled syringe actuated by a preloaded spring [7]. A common structure for the spring-driven autoinjectors is illustrated in Fig. 1.2(a). The subcutaneous administration of the autoinjector typically consists of three parts (Fig. 1.2(b)): Upon trigger, the preloaded spring is released and propels the driving rod until the rod hits the plunger (activation process). Then the syringe together with the plunger is accelerated to a high velocity and then decelerated by the mechanical stop. Here, the needle goes outside the device and penetrates the human skin (insertion process). Later, the plunger is slowly pushed by the spring, emptying the drug products into the target place of the subcutaneous tissue (injection process). In some autoinjectors, pressurized gas may be used for the propulsion of the syringe [8]. In some designs, the needle can be detached from the glass body, which is called cartridge [8]. In the cartridge system,

needle is pushed toward the needle with its seal penetrated by the needle. Then the cartridge together with the needle are inserted into the patients' tissue.

The drug dose in subcutaneous injection is usually constrained by the absorption ability of tissues. Therefore, most syringes carry a liquid volume less than 2 mL. A larger volume is more likely to cause discomfort and pain [7], [9]. Furthermore, the increase of the injection volume usually requires a longer injection time and a needle of larger diameter, which can induce more pains for the patient. Due to the constraint of the injection volume, biologics with low potency, notably monoclonal antibodies, need to be administered in high concentrations. As the drug concentration increases, the solution viscosity increases more than linearly [10], [11], and larger forces are needed for actuating the syringes. This can lead to more vehement motion of the syringes and drug solutions during the insertion process. On the other hand, when the highly viscous solution is pushed into the needle, higher pressure can be built up inside the syringe. The reliability of the device and the stability of the drugs during the administration process are a great concern in the development of new autoinjectors, which is also of vital importance to the patients' health and safety.

## 1.2 Concern of protein aggregation in autoinjectors

As a product to deliver parenteral drugs, the autoinjectors are subject to strict requirements set forth by the United States Pharmacopeia (USP) [12], which entails that the drug solutions should be protected against the contamination of particulate particles, including protein aggregates, fibers, glass shards, metals, etc. Violent motions of the drug solution such as shaking, stirring [13] and dropping [14] are notoriously known as the sources of protein aggregation in the manufacture, formulation, filling, storage and delivery of therapeutic proteins [5]. These protein aggregates are responsible for eliciting adverse immunogenic responses in patients [15]–[18], leading to potential health and safety issues of the autoinjector products.

Denaturation or damage of proteins are attributed to various reasons. In early days, it was reported that the enzymes exhibit an activity loss after experiencing a shear flow in a cylindrical viscometer [19]. Later on, it turns out that the hydrophobic interfaces, including

the air-liquid [5], [20], solid-liquid [21] and oil-liquid [22], [23] interfaces, accompanied with the shearing flow are usually the predominant reason for protein denaturation, while the hydrodynamic shear required for unfolding the protein molecules is relatively high [24] so that pure shear flow rarely contribute to the damage or losses [5]. On the other hand, some other reasons are also proposed for protein denaturation, including flow extensional stress [25], local concentration difference [26], radical generation due to cavitation bubbles and motion of contact lines [27]. Therefore, it is of vital importance to understand the fluid flows inside syringes to find the role of flow on the damage and aggregation of the drug molecules.

The violent flows during the administration process and the associate damage to proteins are important considerations in the development of autoinjectors. Even though the mechanism of protein denaturation and aggregation formation has been extensively studied by pharmaceutical, chemical and biotechnological researchers, there are only a limited number of studies that investigate and characterize the fluid flows inside the syringe. This dissertation works on the high-fidelity numerical modeling of the fluid flows during the administration of autoinjectors. To recognize the potential reason for protein aggregation, we evaluate the hydrodynamic stress in the solution and also analyze the motion of air-liquid interface and the strain rates. Our results shed light on the effects of different design parameters, such as the syringe kinematics, fill volume, air gap size, drug viscosity and syringe lubrication, which provide insights for researchers and engineers in pharmaceutical industry to improve the design of autoinjectors.

We identify two fluid dynamics phenomena that are most relevant to the protein aggregation formation and autoinjector reliability: (a) the liquid slosh caused by the acceleration and deceleration during the insertion process, and (b) the cavitation bubble formation induced by the rod impact at the start of the insertion process. The first process occurs in 20~40 ms, while the time scale for the second process is on the order of 0.1 ms. Due to the large difference of the time scale, the two problems are investigated and discussed separately in the next two sections.

### 1.3 Jet formation and liquid slosh induced during the insertion process

During the insertion process, the syringe together with the drug solution is accelerated by the driving rod and then decelerated by the mechanical stop (Fig. 1.2). A liquid jet can form in the center of the air-liquid interface, which strikes the plunger and breaks. The formation of the liquid jet and its velocity dependence on syringe kinematics and fluid properties are important to understand the liquid motion inside the auto-injector. Chapter 2 focuses on the liquid jet formation process for a initially concave meniscus interface undergoing a constant acceleration-deceleration motion. To lay a foundation for the fluid mechanics of the jet formation process, we investigate the scaling of the jet velocity and the breakup criteria of the liquid jet.

In chapter 3, we investigate the liquid slosh and the motion of air-liquid interface during the insertion process of the syringe. We validated our simulation results by comparing the interface shape with those observed in the experiments. To evaluate the risk of denaturation for proteins, we measured the interfacial area and strain rate in the drug solution for different air gap size, syringe velocity, liquid viscosity and so on. The distribution of the strain rate are also analyzed, which helps to find the most possible regions for protein aggregation.

### 1.4 Cavitation at the start of the insertion process

At the start of the insertion process (Fig. 1.2), the driving rod strikes the plunger, leading to an abrupt acceleration of the syringe. This sudden acceleration generates pressure waves propagating in the liquid column and cavitation occurs whenever the pressure drops below a certain point. The collapse of the cavitation bubble can release a high speed re-entrant jet, potentially leading to the aggregation of protein molecules and the pitting or even breakage of syringe wall [3], [28]. The gas contents in the cavitation bubble is compressed in a short time, where the high temperature and pressure can potentially induce the hydroxyl radicals that oxidizes the protein molecules. In Chapter 4, we investigate the cavitation bubble dynamics in an autoinjectors using one-dimensional analysis as well as high-fidelity numerical simulations. Passive tracers are used to illustrate the migration of protein molecules during the cavitation

process. The effects of flow strain rate and interfacial effects, including air-liquid and oil-liquid interface, are also discussed in this chapter.

## 2. VELOCITY SCALING AND BREAKUP CRITERIA FOR JETS FORMED DUE TO ACCELERATION AND DECELERATION PROCESS

*This chapter is reproduced with permission from:*

*Zhang, Y., Guo, T., Vlachos, P. and Ardekani, A.M., 2020. Velocity scaling and breakup criteria for jets formed due to acceleration and deceleration process. Physical Review Fluids, 5(7), p.074003. The experiments are conducted by Tianqi Guo.*

### 2.1 summary

We investigate the formation of a liquid jet due to an impact. The fluid contained in a completely wettable tube undergoes a constant acceleration-deceleration motion with the acceleration time being much smaller than the deceleration time duration. During the impact, the fluid near the wall rises up. For a small deceleration time and liquid viscosity, the velocity of the contact line between the liquid and the wall approximates the tube velocity. Later, the tube deceleration causes the flow to focus at the center of the tube forming a liquid jet. The velocity of liquid jet is mainly characterized by five dimensionless numbers: the Weber number (We), the Ohnesorge number (Oh), Bond number (Bo) and dimensionless acceleration ( $\tau_a$ ) and deceleration time ( $\tau_d$ ). We investigate the cases with very small acceleration time. The jet velocity and the liquid kinetic energy increase with acceleration time and reach a maximum value for a certain deceleration time. For zero Bond numbers, our numerical simulations show that the jet velocity  $V_j$  scales with  $\text{Oh}^{-1/4}\text{We}^{1/8}\tau_d^{-2/3}$  for large Oh. For a wide range of Bond numbers, the kinetic energy reduction due to viscous dissipation in jet tip  $[1 - V_j^2/V_{j,0}^2]$  scales with  $\text{Oh}^{2/3}f(\text{We}, \text{Bo})^{2/3}$  for small Oh, where  $V_{j,0}$  is the inviscid jet velocity,  $f(\text{We}, \text{Bo})$  is an empirical function of We and Bo obtained from least square fit of numerical results. At small Bo, the jet forms due to the focusing flow and the jet velocity decreases with surface tension. On the other hand, at large Bo that the initial interface is flatter, the collapse of surface wave enhances the jet formation and jet velocity increases with surface tension. For the Bond number in experiments, we also investigate the

breakup criteria for the liquid jets. By denoting the critical Weber number for breakup as  $We_c$ , we find that  $f(We_c, Bo)^{-2/3}$  linearly increases with  $Oh^{2/3}$  for a wide range of  $Oh$ , and has a non-monotonic dependence on  $\tau_d$ .

## 2.2 Introduction

A liquid jet forms when the liquid-gas interface is subject to an impact [29]. One of the most fundamental jet formation problem is the one generated by a bursting bubble [30], [31], where a bubble laying right beneath a liquid-gas interface bursts and a liquid jet forms as the consequence of the collapse of the gas cavity. The problem is only dependent on two nondimensional numbers, the Bond number ( $Bo$ ) and the Ohnesorge number ( $Oh$ ). Recently, Ganan-Calvo [32] investigated the published experimental data and proposed a scaling for both the velocity and radius of the first ejected droplet after the bubble bursting in the limit of zero Bond number. The scaling is then extended to a wide range of Bond numbers [33], [34] and applied to find a self-similar shape of cavity and jet profiles [35]. More discussions on the bursting bubble problem can be seen in the works of Gordillo and Rodríguez-Rodríguez [36], [37] and Ganan-Calvo and López-Herrera [38].

Aside from the collapse of a bursting bubble, a sudden movement of the container can also generate liquid jets and droplets. This problem is of vital interest in the injection of pharmaceuticals, propellant sloshing in spacecrafts, and the transportation of unstable liquids. In the drug industry, therapeutic proteins can be damaged or denatured by the hydrodynamic shear involved in the motion of liquid-air interface [5], [13]. Therefore, an understanding of jet and droplet formation during the motion of drug container is helpful for minimizing the loss of protein activity. Propellant slosh can occur during launch of spacecrafts, where the violent motion of liquid can introduce uncertainties in spacecraft attitude [39]. When flammable and combustible liquids are transported, the liquid slosh can generate substantial amount of heat. The flammable temperature is reduced and more cautions are required for shipping these liquid.

One of the most fundamental example of the jet induced by a sudden motion is Pokrovski's experiment. In the experiment, the tube containing the liquid falls freely due the gravity

and then impacts a rigid wall. The sudden change of the tube velocity induces a pressure impulse, in turn generating liquid velocity inside the tube. The analytical solution for the velocity and pressure field at the start of the impact has been found by Antkowiak et al. [40]. Kiyama et al. [41] extended the study into a wider range of accelerations and liquid column heights. They categorized the liquid jet into three types: normal type, splash type and cavitation type. For splash type jets, liquid curtains are formed from the liquid-gas interface due to the presence of the pressure wave. While for cavitation type, there are cavitation bubbles forming due to the pressure drop in the bulk. Onuki et al. [42] proposed a new experimental setup. In their experiments, a thin tube is added to be partially submerged in the liquid so that highly viscous microjets can be generated. In short time, during the impact interval, the jet velocity agrees well with the physical model based on the pressure impulse theory, suggesting that the viscous effects are negligible during the impact. After the impact, during the flow focusing process, fluid viscosity decreases the jet velocity, which can be described by the Reynolds number.

In this paper, we investigated the jet induced by a sudden motion using a different experimental setup, where the tube is hit by a spring-driven rod and then gradually decelerates due to friction and stops. The motion of the tube can be approximated with a constant acceleration motion followed by a constant deceleration motion. Our problem resembles the Pokrovski's experiment, since in both cases, in the reference frame of the tube, the liquid jet is generated due to the downward body force induced by deceleration. While, in our case, the liquid also gains an initial velocity due to the acceleration process. The magnitude of acceleration and deceleration is much smaller than those in Pokrovski's experiment, so that the water hammer and fluid compressibility do not affect the jet formation for a wide range of impact speed studied in this work. Besides, the magnitude of acceleration and deceleration is more controllable and easier to measure. To understand the jet velocity dependence on fluid properties and tube kinematics, we focused on the liquid that is completely wetting to the tube wall, i.e., the contact angle between the liquid-gas interface and wall is zero.

## 2.3 Method

### 2.3.1 Experimental Setup

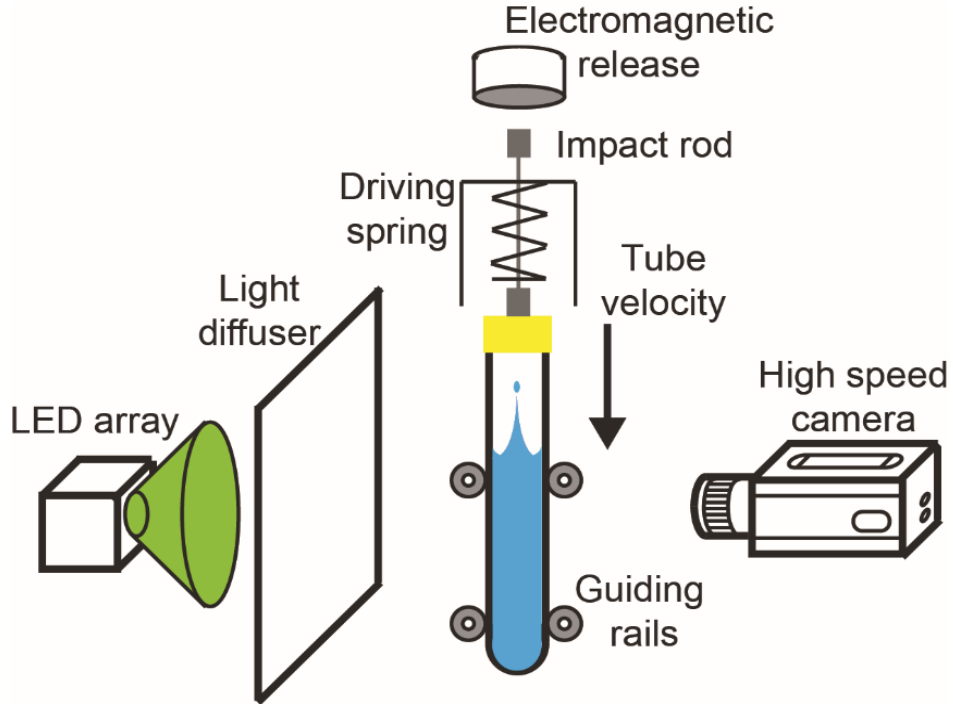


**Figure 2.1.** (a) A schematic of the experimental setup. The working fluid (Sigma-Aldrich 317667 silicone oil, viscosity 5 cSt, surface tension 20 mN/m, density 913 kg/m<sup>3</sup>) is completely wetting with the glass tube.

As illustrated in the schematic drawing shown in Fig. 4.1, a stainless-steel impact rod is released by the electromagnet (5893K96, McMaster Carr) and accelerated by a driving spring until it impacts on the plastic cap on the test tube (borosilicate glass, with inner radius of  $R = 5.7$  mm and length of 100 mm), which contains 2 mL of silicone oil. Subsequent to the impact, the tube is suddenly accelerated and then gradually stopped due to the friction of the guiding rails. The guiding rails are made of two parallel 25 mm  $\times$  25 mm T-slotted profiles (25-2525, 80/20 Inc), which keep the tube slide along the T-slots without blocking the view of the surface jets. Uniform background illumination is achieved by using an LED light source (Flashlight 300, LaVision) with a light diffuser (DG100X100-1500, ThorLabs, Inc.). The motion of the tube and the liquid-gas interface are captured in a shadowgraph

configuration by a high-speed camera (Phantom v2640, Vision Research) with a frame rate of 10,000 per second.

For each frame, the displacement of the glass tube is determined by locating the bottom of the tube after image binarization. For most of our experiments, the tube motion can be approximated by a constant acceleration-deceleration process where tube velocity increases linearly from 0 to a maximum velocity  $U$  at time  $t_a$ , and then decreases linearly to zero after time  $t_d$ . The maximum tube speed  $U$  depends on the spring compression, which varies between test cases. With one guiding rail mounted on a precision linear stage (X-LRQ075AL-E01-KX13C, Zaber Technologies Inc.), deceleration time  $t_d$  is controlled by adjusting the distance between the rails. In most of our experiments, the acceleration time  $t_a$  ( $\sim 0.5$  ms) is much smaller than the deceleration time  $t_d$  ( $\sim 5$  ms).

### 2.3.2 Numerical Method

The flow field inside the tube is governed by Navier-Stokes equations since the impacts are in the incompressible flow regime. From the previous study by Antkowiak et al.[40], the flow field is not affected by the wall at the tube bottom for a long enough liquid column. Therefore, we do not consider the role of the height of liquid column on the jet dynamics. To have a manageable parameter space, we focused on the liquid that is completely wetting to the tube wall, i.e., the contact angle between the liquid-gas interface and wall is small. After scaling lengths by the tube inner radius  $R$ , velocity by  $U$ , and time by  $R/U$ , the jet dynamics in our problem is characterized by five dimensionless numbers: the Weber number  $We = \rho U^2 R / \sigma$ , the Ohnesorge number  $Oh = \mu / \sqrt{\rho \sigma R}$ , the Bond number  $Bo = \rho g R^2 / \sigma$ , the dimensionless acceleration time  $\tau_a = t_a U / R$  and dimensionless deceleration time  $\tau_d = t_d U / R$ , where  $g$  is the gravitational acceleration,  $\rho$ ,  $\sigma$ ,  $\mu$  are the liquid density, surface tension, and viscosity, respectively.

We performed axisymmetric simulations by using a two-phase flow solver Gerris with an adaptively refined mesh near the liquid-gas interface [43]. A body force term is added to include the effects of the acceleration and deceleration of the tube since we move in the tube frame of reference. Initial liquid-gas interface is calculated from a separate simulation

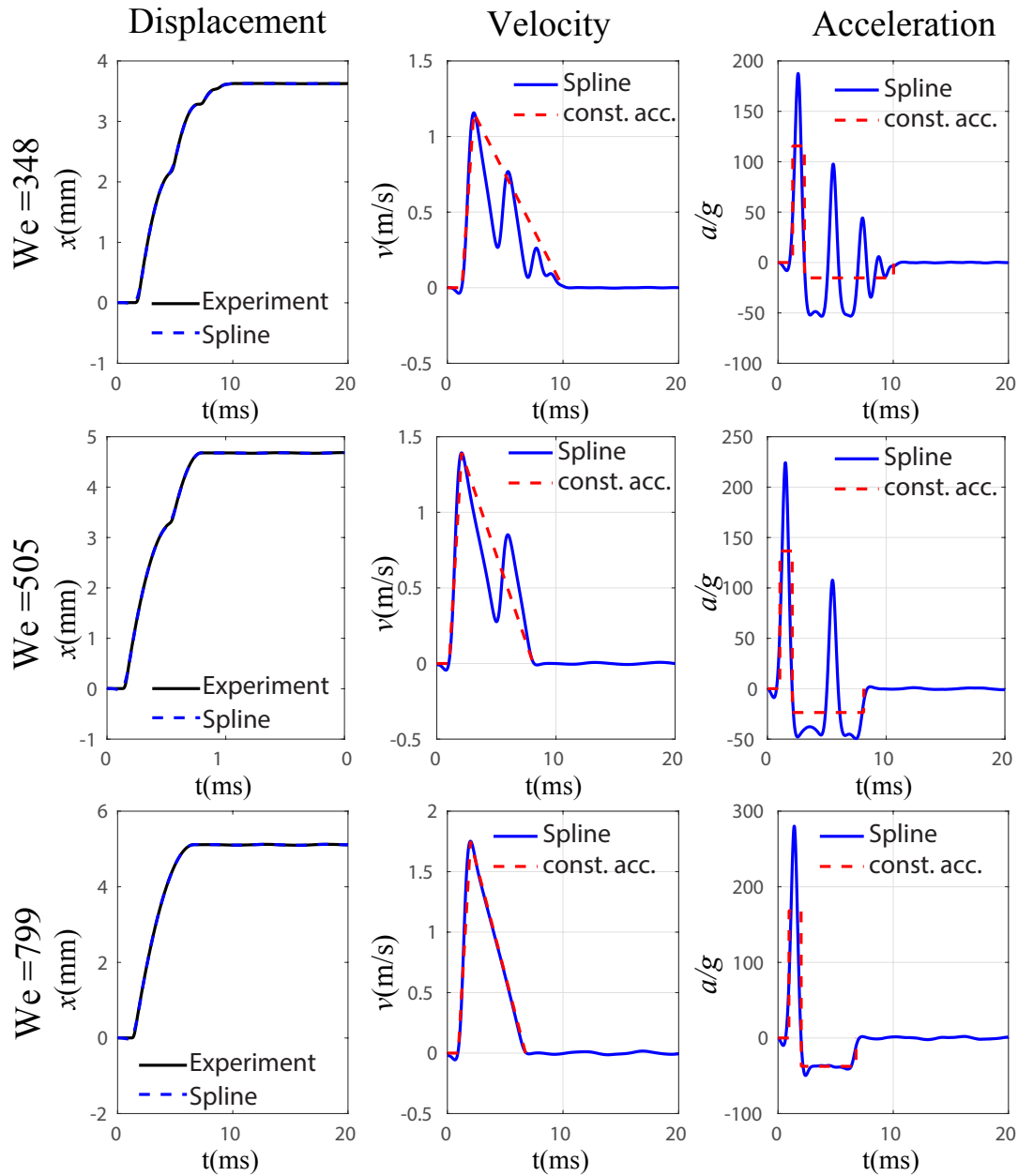


**Figure 2.2.** The displacement (left), velocity (middle) and acceleration (right) of the tube for three different spring compressions with  $We$  corresponding to 348 (top), 505 (middle), and 799 (bottom).

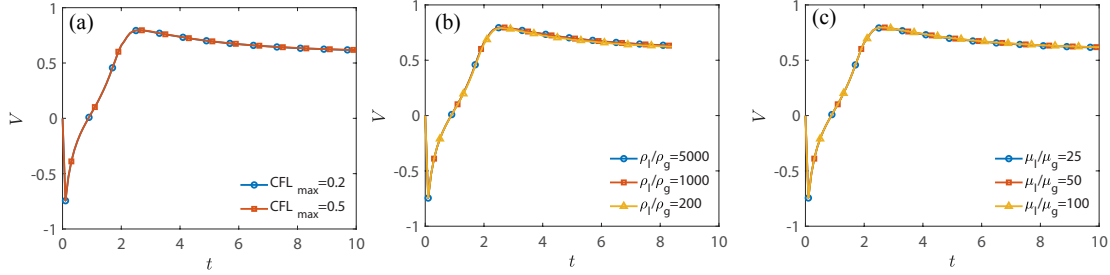


**Figure 2.3.** The interface velocity at the tube center is independent of (a) the max CFL in the simulation, (b) the density ratio between the liquid and gas  $\rho_l/\rho_g$  and (c) the viscosity ratio between the liquid and gas  $\mu_l/\mu_g$ . Here,  $Bo = 0$ ,  $Oh = 0.001$ ,  $We = 1000$ ,  $\tau_d = 2$ ,  $\tau_a = 0.1$ .

where the interface deforms from a flat interface into the hydrostatic equilibrium state in the absence of tube movement. The contact angle is  $1^\circ$  corresponding to the completely wetting fluid used in the experiments and the interface shape in the hydrostatic equilibrium is only determined by the Bond number. For  $Bo = 0$ , the initial interface shape is close to a semi-sphere. The simulation domain is a  $1 \times 15$  box, with  $y \in [0, 5]$  initially occupied by liquid while  $y \in [5, 15]$  occupied by gas. No-slip boundary conditions are applied for the tube walls, and a symmetry boundary condition is applied for the axis. The contact line between the interface and tube wall is described by the constant contact angle model in Gerris [44], which allows for numerical slip in the vicinity of the contact line. During the simulation, the grid points near the liquid-gas interface are refined to a grid size of  $\Delta x = 1/2^{10}$ , and the grid points in regions with high velocity and stress are refined to  $2\Delta x$ . The density and viscosity ratio between liquid and gas are 1000 and 50, respectively. Since the density and viscosity of the liquid are much larger than those of gas, the simulation results are hardly modified by the density and viscosity of gas (Fig. 2.3). The density and viscosity ratio are based on the water-air properties. In experiments, density ratio is around 1000 and viscosity ratio is about 250. The air viscosity in our simulation is 5 time smaller than the experiments, but it does not affect the simulation results. In all the simulations, time step is controlled by setting the maximum CFL as 0.5, and the simulation results are independent of the max CFL (Fig. 2.3). The simulations are performed in parallel with 16 processors, which takes around 10 hours to finish.

## 2.4 Results

### 2.4.1 Experimental validation of numerical simulations

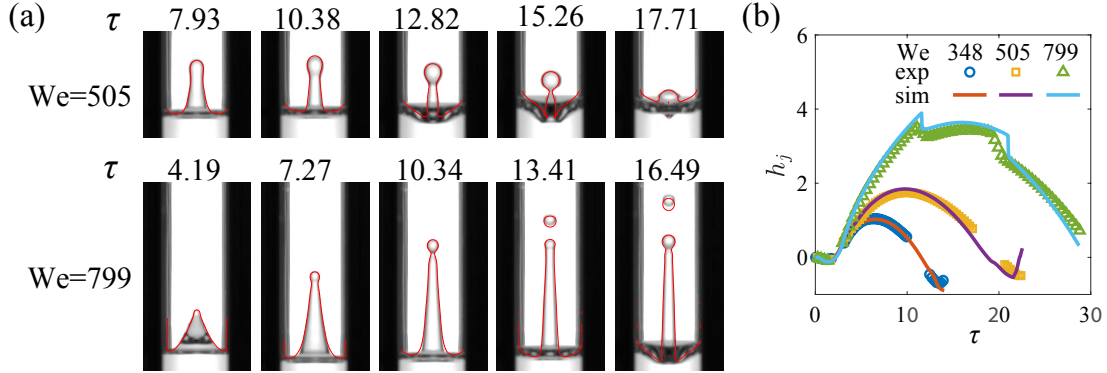


**Figure 2.4.** (a) Comparison of surface profiles between experimental and numerical (red line) results for two Weber numbers. The jet breaks up for  $We = 799$ , but does not for  $We = 505$ . Dimensionless time  $\tau = tU/R$  is denoted at the top of each frame. (b) Time evolution of the jet height  $h_j$  from simulations and experiments.  $h_j$  is defined as the interface height at the center of the tube, and the initial jet height is set to zero. The experimental data for small jet height is missing because the jet is inside a cavity and is not visible in images. For  $We = 348, 505, \text{ and } 799$ ,  $\tau_d$  are 1.57, 1.47 and 1.46, respectively, and  $\tau_a$  are 0.21, 0.25 and 0.33, respectively.  $Bo = 14.5$ . Viscosity ratio between inner and outer fluids in simulations is 50 which is about 5 times smaller than that in experiments. Here,  $Oh = 0.014$ .

We first validated our simulations with the experimental results. To get the acceleration needed for the numerical simulations, we measured the displacement of the bottom of the tube. The displacement data, the calculated velocity and acceleration profiles for three experimental tests are shown in Fig. 2.2. We first fit the displacement data points with a smoothing spline, which represents the tube displacement as a continuous and differentiable function of time. Then, the 1<sup>st</sup> and 2<sup>nd</sup> order derivative of the smoothing spline are calculated as the temporal velocity and acceleration. For the calculation of dimensionless numbers, we approximated the tube motion with a constant acceleration-deceleration process, where the tube velocity increases to the maximum velocity with a constant acceleration and then decreases to zero. For experiments of  $We = 348$  and  $505$ , the rod hits the tube cap multiple

times. For larger spring compression and higher  $We$  ( $We = 799$ ), the deceleration is constant and the tube motion is close to the constant acceleration-deceleration motion. Simulations for validation purposes use a smoothing spline as the input kinematics.

Our simulations show a very good agreement with experimental results when comparing the surface profiles (Fig. 2.4(a)). There is small differences between the simulation and experimental results, which may stem from the errors in measurement of tube acceleration and the discrepancy of the initial interface shape. The numerical results of jet height (Fig. 2.4(b)) also shows a quantitative agreement with experimental measurement throughout the entire life time of the jet. For smaller  $We$  ( $We = 348$  and  $505$ ), the jet does not break, and the jet height is continuous. While for larger  $We$  ( $We = 799$ ), the jet breaks up. The first droplet is ejected from the jet at  $\tau \approx 10$  and the second droplet at  $\tau \approx 20$ , where  $\tau = tU/R$  is the dimensionless time in the simulation. At the instant of jet pinch-off, a new jet forms underneath the ejected droplet and there is a sudden decrease in the jet height. Here, the impact interval, which is  $\tau_a + \tau_d \approx 2$ , is much smaller than the time scale of the liquid jet. The impact results in an initial jet velocity, then the jet velocity gradually decreases mainly due to gravity. When the jet velocity decreases to zero, the jet reaches the maximum height. Later, the jet height decreases to zero, and a cavity can form at the center of the tube. For larger  $We$ , the jet gains more initial momentum due to the impact. The liquid shoots higher and is more likely to break up. In the following sections, we first investigate the interface dynamics during the jet formation process, where the interface center gains an initial velocity and a liquid jet forms, and then the long term behavior of the liquid jet which is characterized by the breakup and droplet ejection.

### 2.4.2 Jet formation process

The interface profiles and the velocity field (Fig. 2.5(a)(b)) demonstrate the jet formation process: since the liquid is completely wetting to the wall, the interface starts from a shape close to a semi-sphere. Upon the impact, the interface near the wall moves upwards due to inertia. At  $\tau = 1$ , the fluids near the wall are lifted and have an upward velocity. At  $\tau = 2$ , due to the deceleration of the tube, the fluids near the wall move downward. The

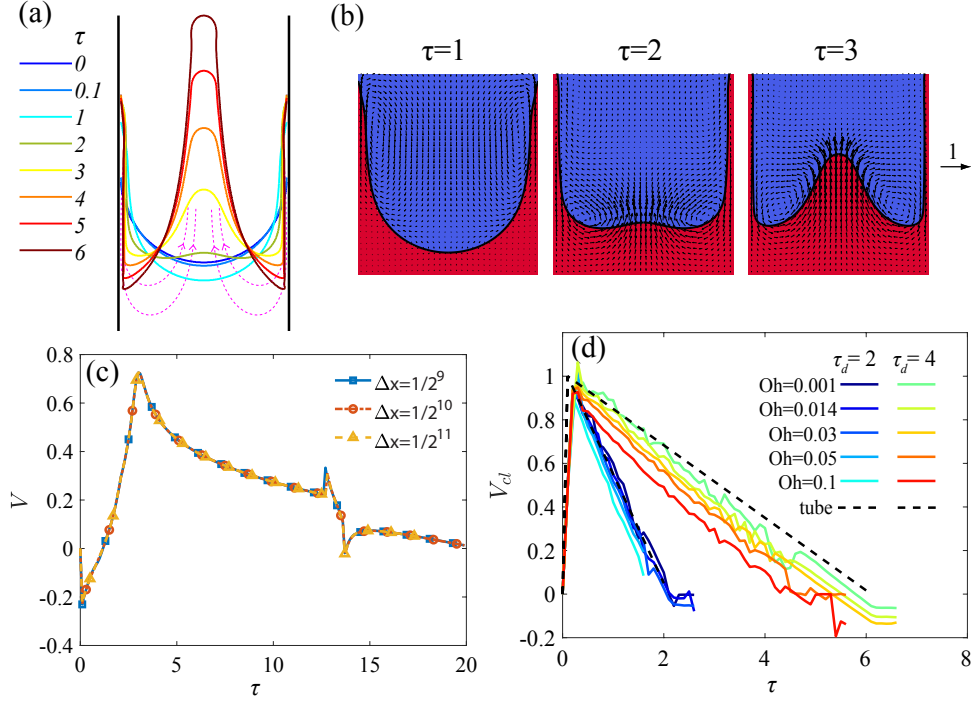


**Figure 2.5.** (a) The time evolution of the liquid-gas interface. Dashed lines show the streamlines at  $\tau = 3$ . The color bar indicates the time corresponding to different profiles. (b) The corresponding time evolution of the velocity field in the liquid jet. The time is annotated at the top of each frame. The scale of the velocity vector is denoted by the arrow on the right. Here,  $Oh = 0.014$ ,  $We = 2000$ ,  $\tau_d = 2$ ,  $\tau_a = 0.1$  and  $Bo = 0$ . (c) The interface velocity at the tube center  $V$  is independent of the refined grid size near the liquid-gas interface  $\Delta x$ . Here,  $Oh = 0.014$ ,  $We = 1000$ ,  $\tau_d = 2$ ,  $\tau_a = 0.1$  and  $Bo = 14.5$ . (d) The velocity of the interface near the tube wall in the tube reference frame  $V_{cl}$  follows the tube velocity in the laboratory reference frame (dashed line) for small  $\tau_d$  and  $Oh$ , corresponding to the inviscid limit for the motion of contact line.  $V_{cl}$  is slightly lower than the tube velocity for larger  $\tau_d$  and  $Oh$  due to the effect of fluid viscosity. Here,  $We = 2000$ ,  $\tau_a = 0.1$  and  $Bo = 14.5$ .

flow focuses at the center of the tube with a vortex forming near the interface. The liquid jet forms as the fluid in the center of the tube rises, which is subsequent to the deceleration motion of the tube.

Fig. 2.5(c) shows the interface velocity at the tube center for different grid size  $\Delta x$  near the liquid-gas interface in our simulations. The interface velocity is independent of the grid size  $\Delta x$  for  $\Delta x < 1/2^{10}$ . The center of the interface gains a downward velocity during the

tube acceleration, and then reverts to upward after the tube deceleration. A liquid jet forms at the center. Jet pinch-off occurs at  $\tau \approx 13$  and introduces a singular interface velocity at the center of the tube. The interface velocity presented here is measured at  $1/64$  away from the axis to avoid this singularity. The simulation results are independent of the grid size for  $\Delta x < 1/2^{10}$ . For grid size larger than  $1/2^{10}$ , there is a slight difference in the interface velocity near the jet pinch-off points, where the characteristic length scale of the flow is small.

The velocity of the contact line between the liquid and the wall in the reference frame of the tube, which is denoted as  $V_{cl}$ , is compared with the tube velocity in Fig. 2.5(d). Here, The acceleration induces a pressure impulse in the liquid. The liquid near the corner formed by the interface and the wall gains an initial velocity. The acceleration is applied in a very short time so that the liquid in the corner is dominated by inertia. In our problem, where the contact angle between the wall and the interface is 1 degree, we observe that for small  $\tau_d$  and Oh, the velocity of contact line approximates the same magnitude of the tube velocity but of the opposite direction. Thus, the contact line is almost stationary in the laboratory reference frame. This is because for the small acceleration and deceleration times in the simulation, the flow near the contact line approximates to an inviscid flow and there is a slip on the wall near the contact line [44]. This agrees with the pressure-impulse theory [40] and the analysis of sessile drop [45] where the inviscid flow theory is used. For larger  $\tau_d$  and Oh, this velocity is slightly lower than the tube velocity due to the viscous effects, since the viscous effects usually increase with the elapsed time and the fluid viscosity. This agrees with the experimental findings by Onuki et al. [42] that the viscous effects are negligible during the impact interval but are important for the jet generation.

### 2.4.3 Effects of the time of acceleration and deceleration process

The interface velocity at the center of the tube slightly increases with the acceleration time  $\tau_a$  (Fig. 2.6(a)). In the limit of very small acceleration time, the pressure-impulse theory implies that the initial fluid momentum induced by acceleration is proportional to the impact velocity [40]. In the original work of pressure-impulse theory, both the impact and the fluid

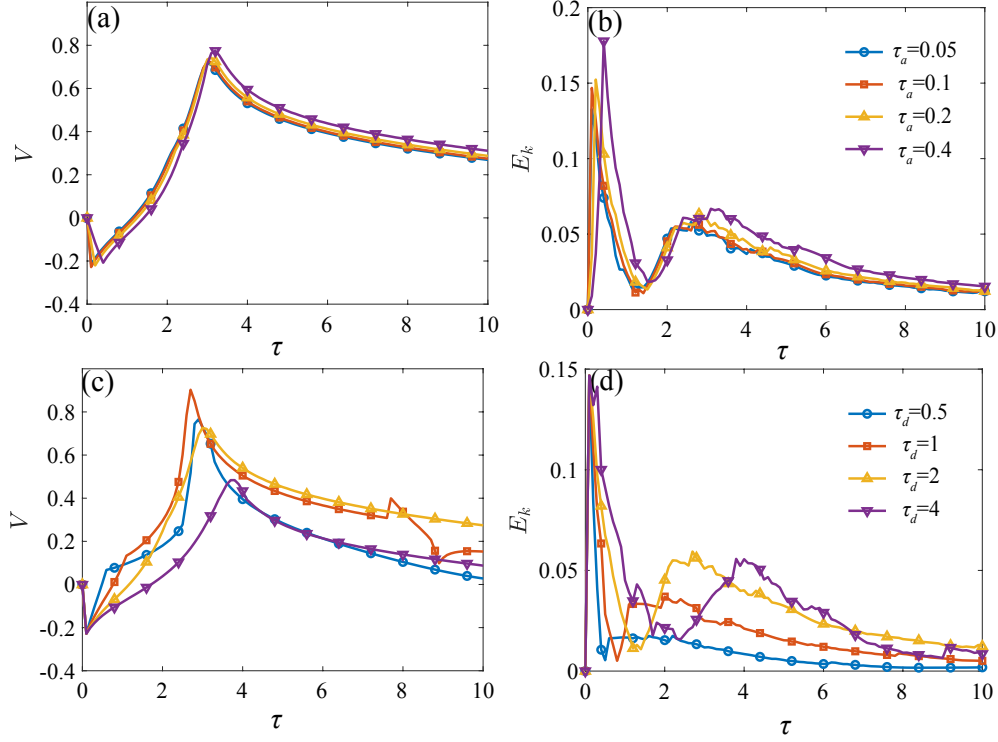


**Figure 2.6.** (a) The interface velocity at the tube center and (b) the total kinetic energy of the liquid for different acceleration time  $\tau_a$  at  $\tau_d = 2$ . In our experiments, the time of the acceleration induced by the rod impact is much smaller than the deceleration time, which corresponds to the limit of very small acceleration time  $\tau_a < 0.2$ . (c) The interface velocity at the tube center  $V$  and (d) the total kinetic energy of the liquid for different deceleration time  $\tau_d$  at  $\tau_a = 0.1$ . Here,  $Oh = 0.014$ ,  $We = 1000$ , and  $Bo = 14.5$ .

momentum are upwards. Because the equations solved in the pressure-impulse theory are linear, the theory also works for our case where both impact and the fluid momentum are downwards. The ratio between the magnitude of fluid momentum and the impact velocity is a constant only depending on the interface geometry even if the impact direction is reversed. For  $\tau_a \rightarrow 0$  and  $Bo = 14.5$ , the interface velocity at the tube center after acceleration is about 0.22 times the impact velocity. For zero Bond number in Fig. 2.7(a), this value is around 0.75, which is close to the analytical result for a hemisphere [40]. When acceleration time increases, the interface velocity at the tube center after the acceleration process slightly decreases. The maximum interface velocity occurs during the jet formation process at  $\tau \approx 3$ .

The maximum interface velocity increases with the acceleration time. The acceleration time in experiments corresponds to  $\tau_a \approx 0.2$ , which is small compared to the deceleration time.

The time evolution of the liquid kinetic energy for different acceleration time is shown in Fig. 2.6(b). The liquid gains the most kinetic energy during the short-time acceleration process. The kinetic energy gained by the liquid increases with the acceleration time  $\tau_a$ , because during the acceleration process, the interface is deformed and the curvature of the interface increases with the elapsed time. The body force due to acceleration exerted on the deformed interface induces more kinetic energy in the liquid. Then during the tube deceleration, the kinetic energy decreases and then increases. The kinetic energy reaches its local maximum when the jet starts forming and the interface velocity at tube center reaches the maximum. The local maximum kinetic energy increases with the acceleration time, which explains why the maximum interface velocity increases with the acceleration time in Fig. 2.6(a). Here, the kinetic energy is calculated by integrating  $u^2 V_c$ , where  $u$  is the local fluid velocity and  $V_c$  is the cell volume that is occupied by the liquid.

Fig. 2.6 (c)(d) demonstrate that the jet velocity and kinetic energy of the liquid have a non-monotonic dependence on the deceleration time  $\tau_d$ . Both the jet velocity and the liquid kinetic energy increase with  $\tau_d$  and then decreases. The jet velocity reaches the maximum value at  $\tau_d = 1$  while the kinetic energy reaches the maximum value at  $\tau_d = 2$ . The non-monotonic  $\tau_d$  dependence for the jet velocity and kinetic energy stems from the deformation of the interface. After the tube acceleration, the fluids near the tube wall is rising and the interface curvature increases with time. The body force due to the deceleration is more effective in generating a focusing flow if it is acting on a curved interface. Therefore, for small  $\tau_d$ , the interface velocity and liquid kinetic energy increases with  $\tau_d$ . In an extreme case where both acceleration and deceleration times are very small, the pressure impulse theory [40] indicates that the momentum changes of the liquid due to acceleration and deceleration balance each other, leading to zero interface velocity after the tube motion. On the other hand, when  $\tau_d$  is large, deceleration is mostly acting on a fully deformed interface. Larger deceleration exerted on the fully deformed interface is more effective in generating the focusing flow. Since the deceleration magnitude is inversely proportional to  $\tau_d$ , the interface velocity and the kinetic energy decrease with  $\tau_d$ . The tip of the liquid jet make up only a

small volume of the whole liquid, therefore, the interface velocity and kinetic energy reach the maximum value at different  $\tau_d$ . The maximum interface velocity can be very different for the same value of kinetic energy. For  $\tau_d = 0.5$ , the maximum interface velocity is large, meaning that the momentum of the liquid is more focused at the tube center, while for  $\tau_d = 4$  the maximum interface velocity is smaller, where the momentum of the liquid is less focused at the tube center. Here, only the jet at  $\tau_d = 1$  pinches off, which also has the largest maximum interface velocity. To reduce the parameter space, we focus on the simulations in small  $\tau_a$  regime and  $\tau_a = 0.1$  is used for the following simulations.

#### 2.4.4 Scaling laws for the jet velocity

Here, we investigate the dependence of the jet velocity on the fluid viscosity (Oh), surface tension (We) and deceleration time ( $\tau_d$ ) without gravitational effects (Bo=0). The time evolution of the interface velocity for different Ohnesorge numbers are shown in Fig. 2.7(a). For  $\tau < 2$ , the interface velocity is independent of Oh, suggesting that the viscous effects do not influence the jet dynamics before the flow is focusing at the center of the tube. For  $\tau > 2$ , the interface velocity decreases with Oh. The liquid jet forms when the interface velocity reaches the maximum value. The time for reaching the maximum velocity evaluates the time for the jet formation process, which show a slight decrease with Oh and a strong increase with  $\tau_d$ . When  $\tau_d$  increases, it takes longer time for the interface velocity to reach the maximum value and the maximum interface velocity decreases.

We define the maximum value of the interface velocity as the jet velocity  $V_j$ . The dependence of  $V_j$  on Oh, We and  $\tau_d$  are shown in Fig. 2.7(b). When  $\text{Oh} \rightarrow 0$ ,  $V_j$  approaches the inviscid jet velocity  $V_{j,0}$ , which is proportional to the momentum gained by the center of the interface during the tube acceleration-deceleration motion.  $V_{j,0}$  decreases with  $\tau_d$  for  $\tau_d > 2$  and slightly increases with We. In simulations for the inviscid jet ( $\text{Oh} = 0$ ), surface waves of small wavelengths persist after the impact and introduce oscillations in the interface velocity. The inviscid jet velocity  $V_{j,0}$  is approximated by the jet velocity at  $\text{Oh} = 0.001$ . For a viscous jet, the jet velocity  $V_j$  is always smaller than  $V_{j,0}$  due to viscous dissipation in the liquid.

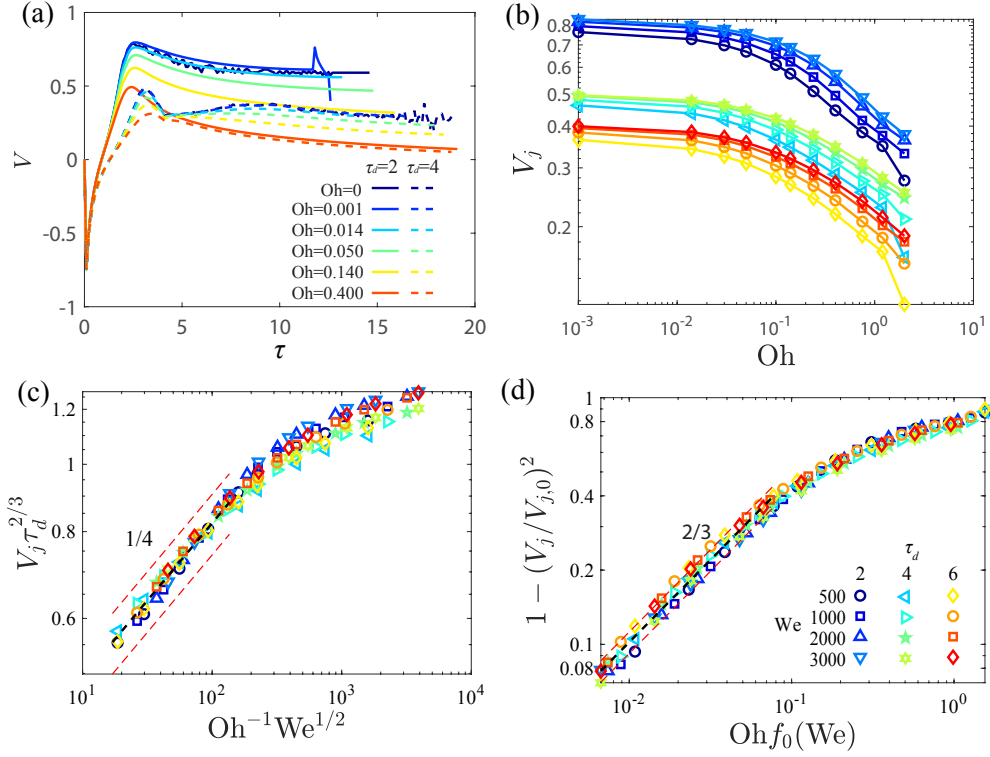


**Figure 2.7.** Jet velocity without gravity effects ( $Bo=0$ ,  $\tau_a = 0.1$ ). (a) The interface velocity at the tube center for different  $Oh$  and  $\tau_d$ . When the jet forms ( $\tau \approx 2.6$  for  $\tau_d = 2$ , and  $\tau \approx 3.2$  for  $\tau_d = 4$ ), the interface velocity reaches a maximum value, which is defined as the jet velocity  $V_j$ . (b) The jet velocity  $V_j$  versus  $Oh$  for different  $We$  and  $\tau_d$ . (c) The jet velocity for small  $Re$  collapses on a single curve when  $V_j \tau_d^{2/3}$  is plotted versus  $Oh^{-1} We^{1/2}$ . (d) For large  $Oh$ ,  $[1 - (V_j/V_{j,0})^2]$  scales with  $[Oh f_0(We)]^{2/3}$ , where  $f_0(We)$  evaluates the effect of  $We$  to the viscous dissipation at  $Bo = 0$ . (b-d) shares the same legend in (d). The red dashed lines show the 10% error away from the scaling (black dashed line).

We then collapsed the jet velocity data in two different ways. For highly viscous fluids, the jet velocity can be expressed as

$$V_j \sim \tau_d^{-0.6448} Oh^{-0.2264} We^{0.1239}, \quad (2.1)$$

where the exponents are obtained from the multivariate least squares fitting for data within  $Oh^{-1} We^{1/2} < 100$ . By approximating the exponents with the nearest fractional numbers, we

collapse the data on the plot of  $V_j \tau_d^{2/3}$  versus  $\text{Oh}^{-1} \text{We}^{1/2}$  (Fig. 2.7(c)) with the jet velocity scaling expressed as

$$V_j \sim \tau_d^{-2/3} \text{Oh}^{-1/4} \text{We}^{1/8}, \text{ for } \text{Oh}^{-1} \text{We}^{1/2} < 100. \quad (2.2)$$

This scaling describes the small jet velocity at large Oh and small We. Most of the liquid kinetic energy obtained during the acceleration-deceleration process is dissipated due to viscous effects, thus the jet velocity  $V_j$  can directly scale with  $\text{Oh}^{-1/4}$ . In the small Oh regime, the jet velocity data does not fully collapse because of the surface tension effects during the jet formation. As Oh decreases, the jet velocity data  $V_j \tau_d^{2/3}$  approaches  $V_{j,0} \tau_d^{2/3}$ , which shows a dependence on We.

For a small Oh regime, we investigate the normalized reduction of the kinetic energy in jet tip  $[1 - V_j^2/V_{j,0}^2]$ , which approaches zero for  $\text{Oh} = 0$ . As is shown in Fig. 2.7(d),  $[1 - V_j^2/V_{j,0}^2]$  is hardly dependent on the deceleration time  $\tau_d$ , thus can be collapsed on a single curve when it is plotted against  $\text{Oh} f_0(\text{We})$ ,

$$1 - (V_j/V_{j,0})^2 \sim [\text{Oh} f_0(\text{We})]^{2/3}, \text{ for } \text{Oh} f_0(\text{We}) < 0.1, \quad (2.3)$$

where  $f_0(\text{We}) \equiv f(\text{We}, \text{Bo} = 0) = 7.17 \text{We}^{-0.406} + 0.2$  with  $f(\text{We}, \text{Bo})$  being a function of We and Bo and  $f_0(\text{We})$  is the value at zero Bond number. The formula of  $f(\text{We}, \text{Bo})$  is discussed in the next section.

#### 2.4.5 Effects of gravity

Gravity affects the jet formation process in two ways: it flattens the liquid-air interface at the initial state and the gravitational force acts as a source term in the momentum equation. Fig. 2.8 shows the velocity at the center of the interface  $V$  and the liquid kinetic energy  $E_k$  when the initial interface is flattened by gravity. The shape of the initial interface is determined by the Bond number. To separate the effects of the gravitational force from the effects of the initial interface perturbation caused by gravity, we also calculated the results with the same initial interface shape but without the gravitational force. When the initial

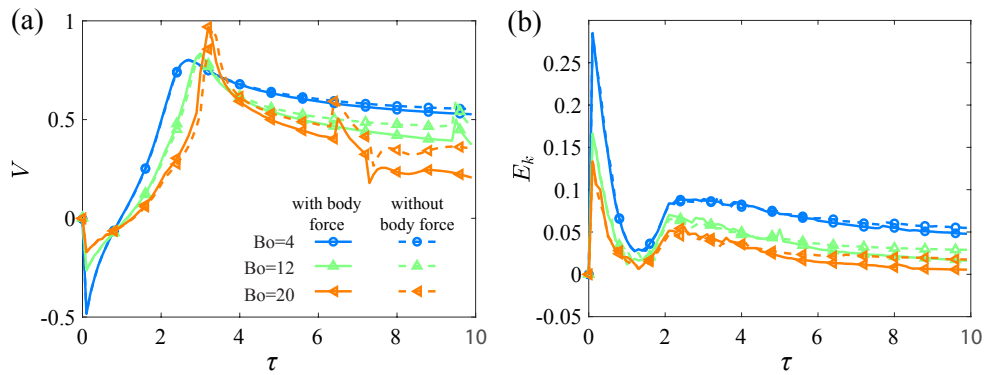


**Figure 2.8.** The time evolution of (a) the velocity at the center of the interface and (b) the liquid kinetic energy when the initial interface is modified by gravity, whose magnitude is indicated by  $Bo$ . The solid line includes the gravitational force, while for the dashed line, the gravitational force is excluded. Here,  $Oh = 0.014$ ,  $We = 1000$  and  $\tau_d = 2$  and  $\tau_a = 0.1$ .

interface is flattened by gravity, the focusing flow is enhanced and the fluid velocity at the center of the interface can reach larger maximum value. The jet velocity is hardly affected by the gravitational force term for  $Bo < 20$ . Here, the ratio between the body force term of gravity over deceleration  $gt_d/U = Bo\tau_d/We$  is less than 0.04. The gravitational force is very small compared to the body force due to the tube deceleration, but when the tube is stopped, the liquid jet is still subject to the gravitational force and its velocity decreases. After the jet is formed, the flow velocity inside the jet is decreased by the gravitational force, and the effect of gravity increases with time. During the jet formation process, the jet velocity is only slightly decreased by gravitational force, but for the jet pinch-off, which occurs later in time, the gravitational force is important in decreasing the jet velocity. Among all the presented cases, the jet only breaks up for  $Bo = 20$  whether the gravitational force term is included or not. This suggests that the gravity affects the jet pinch-off mainly by modifying the initial interface shape. When the initial interface is flattened by gravity, the inviscid jet velocity increases, which enhances the breakup of liquid jet. The corresponding kinetic energy of the liquid is shown in Fig. 2.8(b). When the initial interface is flattened by gravity, the liquid gains less kinetic energy from the tube acceleration. Even though the total amount of kinetic energy is smaller in the bulk of the liquid, the interface velocity at the center is larger. This suggests that gravity helps liquid momentum to be more focused at the tip of the liquid jet.

The inviscid jet velocity  $V_{j,0}$  and jet formation time  $t_{j,0}$  for different  $Bo$  and  $We$  are demonstrated in Fig. 2.9. When  $Bo$  increases, both  $V_{j,0}$  and  $t_{j,0}$  increases, and their dependence on  $We$  is dependent on  $Bo$ . An example of the time evolution of the interface shape is shown in Fig. 2.9(c). When  $Bo$  increases, the initial interface is flattened. Only the interface near the wall is perturbed. At  $\tau = 2$ , the initial perturbation evolves into a surface wave after the acceleration-deceleration motion of the tube. The surface wave propagates towards the center of the tube and then collapses, facilitating the formation of the liquid jet. The formation of the surface wave is more obvious for  $Bo = 100$ , where the initial interface is flattened by gravity and the flow focusing effects is suppressed. Here, the surface

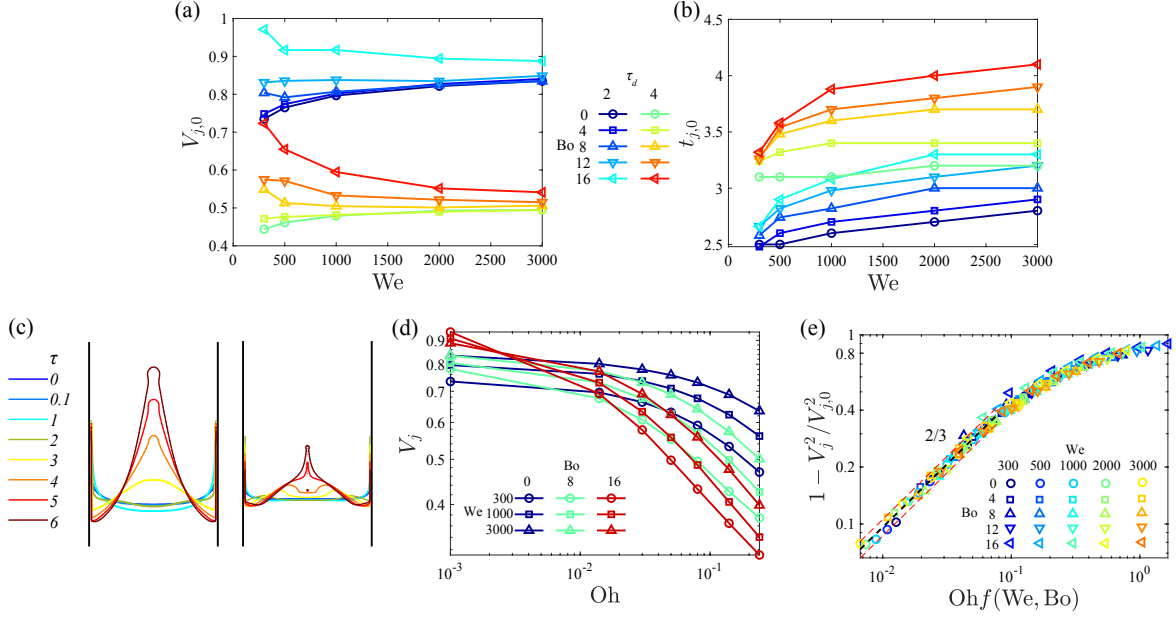


**Figure 2.9.** (a) The inviscid jet velocity  $V_{j,0}$  and (b) the dimensionless time when the maximum interface velocity occurs for different  $We$ ,  $Bo$  and  $\tau_d$ . (c) The time evolution of the interface for  $Bo = 16$  (left) and  $Bo = 100$  (right). A slight surface wave occurs at  $\tau = 2$  for  $Bo = 16$  and this surface wave is more obvious for  $Bo = 100$ . Here,  $We = 2000$ ,  $Oh = 0.014$ ,  $\tau_d = 2$ ,  $\tau_a = 0.1$ . (d) The jet velocity  $V_j$  as a function of  $Oh$  for different  $Bo$ ,  $We$ . (e) The jet velocity data are collapsed on a single curve in the plot of  $[1 - V_j^2/V_{j,0}^2]$  versus  $Ohf(We, Bo)$ , where  $f(We, Bo) = (Bo^{1.48} + 7.17)We^{-0.406} + 0.20$  is an empirical function that evaluates the focusing effect of the flow and is obtained by using a least square fit. Red dashed lines indicate 10% error from the scaling. Here,  $\tau_d = 2$ ,  $\tau_a = 0.1$ .

wave is generated by the acceleration-deceleration process due to the body force term. The dispersion relationship reads as

$$\tilde{\omega}^2 = \tilde{a}_d \tilde{k} + \frac{\sigma}{\rho} \tilde{k}^3, \quad (2.4)$$

where  $\tilde{\omega}$  is the dimensional phase angular speed,  $\tilde{k}$  is the dimensional wave number, and  $\tilde{a}_d$  is the dimensional acceleration due to the body force exerted on the liquids. During the deceleration process,  $\tilde{a}_d = U/t_d + g$ . After deceleration, only gravity is present  $\tilde{a}_d = g$ . By using the scaling  $\tilde{\omega} = \omega U/R$  and  $\tilde{k} = k/R$ , the non-dimensional form of the dispersion relation is

$$\omega^2 = a_d k + \text{We}^{-1} k^3, \quad (2.5)$$

where  $a_d = \tau_d^{-1} + \text{Bo}/\text{We}$  during deceleration and  $a_d = \text{Bo}/\text{We}$  after deceleration. For  $\text{Bo} = 100$  in Fig. 2.9(c), the half wavelength normalized by the tube radius is about 0.65, thus,  $k = \pi/0.65 = 4.8$ . The peak of the wave moves with the phase velocity. The steady-state phase velocity is  $c = \omega/k$ , which is 0.34 during deceleration process and 0.11 after deceleration. This means that the wave propagates with speed 0.34 during deceleration process and then decreases to 0.11 after the deceleration process. In Fig. 2.9(c), the deceleration stops at  $\tau_d + \tau_a = 2.1$ . The average wave velocity is measured 0.24 for time between 2 and 3 and 0.14 for time between 3 and 4, which agree with the calculation above.

The inviscid jet velocity and jet formation time are larger than those at  $\text{Bo} = 0$ , where the jet formation process is dominated by the flow focusing effect. At  $\text{Bo} = 16$ , when the surface tension increases, i.e.,  $\text{We}$  decreases, the inviscid jet velocity  $V_{j,0}$  increases and the jet formation time  $t_{j,0}$  decreases, which contrasts with the jet induced by the focusing flow at  $\text{Bo} = 0$ , where  $V_{j,0}$  decreases and  $t_{j,0}$  slightly decreases. The dependence of the jet velocity on  $\text{We}$  depends on the initial interface shape and the Bond number. When the Bond number increases, the jet formation process is enhanced by the collapse of surface wave. The Oh dependence of the jet formation time  $t_j$  can be informed from Fig. 2.7(a).  $t_j$  slightly decreases with Oh for most of our investigated cases, but this decrease can become important for large  $\tau_d$ , where the viscous effects are dominant. Similarly, a contact angle close to  $90^\circ$  also flattens

the initial interface shape and reduces the flow focusing effects. For a contact angle slightly less than  $90^\circ$  or very large Bond numbers, only a small part of the interface near the wall is initially perturbed. We can expect that the focusing flow is suppressed and the jet formation process is dominated by the collapse of surface wave.

The jet at large Bond numbers (Fig. 2.9(c)) is thinner than the jet at  $Bo = 0$  (Fig. 2.5(a)), suggesting that the interface velocity is more focused at the center. The flow is more susceptible to the viscous dissipation in the liquid. In Fig. 2.9(d), the jet velocity  $V_j$  decreases more rapidly with  $Oh$  when  $Bo$  increases and  $We$  decreases. Here, the surface wave stores more kinetic energy, and more liquid momentum is focused at the center of the tube. For a large  $Oh$ , the jet velocity increases with  $Bo$  and decreases with  $We$ . While for a more viscous liquid with large  $Oh$ , the fluid viscous effects are important, the jet velocity decreases with  $Bo$  and increases with  $We$ . For intermediate  $Oh$ , the jet velocity can display a non-monotonic dependence on  $Bo$  and  $We$ .

In Fig. 2.9(e), we successfully collapsed the data on a single curve in the plot of  $[1 - V_j^2/V_{j,0}^2]$  versus  $Ohf(We, Bo)$ , where  $f(We, Bo) = (Bo^{1.48} + 7.17)We^{-0.406} + 0.20$  evaluates the effects of  $Bo$  and  $We$  on the viscous dissipation. The form of the equation is based on the observation that  $[1 - V_j^2/V_{j,0}^2]$  increases with  $Bo$  and decreases with  $We$ . At large  $Bo$ ,  $[1 - V_j^2/V_{j,0}^2]$  decreases more rapidly with  $We$ , thus we come up with this formula for  $f(We, Bo)$ . The constants and exponents are obtained through a least-square fit. The results here extend the scaling in Fig. 2.7(c) to nonzero Bond numbers,

$$1 - (V_j/V_{j,0})^2 \sim [Ohf(We, Bo)]^{2/3}, \text{ for } Ohf(We, Bo) < 0.09. \quad (2.6)$$

At small  $Oh$ , the normalized reduction of kinetic energy in the jet tip  $[1 - V_j^2/V_{j,0}^2]$  scales with  $Oh^{2/3}$  regardless  $Bo$ ,  $We$  and  $\tau_d$ . At large  $\tau_d$  and  $Bo$ , the gravitational force can be comparable to the body force from deceleration motion, causing the jet velocity to deviate from the scaling.  $f(We, Bo)$  evaluates the focusing effects of the flow, which increases with  $Bo$  and decreases with  $We$ . When  $Bo$  increases, the jet formation process is more dominated by the collapse of the surface wave, where  $f(We, Bo)$  decreases more rapidly with  $We$ . The scaling of the jet velocity applies to all the cases in our problem regardless of  $Oh$ ,  $We$  and

$\tau_d$  except for  $\tau_d < 1.5$ , where the jet behavior is different and the corresponding explanation is offered later.

## 2.4.6 Criteria for jet breakup

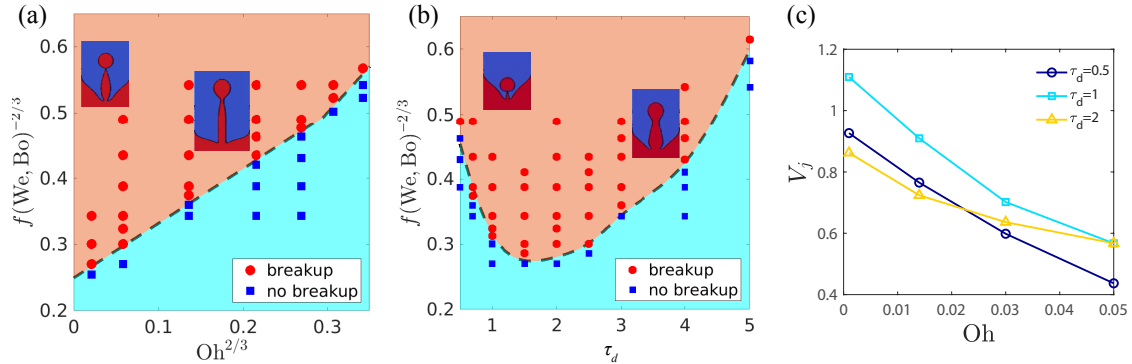


**Figure 2.10.** Study of breakup criteria at  $Bo = 14.5$  and  $\tau_a = 0.1$ . (a) Phase diagram of jet breakup at  $\tau_d = 2$ . Insets are two snapshots of the jet shape before breakup for  $Oh = 0.014, We = 400$  (left) and  $Oh = 0.14, We = 1800$  (right). (b) Phase diagram at  $Oh = 0.014$ . Insets show the jet shape before breakup for  $\tau_d = 1, We = 350$  (left) and  $\tau_d = 4, We = 1200$  (right). (c) The jet velocity shows a non-monotonic dependence on  $\tau_d$  at  $We = 1000$ .

The liquid jet can break up due to the Rayleigh-Plateau instability. As is illustrated in Fig. 2.4, the jet breaks up above a critical Weber number  $We_c$ . We also find that the time instant of pinch-off is postponed with decreasing  $We$ . At  $We_c$ , the jet pinches off right before the jet disappears into the bulk liquid. The critical Weber number  $We_c$  in Fig. 2.4 is a little above 505, since the jet is about to pinch off at  $\tau = 15.26$  for  $We=505$ . The time scale of the jet pinch-off is about one order of magnitude larger than that of the jet formation process. As we discussed previously, the effects of viscous dissipation and gravitational force increase with the elapsed time. The viscous dissipation and gravitational force are usually important in the jet pinch-off process.

Given the jet velocity scaling in Eq. (2.6), we plotted the phase diagram of jet breakup in space between  $f(\text{We}, \text{Bo})^{-2/3}$  and  $\text{Oh}^{2/3}$  (Fig. 2.10(a)). For  $\text{Oh}^{2/3}$  less than 0.3, the breakup and non-breakup regions can be separated by a straight line expressed as

$$f(\text{We}_c, \text{Bo})^{-2/3} - f(\text{We}_{c,0}, \text{Bo})^{-2/3} \sim \text{Oh}^{2/3}, \quad (2.7)$$

where  $\text{We}_{c,0}$  is the critical Weber number at  $\text{Oh} = 0$ , and  $f(\text{We}_{c,0}, \text{Bo})^{-2/3}$  is the y-intercept of the line, which is nonzero because the liquid jet has to overcome the gravitational force before it pinches off.  $f(\text{We}_c, \text{Bo})^{-2/3}$  linearly increases with  $\text{Oh}^{2/3}$ . For larger  $\text{Oh}$ , the slope between  $f(\text{We}_c, \text{Bo})^{-2/3}$  and  $\text{Oh}^{2/3}$  increases. The insets show the interface shape for the jet just above the critical Weber number. For the jet of small  $\text{Oh}$ , the radius of the interface at the bottom of the jet decreases and there is a tendency for the formation of a satellite droplet. While for the jet of large  $\text{Oh}$ , the shape of the liquid jet is close to a cylinder.

Phase diagram for jet breakup in the space formed by  $f(\text{We}, \text{Bo})^{-2/3}$  and  $\tau_d$  shows two different regimes: for  $\tau_d < 1.5$ ,  $f(\text{We}_c, \text{Bo})^{-2/3}$  decreases with  $\tau_d$ , while for  $\tau_d > 1.5$ ,  $f(\text{We}_c, \text{Bo})^{-2/3}$  increases with  $\tau_d$  (Fig. 2.10(b)). The breakup of the jet is related to the jet velocity in the jet formation process. In Fig. 2.10(c), the jet velocity at  $\tau_d = 1$  is larger than  $\tau_d = 0.5$  and 2 for  $\text{Oh} < 0.05$ , suggesting that the jet velocity increases with  $\tau_d$  first and then decreases. The jet velocity has the maximum value for  $\tau_d \approx 1$ , which agrees with the results in the phase diagram where the critical  $\text{We}$  is minimum at  $\tau_d \approx 1.5$ . The non-monotonic dependence of  $V_j$  on  $\tau_d$  has also been discussed in Fig. 2.6. In Fig. 2.10(c), the flow of  $\tau_d < 1.5$  are more susceptible to liquid viscous dissipation. The jet velocity  $V_j$  decreases more rapidly with  $\text{Oh}$ . For large  $\text{Oh}$ , the jet velocity at  $\tau_d = 2$  can become larger than that at  $\tau_d = 1$ . We also find that  $V_{j,0}$  reaches its maximum value at  $\tau_d = 1$ , which means that the traveling distance of the tube is 1/4 of the tube diameter. The maximum  $V_{j,0}$  is larger than 1, meaning that the jet velocity measured in the reference frame of the tube is larger than the maximum moving speed of the tube. As we previously discussed, this velocity can further increase if  $\tau_a$  increases or  $\text{We}$  decreases. The combination of focusing flow and collapse of surface wave effects help the flow momentum to focus at the center of the interface. The maximum jet velocity can be larger than the maximum moving speed of the tube.

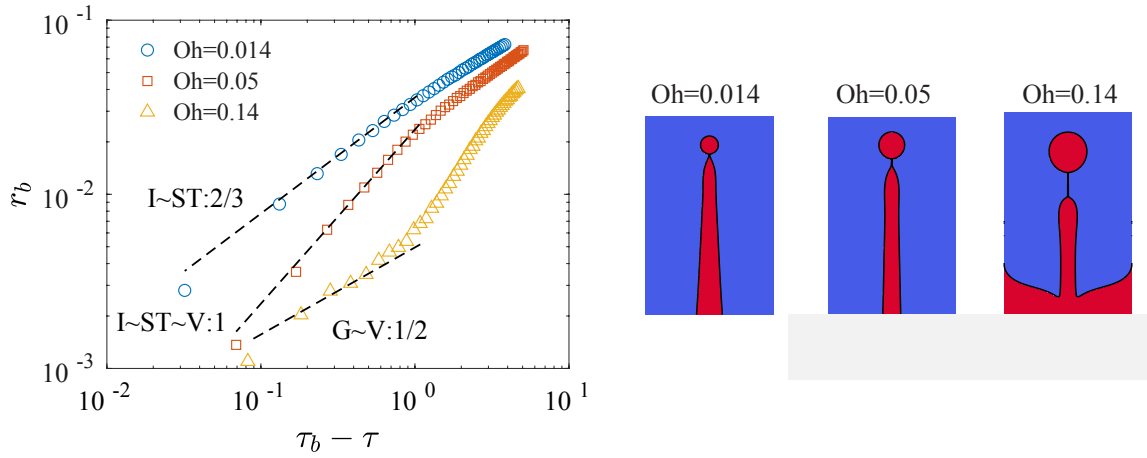


**Figure 2.11.** The neck radius at the breakup point  $r_b$  plotted versus the time before breakup  $\tau_b - \tau$ , where  $\tau_b$  is the time when the jet breaks. At  $Oh=0.014$ ,  $r_b$  scales with  $(\tau_b - \tau)^{2/3}$ , corresponding to the scaling for inviscid pinch-off where liquid inertia (I) is balanced by surface tension (ST) [46], [47]. At  $Oh=0.05$ ,  $r_b$  scales with  $(\tau_b - \tau)$ , corresponding to the scaling for viscous pinch-off where inertia (I), surface tension (ST) and viscous (V) effects balance each other [48]. At  $Oh=0.14$ ,  $r_b$  scales with  $(\tau_b - \tau)^{1/2}$  where gravity (G) is balanced by viscous (V) effects [49]. The panels on the right shows the interface profile before pinch-off. Here,  $Bo = 14.5$ ,  $We = 2000$ ,  $\tau_d = 2$ , and  $\tau_a = 0.1$ .

The breakup of the liquid jet is a singular phenomenon where the flow length scale approaches zero. The flow field near the breakup point is usually described by similarity solutions [29] that are independent of the flow in the outer regions. In Fig. 2.11, we investigate the radius at the breakup point as a function of the dimensionless time before breakup ( $\tau_b - \tau$ ). The value of  $\tau_b$  is estimated by extrapolating the last three data points before breakup using a spline fit, and is 11.83, 22.07, and 51.68 for  $\text{Oh}=0.014$ , 0.05, and 0.14. At  $\text{Oh} = 0.014$ , the radius scales with  $(\tau_b - \tau)^{2/3}$ , which agrees with the scaling in the inviscid breakup [46], [47]. Here, the liquid inertia is balanced by the surface tension effects and fluid viscosity is negligible. As  $\text{Oh}$  increases to 0.05, the viscous effects increase to the same magnitude with inertial and surface tension effects, the radius scales with  $(\tau_b - \tau)$ , which corresponds to the scaling in viscous breakup [48]. As  $\text{Oh}$  increases to 0.14, the radius scales with  $(\tau_b - \tau)^{1/2}$  right before the breakup, which agrees with the solution for the dripping of a viscous liquid [49]. Here, liquid viscous effects is balanced by gravity. The panel on the right shows the interface profile before breakup for the three different  $\text{Oh}$ . The droplet size increases with  $\text{Oh}$  and the thin thread beneath the droplet elongates with increasing  $\text{Oh}$ . The length scale of the breakup regime is increasing with  $\text{Oh}$ . At large  $\text{Oh}$ , gravity starts to play an important role in this regime.

## 2.5 Conclusion

We investigated the jet formation process when a tube is subject to a sudden acceleration motion and is then gradually decelerated to stop. The numerical simulations are validated using experiments. We find that rise of the contact line is dominated by inertia and the viscous effects only play a role in the jet formation and pinch-off process, because the time scale of these processes is larger than the deceleration time. For liquid jet with the acceleration time being much smaller than the deceleration time, we collected the jet velocity data for different  $\text{Oh}$ ,  $\text{Bo}$ ,  $\text{We}$ , and  $\tau_d$  and obtained the scaling law of the jet velocity for both low  $\text{Oh}$  and high  $\text{Oh}$  regimes by fitting the numerical results. The scaling is also extended to non-zero Bond numbers. For large Bond number, a surface wave collapses during the jet formation process. The  $\text{We}$  dependence of jet velocity is associated with  $\text{Bo}$ , while the viscous dissipa-

tion in the flow scales as  $\text{Oh}^{2/3}$ . For the breakup of the liquid jet,  $f(\text{We}_c, \text{Bo})^{-2/3}$  shows a linear increase with  $\text{Oh}^{2/3}$  for a wide range of  $\text{Oh}$ . But  $f(\text{We}_c, \text{Bo})^{-2/3}$  has a non-monotonic dependence on  $\tau_d$ , where the liquid jet is more likely to breakup for  $\tau_d \approx 1.5$ .

The present study lays the foundation for understanding the jet dynamics induced by a sudden movement, and the conclusions here can be applied to analyze the droplet formation and sloshing dynamics in pharmaceutical, aerospace and transportational industries. For example, in the administration of autoinjectors, the syringe is usually impacted by a high tension spring, generating liquid droplets that potentially affect the functionality of the pharmaceuticals. Our breakup phase diagrams imply that the droplet formation can be reduced if we allow the syringe to decelerate in a longer time or if the liquid has a higher viscosity. Furthermore, liquid jets induced by a sudden movement is a very complicated problem and many aspects of this problem are still underexplored, such as the effects of the contact angle, and fluid compressibility. In the near future, we expect more experimental and theoretical works in this area regarding the jet scaling analysis, jet breakups, and the formation of secondary structures such as splash and crown.

### 3. THE INTERFACE MOTION AND HYDRODYNAMIC SHEAR OF THE LIQUID SLOSH IN SYRINGES

*This chapter is reproduced with permission from:*

*Zhang, Y., Han, D., Dou, Z., Veilleux, J.C., Shi, G.H., Collins, D.S., Vlachos, P.P. and Ardekani, A.M., 2021. The Interface Motion and Hydrodynamic Shear of the Liquid Slosh in Syringes. Pharmaceutical Research, pp.1-19. The experiments are conducted by Zhongwang Dou.*

#### 3.1 Summary

Interface motion and hydrodynamic shear of the liquid slosh during the insertion of syringes upon autoinjector activation may damage the protein drug molecules. Experimentally validated computational fluid dynamics simulations are used in this study to investigate the interfacial motion and hydrodynamic shear due to acceleration and deceleration of syringes. The goal is to explore the role of fluid viscosity, air gap size, syringe acceleration, syringe tilt angle, liquid-wall contact angle, surface tension and fill volume on the interface dynamics caused by autoinjector activation. A simplified -autoinjector platform submerged in water is built to record the syringe and liquid motion without obstruction of view. The syringe kinematics is imported to the simulations based on OpenFOAM InterIsoFoam solver, which is used to study the effects of various physical parameters. The simulations agree with experiments on the air-liquid interface profile and interface area. The interfacial area and the volume of fluid subject to high strain rate decreases with the solution viscosity, increases with the air gap height, syringe velocity, tilt angle and syringe wall hydrophobicity, and hardly changes with the surface tension and liquid column height. The hydrodynamic shear mainly occurs near the syringe wall and entrained bubbles. For a given dose of drug solution, the syringe with smaller radius and larger length will generate less liquid slosh. Reducing the air volume and syringe wall hydrophobicity are also helpful to reduce interface area and effective shear. The interface motion is reduced when the syringe axis is aligned with the gravitational direction.

## 3.2 Introduction

Autoinjectors are pen like devices designed for delivering a bolus dose, typically no more than 2 ml, of drug product solution to patients via subcutaneous injection. As a safe, convenient and cost-effective way to deliver pharmaceuticals into the human bodies, self-administered subcutaneous (SQ) injection using autoinjectors has become the gold standard in the treatment of many indications, such as anaphylaxis, multiple sclerosis, rheumatoid arthritis [50]. Most of the drug delivered by autoinjectors are proteins and amino acid derivatives, i.e. monoclonal antibodies (mAb), interferon and epinephrine [51]. A schematic of a spring-driven autoinjector is shown in Fig. 1a. The administration process of autoinjectors can be divided into three parts: activation, insertion and injection (Fig. 1b). When a spring-driven autoinjector is activated, the compressed spring is released, propelling the driving rod to hit the plunger (activation process). The syringe together with the plunger are moved by the driving rod and then stopped when the needle has extended outside the device sufficiently for the needle to penetrate the human skin and subcutaneous tissue and reach the target depth (insertion process). As the spring continues to lengthen, it pushes the plunger, injecting the drug product into the subcutaneous tissue of the patient (injection process). The insertion process can generate abrupt acceleration and deceleration of the syringe, inducing vehement motion of air-liquid interface and may impose mechanical and hydrodynamic stresses to drug molecules (Fig 1c). The protein drug molecules are susceptible to the loss of biological activities due to the perturbation of the native conformation and aggregation formation. The protein aggregates are a potential concern to product quality and patient safety, since the particles can elicit immunogenic responses [15]–[18]. It is, thus, important to understand the role of the liquid sloshing upon autoinjector activation on the mechanical and hydrodynamic stresses acting on the drug molecules, which is the focus of the current manuscript.

The formation of subvisible particles including protein aggregates and silicone oil during SQ injection and the corresponding mechanisms are still poorly understood. In the current work, we use the computational method to quantify the air-liquid interface motion and the hydrodynamic stress distributions in syringes during the insertion process of the auto-

injectors. Even though high values of shear rates occur during the sloshing motion, the time duration is relatively short (40ms). Future experiments using methods such as dynamic light scattering under similar hydrodynamic stresses, shear conditions, and time duration would help to understand whether the proteins aggregate under these conditions.

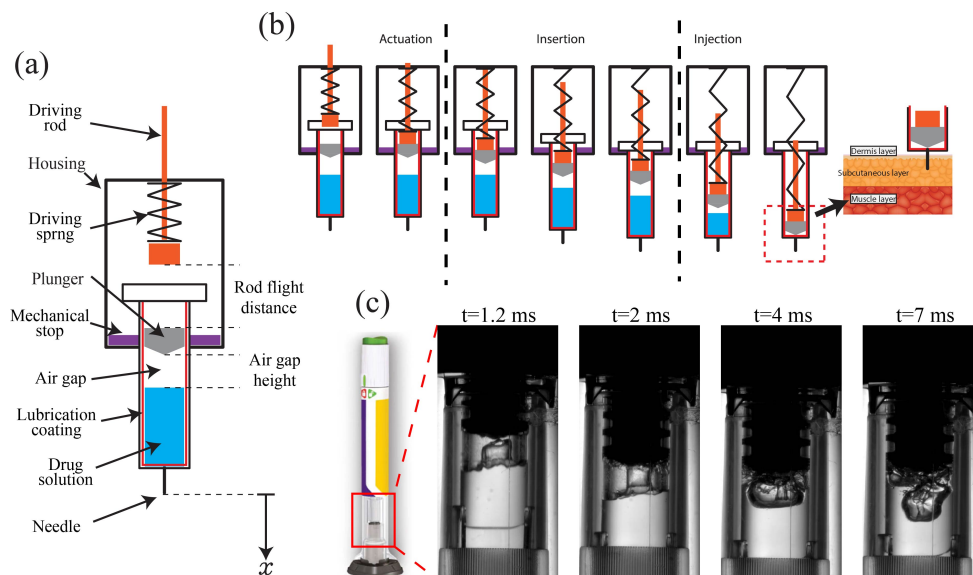


**Figure 3.1.** (a) Schematic of a spring-driven autoinjector and (b) the motion of each component during administration. (c) Experimental images of the liquid slosh during the insertion process. Here, the liquid in the syringe is water.  $t=0$  is set to the beginning of insertion process when the driving rod hits the plunger.

As an important factor concerning the quality of therapeutic proteins in manufacturing, filling, storage and delivery processes, the effects of mechanical stresses on proteins in solutions have been studied for decades. Experiments by Kiese et al. [13] demonstrate that the mechanical stress during stirring and shaking can cause aggregation of mAb molecules. The protein solutions after hours of stirring are of high turbidity, containing many insoluble, visible and sub-visible particles whilst shaking induces a higher amount of soluble particles. For shaking, the formation of aggregates depends on the air gap height. The surfactants reduce the susceptibility of the protein aggregation, suggesting that protein aggregates are formed due to the molecular interactions and exchange at the air-liquid interface.

Effects of hydrodynamic shear on protein molecules are complicated, depending on the concentration and molecular structure of proteins, the type and duration of shear applied, the strain history and so on. Many recent works have demonstrated that the air-liquid interface is the most deleterious reason for protein denaturation, while the hydrodynamic shear alone is rarely the main cause of the damage for enzymic and therapeutic proteins [5], [24], [52]. On the other hand, some argue that the protein aggregation and unfolding may occur at relatively small shear rates ( $102\sim 105\text{ s}^{-1}$ ) [53]. Protein damage can also occur due to the solid-liquid interface [24], [54], oil-liquid interface [55], extensional flow [25] and the local concentration change [26]. The dilatational compression of the air-liquid interface is shown to be more important than the constant-area shear in terms of mAb aggregation [20]. Analysis of the aggregated antibody molecules suggests that the particle formation leads to minimal structural changes but is capable of exposing free cysteines to solvent to form the nonnative intramolecular disulfate bonds, which plays a significant role in the particulate formation reaction [56].

It is challenging to experimentally measure the air-liquid interface area and hydrodynamic stress for the liquid slosh inside an autoinjector due to the confinement of syringes inside autoinjector that prevents direct measurement. Experimentally validated computational fluid dynamics (CFD) simulations are used in this paper to investigate the slosh dynamics in syringes. Numerical simulations have been validated against the published results of Rayleigh-Taylor instability (see the supplemental material). The numerical results of the interface shape are in quantitative agreement with experimental results for a simplified autoinjector platform. The interface area and hydrodynamic shear are calculated and their dependences on the syringe kinetics, properties of the drug solution (viscosity, surface tension) and syringe configuration and properties (fill volume, air gap height, tilt angle, wall wettability) are revealed.

### 3.3 Method

#### 3.3.1 Experimental Setup

The experimental setup is described in detail in [6] and only a brief summary is given here. To mimic the operating procedures of a single-spring actuated autoinjector, a simplified autoinjector platform is implemented to study the key kinematics during the insertion and injection of autoinjector device. The driving rod, spring, and syringes are mounted on a 3D-printed fixture, submerged in a transparent water tank and imaged using an ultra-high-speed camera (Phantom V 2640, Vision Research Inc). An LED light source (Flashlight 300, LaVision) accompanied by a light diffuser (DG100X100-1500, ThorLabs, Inc.) are used to achieve uniform background illumination of the pre-filled syringe. The motion of the driving rod, plunger, and syringe is captured at a rate of 20,000 frame/s. Resolution of each frame is  $15.6 \mu\text{m}/\text{pixel}$  and  $1960 \times 656$  pixels. The experiments use a 2.25 mL long glass syringe (BD Neopak) with inner diameter of 8.5 mm.

#### 3.3.2 Numerical model

The interIsoFoam, a geometric VOF Volume of Fluid (VOF) solver [57] in the OpenFOAM package, is used to simulate the motion of air and liquid inside the syringe. The OpenFOAM package has been used widely for simulating multi-phase flow problems, such as the breakup of liquid jet [58], capillary effects in porous media [59], and collapse of cavitation bubbles [60]. In the Volume of Fluid (VOF) technique, the two phases are separated by a sharp interface implicitly represented via the volume fraction  $\alpha$  of the reference phase. Here, volume fraction  $\alpha$  is a Heaviside step function with  $\alpha = 1$  representing the liquid phase and  $\alpha = 0$  representing the gas phase. As a common practice in VOF, the interface is the contour surface of  $\alpha = 0.5$  [58]–[60]. The geometric Volume of Fluid (VOF) method improves the precision for calculating the interface advection by using an explicit reconstruction of the interface from the volume fraction compared to an algebraic Volume of Fluid (VOF) method. The air and liquid are modeled as incompressible Newtonian fluids. Here, we are only interested in the flow inside the liquid and the motion of the air-liquid interface, which are subject

to the stress from the liquid. Besides, the air velocity is on the order of 1 m/s and the Mach number is less than 0.01. The role of air compressibility on the hydrodynamic stresses formed during sloshing motion is negligible. Since the frame of reference moves with the syringe, acceleration and deceleration motion of the syringe is included as an additional body force term. Rheological experiments on BSA and mAb solutions have shown that the solution has constant viscosity for shear rates larger than  $100 \text{ s}^{-1}$  [61], [62]. For surfactant-laden mAb solutions without aggregation, the viscosity is constant, but protein aggregation and adsorption on interfaces can induce shear-thinning viscosity for shear rate smaller than  $100 \text{ s}^{-1}$ . Rheological measurements suggest that the shear thinning behavior of globular protein solutions stems from the protein aggregation in the air liquid interface present in the cone and plane geometry, and the bulk viscosity measurements show a constant viscosity value independent of shear rate [63]. In our problem, protein aggregation is only a small portion of the solution and most regions have shear rates larger than  $100 \text{ s}^{-1}$ , thus, we assume the viscosity to be constant. The motion of fluid is described by the two-phase incompressible, variable-density Navier-Stokes equations. Mass conservation:

$$\nabla \cdot \mathbf{u} = 0, \quad (3.1)$$

Advection of volume fraction:

$$\frac{\partial \alpha}{\partial t} + \nabla \cdot (\alpha \mathbf{u}) = 0, \quad (3.2)$$

Momentum conservation:

$$\rho \left( \frac{\partial \mathbf{u}}{\partial t} + \nabla \cdot \mathbf{u} \mathbf{u} \right) = -\nabla p + \mu \nabla^2 \mathbf{u} + \sigma \kappa \delta_s \mathbf{n} + \rho(\mathbf{g} - \mathbf{a}), \quad (3.3)$$

Here,  $\mathbf{u}$  is a 3D vector representing the fluid velocity,  $\rho$  is the density of the mixture defined as  $\rho = \alpha \rho_l + (1 - \alpha) \rho_a$ , with  $\rho_l$ ,  $\rho_a$  being the density of liquid and air, respectively.  $\mu$  is the viscosity of the mixture defined as  $\mu = \alpha \mu_l + (1 - \alpha) \mu_a$ , with  $\mu_l$ ,  $\mu_a$  being the viscosity of the liquid and air, respectively.  $\sigma \kappa \delta_s \mathbf{n}$  is the surface tension force, where  $\sigma$  is the surface tension,  $\kappa$  is the interface curvature,  $\delta_s$  is the delta function at the interface, and  $\mathbf{n}$  is the unit normal vector of the interface. The surface tension term is calculated based on the

Continuum Surface Force model  $\kappa = -\nabla \cdot \mathbf{n}$  where the unit normal  $\mathbf{n} = \frac{\nabla \tilde{\alpha}}{|\nabla \tilde{\alpha}|}$  and  $\tilde{\alpha}$  is the smoothed volume fraction [64].  $\boldsymbol{\alpha}$  is the acceleration of syringe.

### 3.3.3 Simulation setup for slosh dynamics in syringes

The syringe is modeled as a cylinder with one end approximately represented to be smoothly connected to the needle for simplicity. The geometry of the needle entrance is shown in Fig. 2(a). To construct the mesh for the syringe, the snappyHexMesh utility in OpenFOAM was utilized, which starts with a large cuboid with a uniform mesh, removes the redundant cells and morphs the boundaries to the syringe geometry. The final mesh is shown in Fig. 2(b), where the cell size is uniform inside the domain, but the cells near the boundaries are morphed to the syringe shape. The grid size in the simulations are  $\Delta x = 1/12$  mm (102 cells in barrel diameter, 4 cells in needle diameter), the effects of grid size are discussed in the supplemental material.

In the simulation, no-slip/penetration boundary conditions are applied on all the syringe walls. The no-slip/penetration boundary condition is justified at the outlet of the needle because the needle has high resistance to the flow. During the acceleration process of the syringe, the liquid is not pressurized and there is no liquid coming out of the needle. The liquid pressure increases abruptly during the deceleration process and sustains a pressure around 6 bar when the drug solution is pushed into SQ tissues. The injection time of drug solution is  $\sim 2$  s, which can result in a flow velocity  $\sim 0.01$  m/s in the syringe. This is very small compared to the flow velocity in our simulations, thus we consider the no-slip/penetration boundary condition is valid for the needle outlet. For simplicity, the contact angle between the air-solution interface and the syringe wall, which is defined as  $\theta_c$ , is assumed to be constant. The combined effects of surface tension and gravity govern the initial shape of the interface. To get the initial interface shape, a separate simulation is conducted to get the hydrostatic interface shape. In this simulation, the final interface shape is independent of the liquid viscosity. Liquid viscosity of 1000 cp (density 1000kg/m<sup>3</sup>) is used in this simulation to suppress the motion of the interface before reaching hydrostatic state. Since the syringe acceleration is excluded here, the interface is only deformed due to the

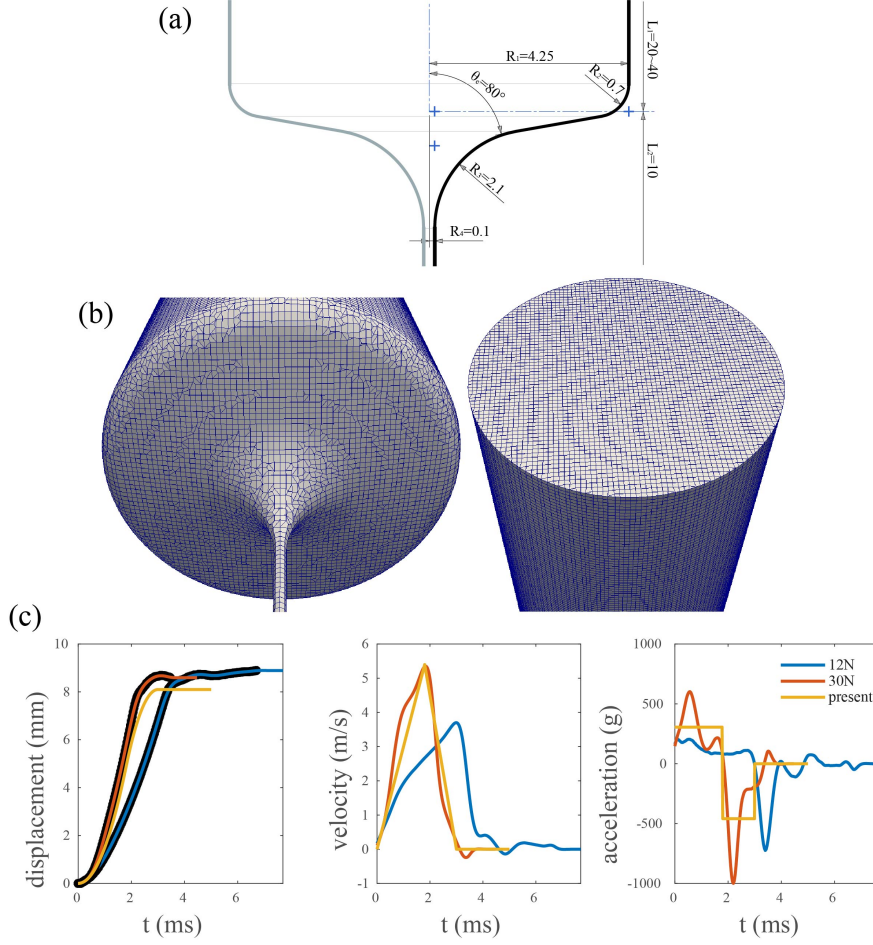


**Figure 3.2.** (a) The geometry of the needle entrance of the syringe. Dimensions are given in millimeter. The length of the syringe  $L_1$  can range from 20mm to 40mm, corresponding to the syringe volume from 1mL to 2mL. (b) The bottom (left) and top (right) view of the mesh in the simulations. (c) The displacement, velocity and acceleration of the syringe measured from experiments for two different spring strengths. The acceleration used as an input to the simulations is a simplified form of the experimentally measured kinematics caused by a 30 N spring with spring stiffness of 409 N/m.

interplay between gravity and surface tension. The magnitude of gravitational acceleration  $g$  is  $9.8 \text{ m/s}^2$ . Given that the equations are solved in the syringe frame of reference, the direction of gravitational force is determined by the tilt angle of the syringe  $\theta_t$ , where  $\theta_t$  is the angle between the axis of the syringe and the gravitational acceleration. The volume fraction data produced by this simulation is used as the initial state for the slosh dynamics simulations.

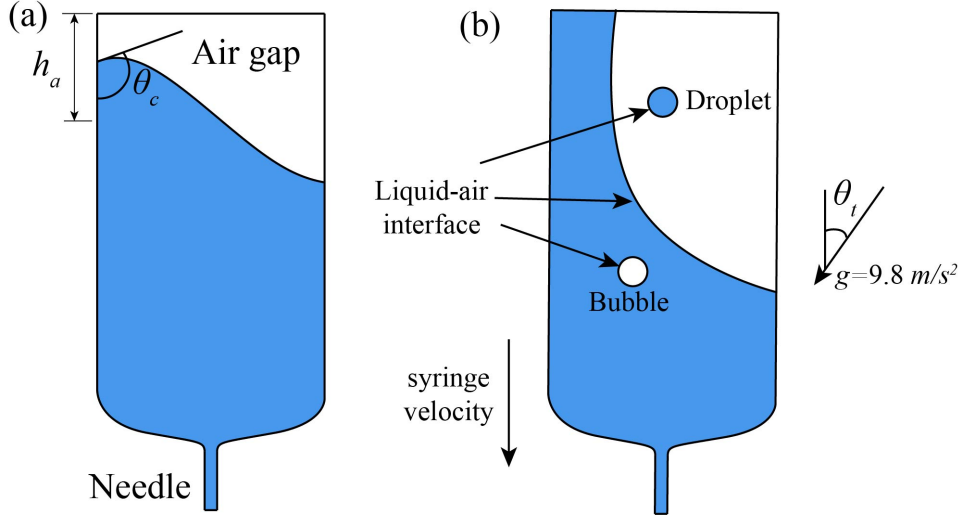


**Figure 3.3.** Schematics of (a) the initial interface setup and (b) the slosh dynamics in the syringe frame of reference for a non-zero tilt angle.

During the insertion of autoinjector, the syringe is first accelerated due to the collision of the driving rod with the plunger and then is decelerated by a mechanical stop. In numerical simulations, the syringe is assumed to go through a constant acceleration-deceleration process, where the magnitude of acceleration is described as follows.

$$a = \begin{cases} U_s/t_a, t \leq t_a \\ -U_s/t_d, t_a < t \leq t_a + t_d \\ 0, t > t_a + t_d \end{cases} \quad (3.4)$$

where  $U_s$  is the maximum syringe speed, which is usually several m/s.  $t_a$  and  $t_d$  are the acceleration and deceleration time, respectively. In the current study,  $t_a = 1.8$  ms, and  $t_d = 1.2$  ms. The resulting syringe velocity resembles that of an autoinjector driven by a 30 N spring (Fig. 2c), indicating that the kinetic energy and momentum change of the syringe are similar as that in experiments. For all the simulations, the time step is controlled by setting the max Courant-Friedrichs-Lewy (CFL) number to 0.4. For post-processing, the air-liquid interface is calculated as a contour surface where the volume fraction is  $\alpha = 0.5$ . The area of the contour surface is then integrated to find the total area of the air-liquid interface. The

Reynolds number in this problem is defined as  $Re = \rho U_s R_1 / \mu_l$ , where  $R_1 = 4.25$  mm is the inner radius of the syringe. The Reynolds number is between 400 and 10,000 in our problem.

### 3.4 Results and discussions

#### 3.4.1 Validation against Rayleigh-Taylor instability

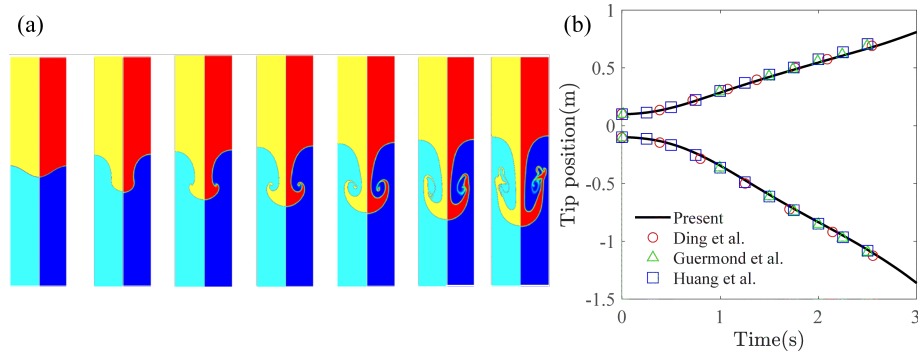


**Figure 3.4.** (a) The interface evolution due to Rayleigh-Taylor instability at time 0, 1, 1.25, 1.5, 1.75, 2, and 2.25 s. The present results (left panel, yellow and cyan) is compared with those computed using a diffusive interface method [65] (right panel, red and blue). Only half of the simulation domain is showed. (b) The center of the interface goes down while the interface near the boundary goes up. The transient behavior of the tip position agrees with the published numerical results by Ding et al. [65], Guermond and Quartapelle [66] and Tryggvason [67].

We first validated our numerical simulations with the published results for the Rayleigh-Taylor instability, where the interface is perturbed with a small amplitude of sinusoid function with the top liquid (density  $\rho_l$ ) being heavier than the bottom liquid (density  $\rho_a$ ). In the benchmark study,  $\rho_l = 3$  kg/m<sup>3</sup>,  $\rho_a = 1$  kg/m<sup>3</sup>,  $\mu_l = \mu_a = 1$  cp. The simulation domain is a 1m by 4m rectangle discretized by 200 x 800 cells. No-slip/penetration boundary condition is used for the top and bottom boundary and periodic boundary conditions for the two lateral boundaries. The gravitational acceleration here is  $g = 1$  m/s<sup>2</sup>.

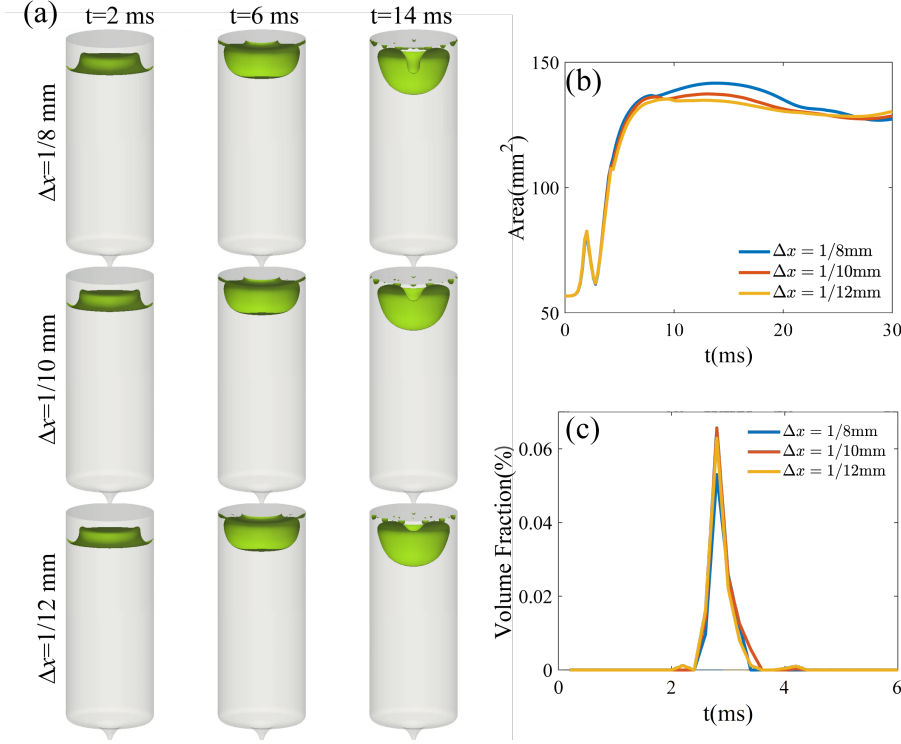


**Figure 3.5.** (a) The cross section of the liquid-air interface, (b) the total interfacial area and (c) volume fraction of liquids with strain rate  $|\mathbf{D}| > 10^4$  for three different mesh resolutions  $\delta x = 1/8, 1/10, 1/12$  mm.

### 3.4.2 Simulation results for different mesh resolutions

The interface motion in the slosh dynamics involves rupture/coalescence of droplets and bubbles, where the length scale of the flow is very small and difficult to be captured by simulations. The interface is also highly unstable, since a small perturbation of the interface can grow abruptly in the later stage and have an important influence in the final interface shape. To assure the reliability of our numerical results, we investigated the interface shape for three different mesh resolutions (Fig. 3.5). As the mesh refines, the simulation produces similar interface shape, while the details of bubble rupture and coalescence varies for different mesh resolutions. In Fig. 3.5(b), the area interface for different mesh resolution follows similar trend. The volume fraction of liquids whose strain rate is larger than  $10^4 \text{ s}^{-1}$  is shown in Fig. 3.5(c). As the mesh refines, the rupture/coalescence of bubble and droplets are better resolved by the simulations, where the fluids are usually subject to high strain

rate. Therefore, the volume fraction for  $|\mathbf{D}| > 10^4 \text{ s}^{-1}$  slightly increases with decreasing grid size.

### 3.4.3 Comparison with experiments

The simulations are first validated against experimental results. In experiments, the initial spring force of the compressed drive spring is 12 N. The ensemble-averaged displacement for the syringe (Fig. 4) is obtained by using the cross-correlation method. Then, the velocity and acceleration are calculated from the 1st and 2nd derivatives of the spline fit of the displacement. The acceleration profile is then used as the input in the numerical simulation. The interface profile is also extracted from the experimental snapshots using an in-house edge detection algorithm. The ensemble-averaged interface area is calculated based on the extracted interface profile, which is compared with the simulation results (Fig. 5). In the experiments, the initial air gap height is 8mm but because of the air gap compression due to plunger motion inside the syringe, the air gap height changes at the start of the impact (Fig. 5b). The air-liquid interface comes into contact with the plunger after 4 ms when the air gap height reaches the steady state. The steady-state air gap height of 4 mm is used in simulations. The contact angle between the air-liquid interface and syringe wall is 10 degrees for both simulations and experiments. The initial interface in the simulation is obtained from a separate simulation where the free interface reaches the equilibrium state due to the influence of gravity and surface tension effects. In both experiments and simulations, the syringe inner diameter is 8.5 mm, liquid column height is 32mm. Silicone oils (Sigma-Aldrich) with four different kinematic viscosities (1, 5, 20, 50 cSt and density 822, 913, 950, 960 kg/m<sup>3</sup>, which correspond to viscosities 0.822, 4.565, 19 and 48 cp) are used to mimic drug product solutions of different concentrations. The experiments are repeated 6 times for each viscosity, where the camera recorded 50ms of the syringe motion after the activation. Other details of simulation setup are discussed in the section Method - Numerical Model.

The interface area calculated from numerical simulations shows a good agreement with that measured from experiments for different liquid viscosities (Fig. 5c). The interface area

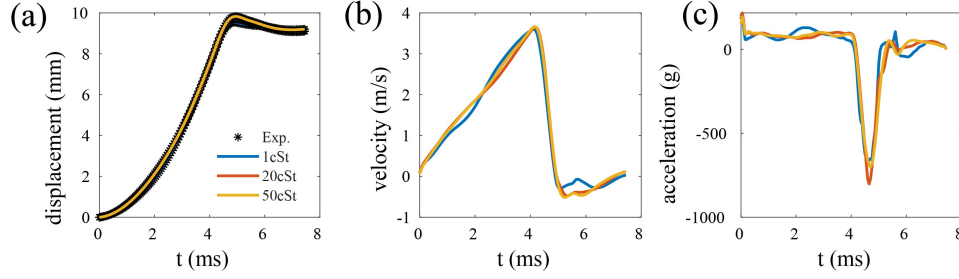


**Figure 3.6.** The kinematics (a)displacement, (b)velocity and (c)acceleration of the syringe measured in experiments for different fluid viscosities (a) 4.565 cp, (b) 19 cp and (c) 48 cp.

increases when the liquid viscosity decreases. The snapshots for critical frames are shown in Fig. 6. The interface shape predicted in the simulation agrees relatively well with the experimental results. In both numerical and experimental results, the interface near the wall rises when the syringe accelerates. The liquid comes into contact with the plunger and the air volume forms a large bubble. Then the syringe decelerates and a round liquid column forms at the center of the syringe. In the experiments, the air-liquid interface is rougher than that in the simulation. This is possibly because the simulations neglect fluid compressibility, which can cause Richtmyer–Meshkov instability at the interface. On the other hand, due to the limitation of the grid resolution, some small bubbles and droplets that are observed in experiments are not fully resolved by the simulations. Due to numerical diffusion, some fine features of the interface are not captured in simulations. Additionally, the syringe in the experiments can be subject to slight horizontal motion, which breaks the axial symmetry of the interface dynamics. In the experiments, the interface area for the first 5 ms is quantified, because the small droplets and bubbles formed in later stages cannot be captured by the current edge detection method.

#### 3.4.4 Investigation of interface area and strain rate

Experiments on the interfacial rheology has indicated that protein aggregation can occur at the interface [20]. Therefore, the time evolution of the interfacial area is investigated for different liquid viscosity  $\mu_l$  (Fig. 3.9), air gap height  $h_a$  (Fig. 3.10), maximum syringe

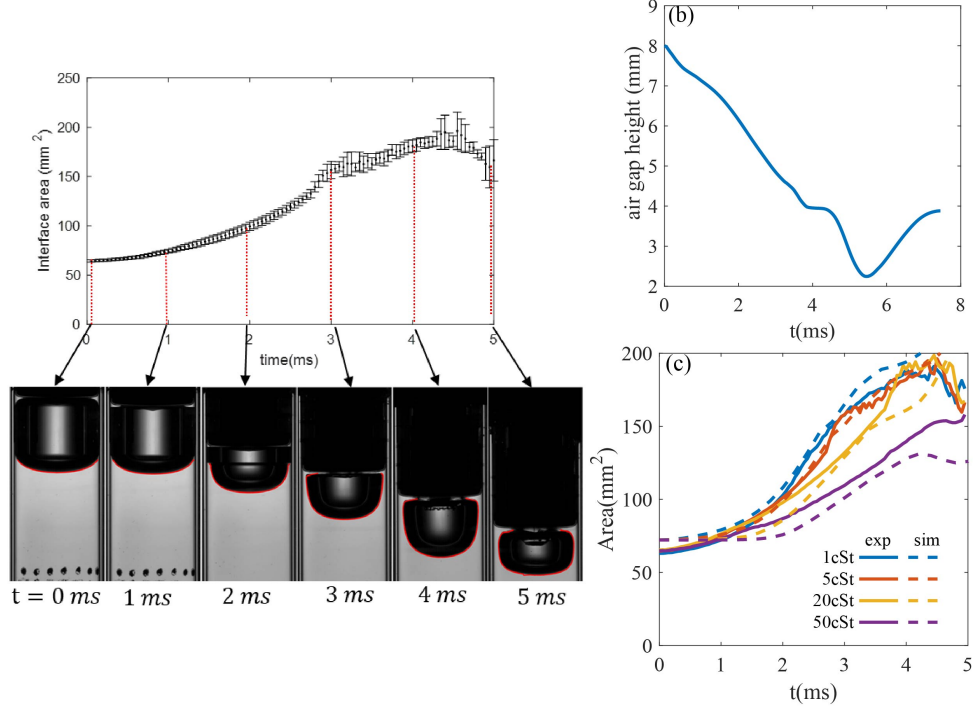


**Figure 3.7.** The ensemble-averaged interface area calculated using the edge detection method for 4.565 cp. Error bar indicates the standard deviation. Snapshot for one run is shown in the bottom panel. (b) Air gap height in the experiments. (c) The interfacial area in the simulation shows a good agreement with experimental results.

velocity  $U_s$  (Fig. 3.11), tilt angle of the syringe  $\theta_t$  (Fig. 3.12), contact angle between wall and the interface  $\theta_c$  (Fig. 3.13), surface tension  $\sigma$  (Fig. 3.14), and liquid fill volume  $V_f$  (Fig. 3.15). To investigate the effect of each parameter, the other parameters are set to be the same as the baseline simulation, whose parameters are listed in Table 1. Here, tilt angle  $\theta_t$  is defined as the angle formed between the axis of the syringe and the gravitational direction. The contact angle is set to  $\theta_c = 100^\circ$ , because in most of prefilled autoinjectors, the syringe wall is coated with a thin layer of silicone oil, making the syringe wall non-wetting to the drug solutions [68], [69].

Given the fluid velocity  $\mathbf{v}$ , the rate-of-strain tensor in the liquid phase  $\mathbf{D} = \nabla \mathbf{v} + \nabla \mathbf{v}^T$  is calculated. The magnitude of rate-of-strain tensor  $|\mathbf{D}| = \sqrt{\sum_i \sum_j D_{ij}^2} / 2$  quantifies the rate of deformation of fluid particles. In the current work, the strain rate threshold of  $D_0 = 104 \text{ s}^{-1}$  for denaturation of drug protein is used to quantify the volume fraction of the liquid at

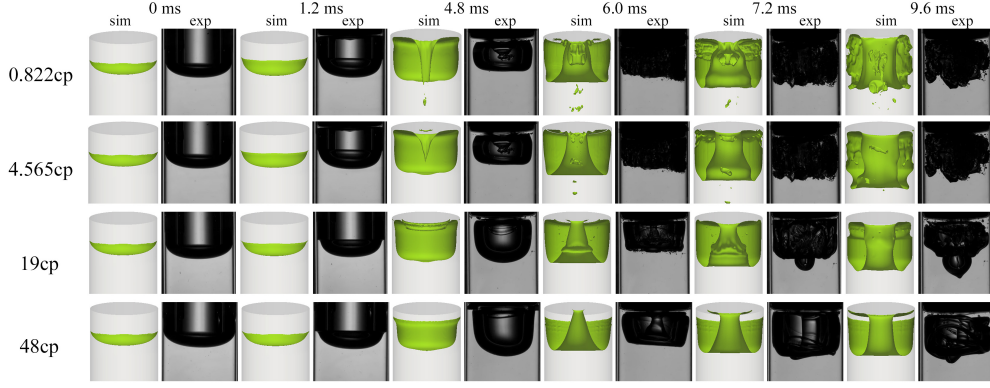


**Figure 3.8.** The interface shape in simulations (labeled by “sim”) and experiments (labeled by “exp”) for different liquid viscosities.

which  $|D| > D_0 \text{ s}^{-1}$  in the syringe. We report the results for a specific syringe configuration, however, the results are independent of the exact syringe geometry. Additionally, non-dimensionalization can be used to generalize the results to a broader parameter space. The definition and value of the dimensionless numbers for the baseline simulation can be found in Table 3.1.

**Table 3.1.** Parameters for the baseline simulation

Liquid viscosity $\mu_l$	1 cp
Tilt angle $\theta_t$	$0^\circ$
Fluid density $\rho_l$	$1000 \text{ kg/m}^3$
Air gap height $h_a$	2 mm
Surface tension $\sigma$	40 dyn/cm
Max. Syringe velocity $U_s$	5.4 m/s
Air viscosity $\mu_a$	0.012 cp
Fill volume $V_f$	1 mL
Air density $\rho_a$	$1 \text{ kg/m}^3$
Contact angle $\theta_c$	$100^\circ$
Liquid column height	18 mm
Syringe inner diameter $2R_l$	8.5 mm
Reynolds number $\text{Re} = \rho U_s R_l / \mu_l$	22,950
Weber number $\text{We} = \rho U_s^2 R_l / \sigma$	3098
Ohnesorge number $\text{Oh} = \sqrt{\text{We}} / \text{Re}$	0.0024
Bond number $\text{Bo} = \rho g R_l^2 / \sigma$	4.4

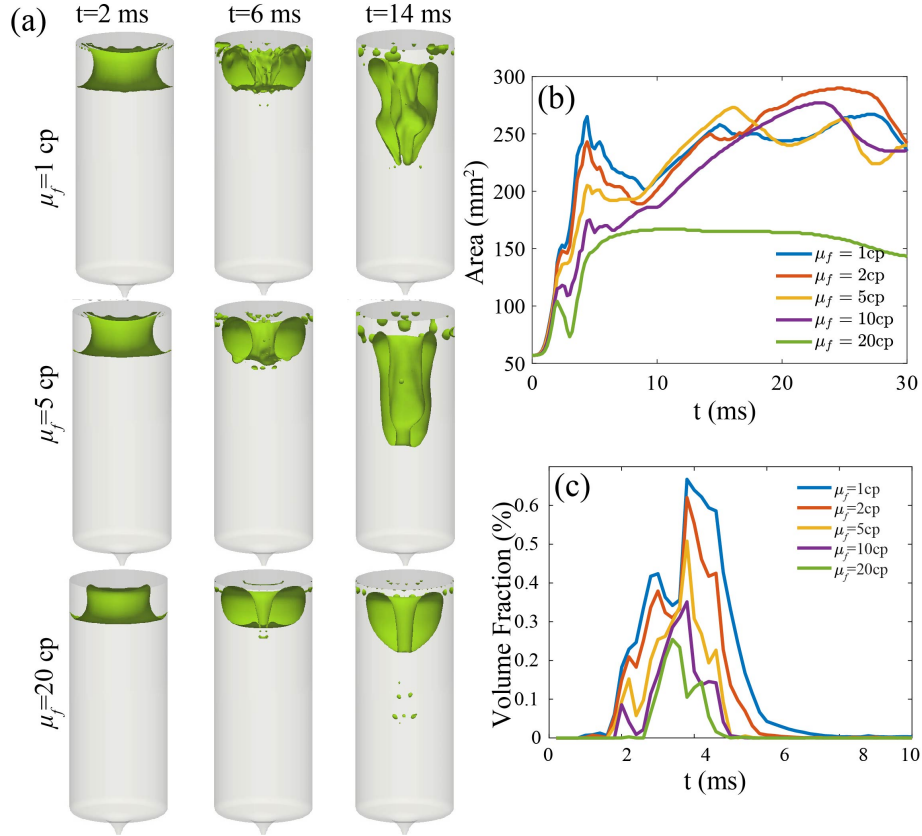


**Figure 3.9.** (a) The cross section of the air-liquid interface, (b) the total interfacial area and (c) volume fraction of liquids with strain rate  $|\mathbf{D}| > D_0$  for different liquid viscosities  $\mu_l$ .

The slosh dynamics for liquid viscosity of 1 cp in Fig. 7a shows a qualitative agreement with the experimental observations in Fig. 1b. The motion of the air-liquid interface for zero tilt angle and non-wettable syringe wall can be characterized by the following process: the air-liquid interface starts with a convex meniscus where the interface at the center is higher than the interface near the wall. When the syringe is accelerated, the center of the interface gains a vertical speed and rises relative to the syringe wall ( $t=2$  ms). Then the syringe decelerates and the interface near the wall rises along the syringe wall, reaches the plunger and focuses at the center. The air entrainment deforms into a toroidal shape ( $t=6$  ms), leading to a large strain rate. Then, the air-liquid interface deforms and may rupture into smaller bubbles ( $t=14$  ms). After the liquid slosh, small air bubbles may reside on the syringe wall due to the wall hydrophobicity.

When the liquid viscosity increases, there is less droplet and bubble formation during the slosh process (Fig. 3.9). Therefore, the interfacial area for  $t < 10$  ms decreases with the solution viscosity. For viscosity less than 10 cp, the final interface shape is similar and is an elongated toroid. The interface area only decreases when liquid viscosity exceeds 10 cp. As the fluid becomes more viscous, irregular flows that break the axial symmetry are suppressed by viscous dissipation and the interface motion becomes more axisymmetric. When the liquid viscosity increases, more kinematic energy is dissipated so that fluid is also subject to smaller strain rate. The volume fraction of fluids with  $|\mathbf{D}| > D_0$  decreases with the liquid viscosity. Some drug solutions exhibit shear-thinning viscosity. In other words, the viscosity of the solution decreases with the local shear rate. Therefore, the interface area and strain rate are expected to be larger than the results at the zero-shear viscosity for those shear-thinning drug solutions.

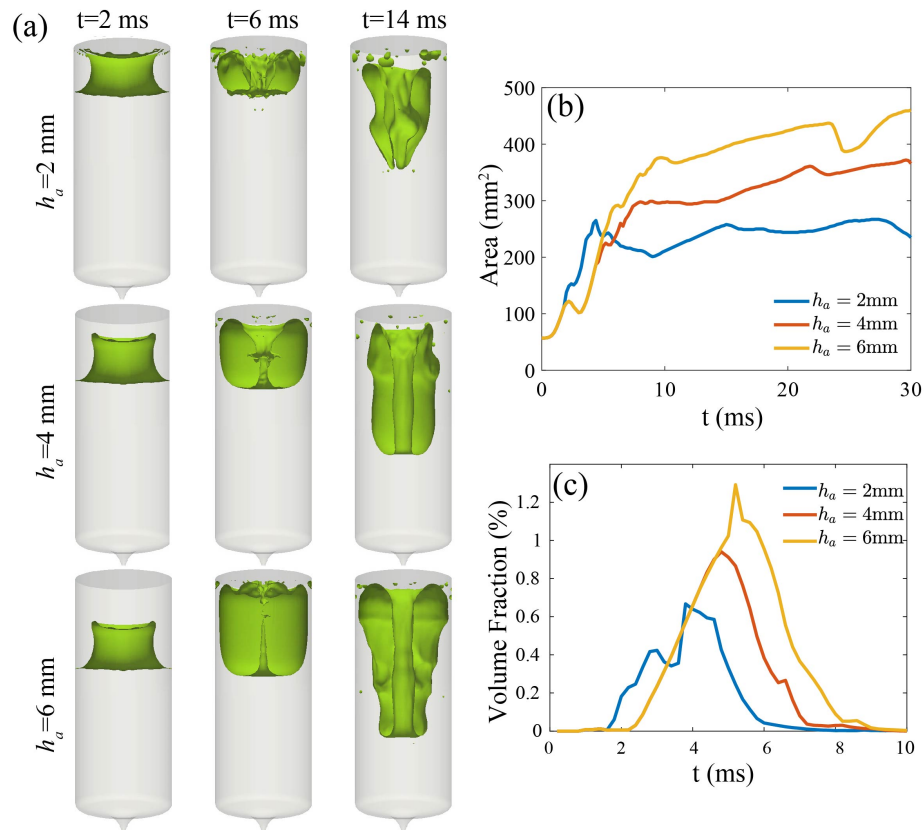


**Figure 3.10.** (a) The cross section of the interface, (b) the total interfacial area and (c) volume fraction of liquids with strain rate  $|\mathbf{D}| > D_0$  for three different air gap heights  $h_a = 2, 4, 6$  mm.

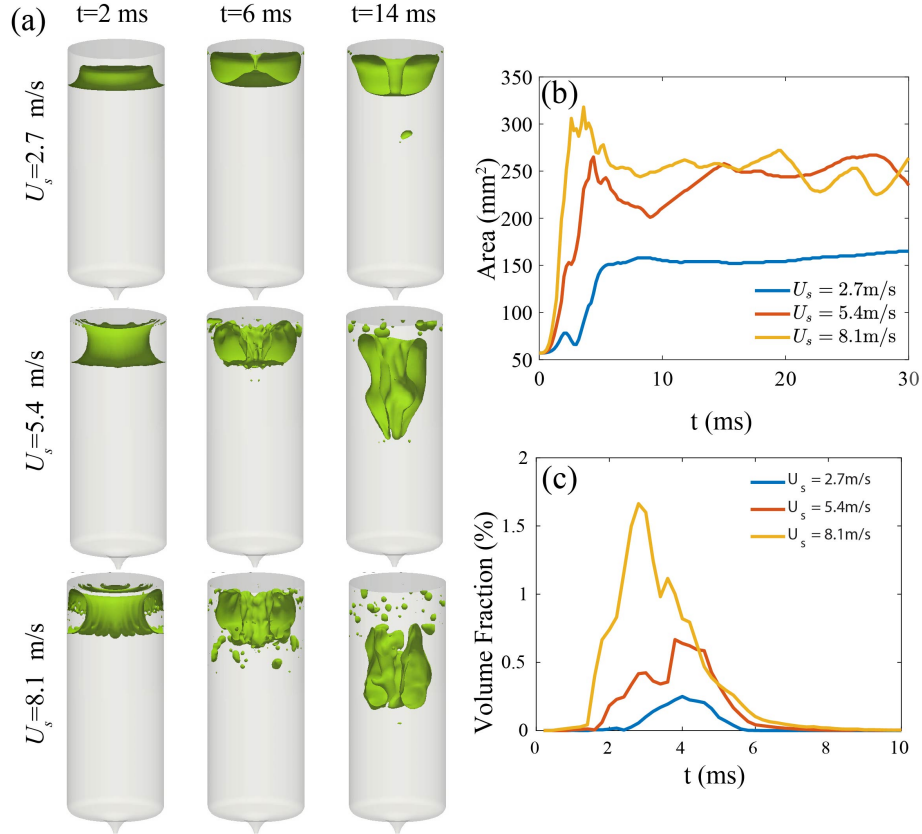


**Figure 3.11.** (a) The cross section of the interface, (b) the total interfacial area and (c) volume fraction for liquids with strain rate  $|\mathbf{D}| > D_0$  for three different maximum syringe velocities  $U_s = 2.7, 5.4, 8.1$  m/s.

When the air gap height increases, more air volume will be trapped inside the liquid (Fig. 3.10). The toroidal interface is elongated, resulting in an increase of the interfacial area for  $t > 5$  ms. More fluids are also subject to high strain rates. When the maximum syringe velocity increases, the fluids gain more kinetic energy during the slosh motion (Fig. 3.11), enhancing bubble and droplet formation. The interfacial area increases with syringe velocity for  $t < 10$  ms. For  $t > 10$  ms, the interface shape and interfacial area are hardly changed when syringe velocity is larger than 5.4 m/s. However, for the syringe velocity of 2.7 m/s, the interface is symmetric and has a smaller area. The strain rate experienced by the fluid also increases abruptly when increasing syringe velocity.

The motion of the air-liquid interface is modified when the syringe is tilted (Fig. 3.12). The interface area increases for  $t < 15$  ms for increasing tilt angle, suggesting that the tilt

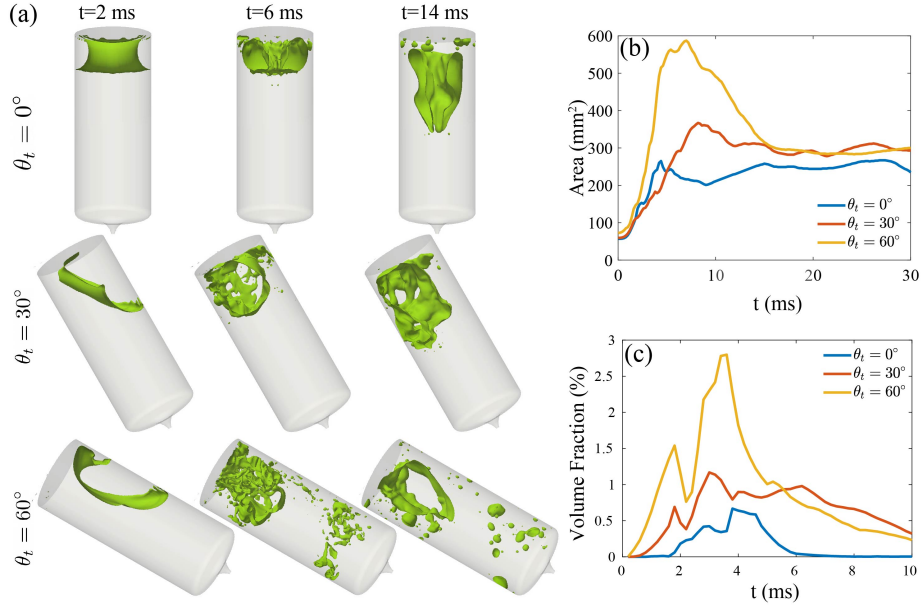


**Figure 3.12.** (a) The cross section of the interface, (b) the total interfacial area and (c) volume fraction for liquids with strain rate  $|\mathbf{D}| > D_0$  for three different tilt angles  $\theta_t = 0^\circ, 30^\circ, 60^\circ$ . Here, the air gap height is 4 mm, while the other parameters are the same as Table 3.1

angle can enhance the bubble and droplet formation during slosh. Since the air volume entrapped in the liquid is the same, the interfacial area is similar for  $t > 15$  ms. The volume fraction of liquid subject to high strain rate increases abruptly with tilt angle. The strain rate also lasts for larger time durations.

The slosh dynamics is dependent on the wettability of the syringe wall. Here,  $\theta_c$  smaller than  $90^\circ$  means the wall is wettable and hydrophilic while  $\theta_c$  larger than  $90^\circ$  means the wall is non-wettable and hydrophobic. Compared to the baseline simulation, the interface motion is different for hydrophilic syringe walls  $\theta_c = 80^\circ$  (Fig 11). The interface near the wall rises along the syringe wall during the syringe acceleration because of interfacial instability caused by the Rayleigh Taylor instability. On the other hand, syringe deceleration causes the center of the interface to move upwards, leading the interface to become flatter due to its stabilizing effect. The final air entrainment is trapped near the plunger, and there are fewer small bubbles forming in the solution. The resulting interfacial area is smaller than that for  $\theta_c = 100^\circ$ , however, there is no obvious decrease in the strain rate experienced by the liquid.

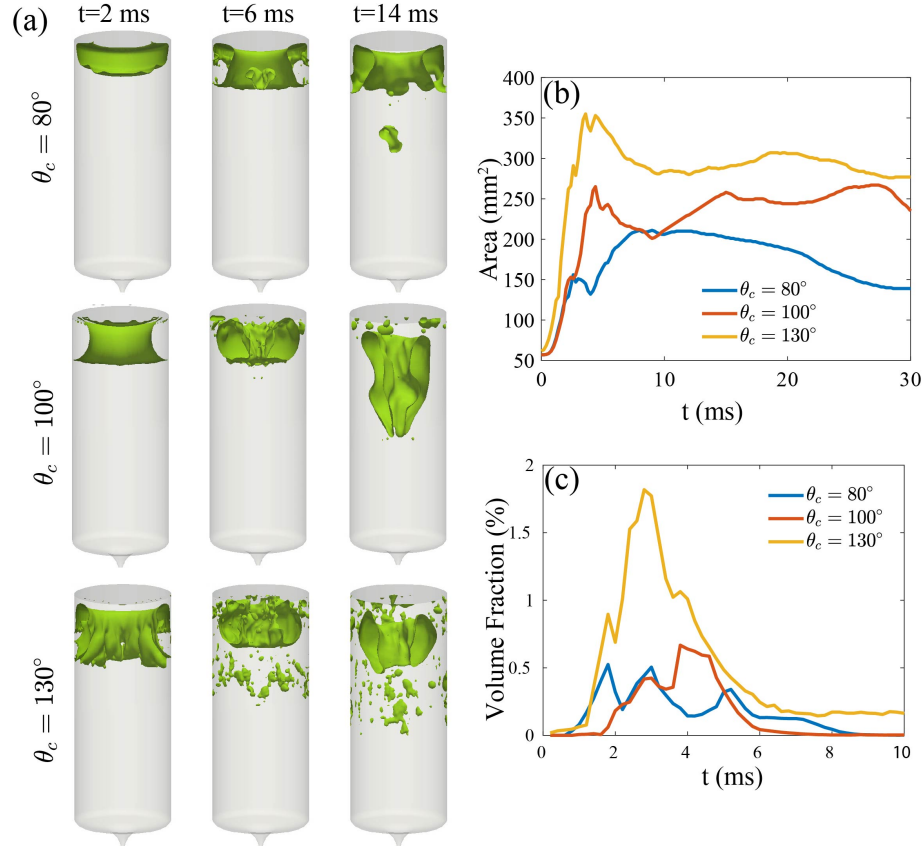


**Figure 3.13.** The cross section of the interface, (b) the total interfacial area and (c) volume fraction for liquids with strain rate  $|\mathbf{D}| > D_0$  for three different contact angles between the air-liquid interface and the syringe wall  $\theta_c = 80^\circ$ ,  $100^\circ$ ,  $130^\circ$ .

For hydrophobic syringe walls, when  $\theta_c$  increased from  $100^\circ$  to  $130^\circ$ , the liquid gains more kinematic energy due to the larger curvature of the initial interface. As contact angle increases, more bubbles are seen attached to the wall. More air bubbles that are attached to the wall are generated by the liquid slosh due to the increasing hydrophobicity of the syringe wall. The interfacial area increases, and more liquids are subject to high strain rates.

Surface tension (Fig. 3.14) and the fill volume of the liquid (Fig. 3.15) have small effects on motion of the air-liquid interface. The surface tension of a drug product solution often containing a surfactant is usually in a narrow range between 40 and 60 dyn/cm [70]. When the surface tension increases, the motion of the interface is hardly changed for  $t < 10$  ms, where the interfacial area and the volume fraction of liquid subject to high strain rates are almost

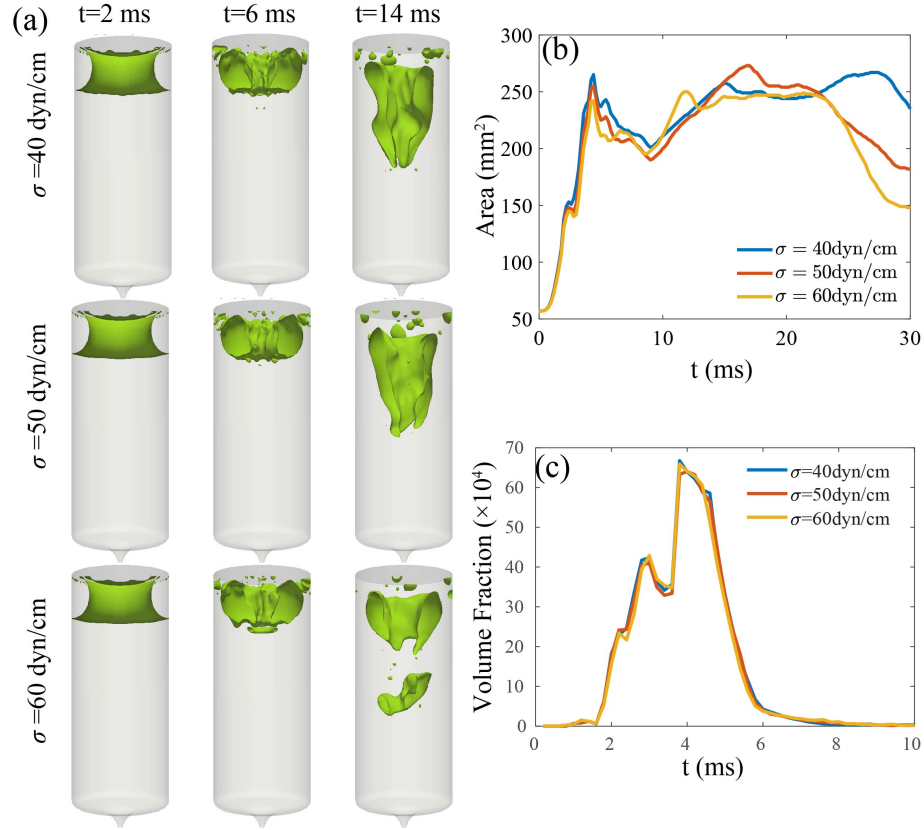


**Figure 3.14.** (a) The cross section of the interface, (b) the total interfacial area and (c) volume fraction for liquids with strain rate  $|\mathbf{D}| > D_0$  for surface tensions  $\sigma = 40, 50, 60$  dyn/cm.

independent of the surface tension. Larger surface tensions cause the interface to rupture after 25 ms and the interfacial area decreases accordingly. Protein and surfactant molecules may not have enough time to reach equilibrium adsorption at the air-liquid interface due to the short time scale of the sloshing dynamics. This can lead to formation of Marangoni stresses and non-uniform surface tension on the interface, which we neglect in this work. However, our results show that the results are insensitive to the surface tension values. Thus, we expect the results for interface dynamics in the absence of equilibrium adsorption to be very similar to what we have reported. In simulations, fill volumes of 1, 1.5, and 2mL correspond to liquid column heights of 18, 27, and 36mm, which are much larger than the air gap height (around 2~6 mm). Since the slosh dynamics only occurs at the top of the liquid column and is not affected by the bottom wall, the motion of interface is almost

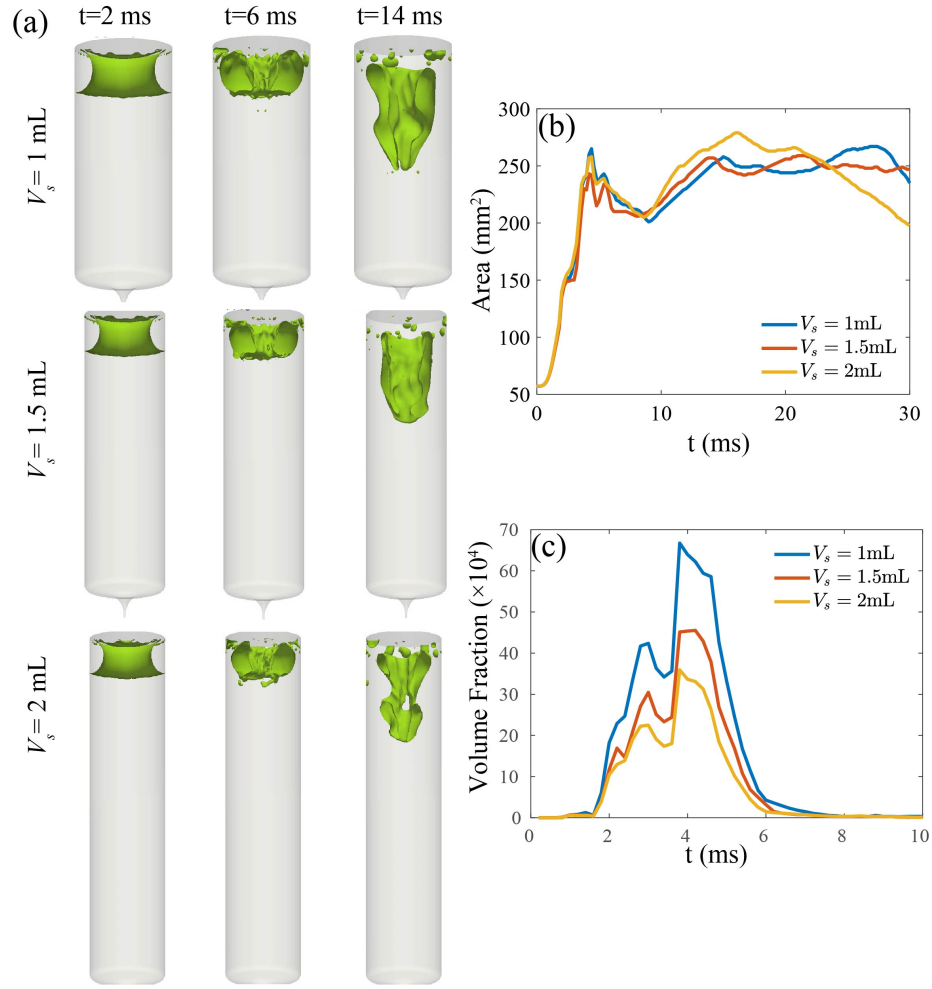


**Figure 3.15.** (a) The cross section of the interface, (b) the total interfacial area and (c) volume fraction for liquids with strain rate  $|\mathbf{D}| > D_0$  for three fill volumes  $V_f = 1, 1.5, 2 \text{ mL}$ .

independent of the fill volume. The interfacial area is not changed. The same amount of liquid is subject to high strain rates, therefore, the volume fraction decreases with the fill volume. Besides, the interface motion occurs mainly at the top of the syringe, and the liquid slosh is independent of the geometry of the syringe bottom.

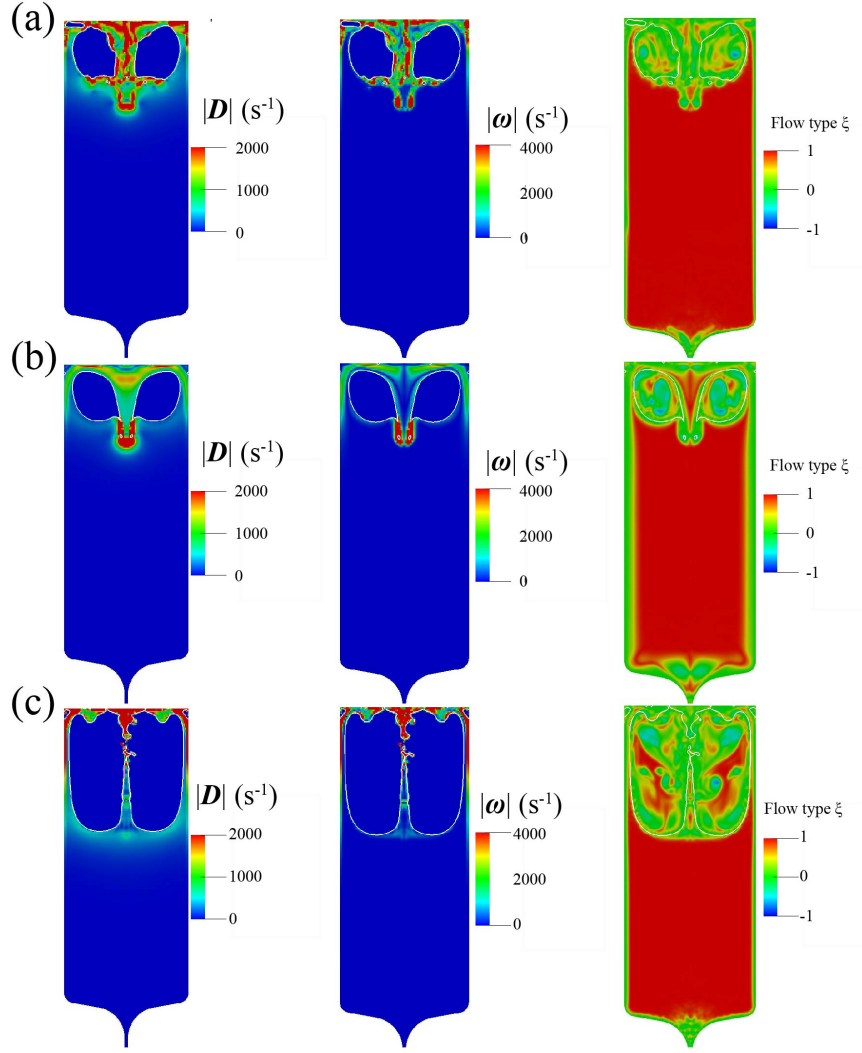


**Figure 3.16.** The spatial distribution of strain rate (left), vorticity (middle) and flow type (right) on the cross section at  $t = 6$  ms for (a) baseline, (b) high viscosity  $\mu_f = 20$  cp, (c) large volume gap  $h_a = 6$  mm, (d) large tilt angle  $\theta_t = 60^\circ$  and (e) large contact angle  $\theta_c = 130^\circ$ . The air-liquid interface is indicated by the white line.

### 3.4.5 Distribution of the strain rate and the flow type

To better understand where the drug molecules are most susceptible to hydrodynamic stress, the strain rate, vorticity and flow type field are calculated (Fig. 14). Here, flow type is defined as

$$\xi = \frac{|D| - |\Omega|}{|D| + |\Omega|}, \quad (3.5)$$

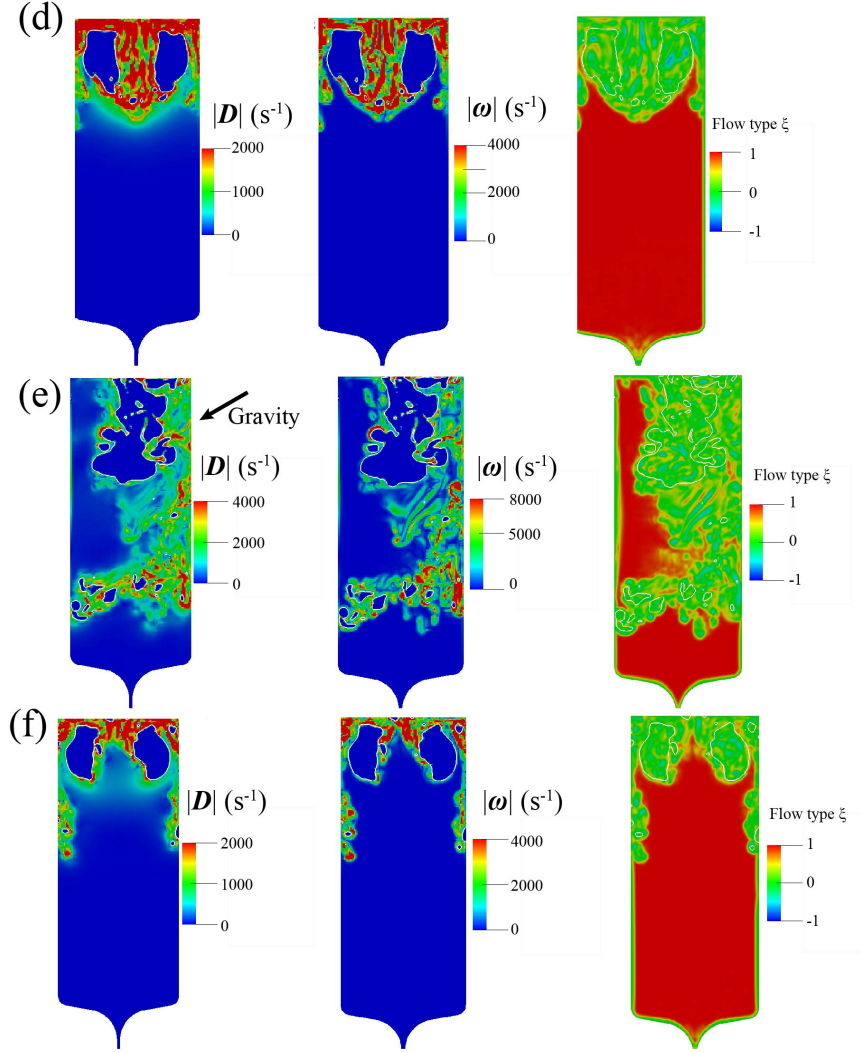


**Figure 3.17.** Fig. 15. Continuation of Fig. 14.

where  $\xi$  varies from  $-1$  to  $1$ .  $\xi = 1$  corresponds to pure extensional flow,  $\xi = 0$  corresponds to pure shear flow and  $\xi = -1$  is solid-like rotation flow [71]. From the study by Dobson et al. [25], the pure extensional flow is more likely to cause damage to the protein molecules than the pure shear flow. Thus, flow regions with high strain rate and  $\xi = 1$  could be more detrimental to protein molecules. For the baseline simulation (Fig. 3.16a), large strain rate and vorticity values are observed near the plunger and the centerline of the toroid. Both regimes are dominated by the shear flows ( $\xi = 0$ ). When the liquid viscosity increases (Fig. 14b), the strain rate and vorticity near the plunger and the centerline of the toroid decreases. The flow in the centerline of the toroid is dominated by an extensional flow ( $\xi = 1$ ). Despite

the fact that higher solution viscosity induces lower strain rates, the transition from shear flow to extensional flow may induce more protein denaturation. For larger air gaps (Fig. 3.16c), the fluid near the top and side walls are subject to strong shear flows. When the syringe velocity increases (Fig. 3.17d), the spatial distribution of strain rate and vorticity are similar to the baseline simulation. Increasing the tile angle has significant effects on the spatial distribution of strain rate and vorticity (Fig. 3.17e), where many bubbles are formed at the bottom of the syringe and strong shear flows are present near the bubbles. Here, large regions of the liquid are subject to a strong shear flow. For larger contact angles (Fig. 3.17f), more bubbles are attached to the walls, around which the fluids are experiencing a strong shear flow. In general, most regions under high strain rates show flow type  $\xi$  close to zero, suggesting that the hydrodynamic shear is more important than the hydrodynamic extension. Strong shear flows are usually present near the syringe wall and near the moving bubbles in the bulk fluid or attached on the wall. For solution with higher viscosity, the shear flow is more suppressed than the extensional flow, and the extensional flow becomes more important. The drug molecules may be subject to the same amount of damage due to the presence of extensional flow.

### 3.4.6 Analysis of invariants of the rate-of-strain and rate-of-rotation tensors

Given the fluid velocity  $\mathbf{v}$ , the rate-of-strain tensor  $\mathbf{D} = \nabla\mathbf{v} + \nabla\mathbf{v}^T$  and rate-of-rotation tensor  $\mathbf{\Omega} = \nabla\mathbf{v} - \nabla\mathbf{v}^T$  are also calculated, where  $\nabla\mathbf{v}$  is the gradient of the velocity vector. The magnitude of rate-of-strain tensor  $|\mathbf{D}| = \sqrt{\sum_i \sum_j D_{ij}^2}/2$  evaluates the rate of deformation of fluid particles. The magnitude of rate-of-rotation tensor  $|\mathbf{\Omega}| = \sqrt{\sum_i \sum_j \Omega_{ij}^2}/2$  evaluates the rate of rotation of fluid particles. The fluid vorticity, which is defined as  $\omega = \nabla \times v$ , can be related with rate-of-rotation tensor as  $|\omega| = 2|\mathbf{\Omega}|$ . In the current work, the strain rate threshold of  $D_0 = 10^4 \text{ s}^{-1}$  for denaturation of drug protein is used to quantify the volume fraction of the liquid at which  $|\mathbf{D}| > D_0 \text{ s}^{-1}$  in the syringe. The drug molecules are only present in the liquid phase, where volume fraction  $\alpha$  is 1. Thus, the final results of  $\mathbf{D}$  and  $\mathbf{\Omega}$  have been multiplied by the volume fraction  $\alpha$  before calculating the volume fraction for which the strain rate exceed the above mentioned threshold. The invariants of the rate-

of-strain and rate-of-rotation tensors can imply the geometry and topology of the flow in complicated flows [72], [73]. Here, three invariants are considered: the second invariants of rate-of-strain tensor  $Q_s = -|\mathbf{D}|^2$ , which is proportional to the local viscous dissipation of kinematic energy; the second invariants of rate-of-rotation tensor  $Q_w = |\boldsymbol{\omega}|^2$ , which is proportional to the local enstrophy (kinetic energy due to turbulence) density; the third invariant of rate-of-strain tensor  $R_s = \sum_i \sum_j \sum_k D_{ij} D_{jk} D_{ki} / 3$ , where  $R_s > 0$  implies that the fluid particles are expanding and the associated flow is in a sheet-like structure, while  $R_s < 0$  implies a contraction flow and a tube-like flow structure.

During protein aggregation, the protein molecules can be partially unfolded by the stretching force applied on the protein molecules. Larger  $Q_s$  indicates that more energy is adsorbed by the protein molecules, which may be detrimental to drug molecules. Larger  $Q_w$  indicates that the strain rate in the fluids contribute to the rotation rather than the deformation of the drug molecules, which alleviate the damage to protein molecules.  $R_s < 0$  means contraction flow where the molecules are stretched in one dimension, which is more detrimental than  $R_s > 0$ , where the expansion flow causes molecules to be stretched in two directions. To sum up, the most detrimental flow is large  $Q_s$ , zero  $Q_w$ , and negative  $R_s$ , which correspond to the pure extensional flow.

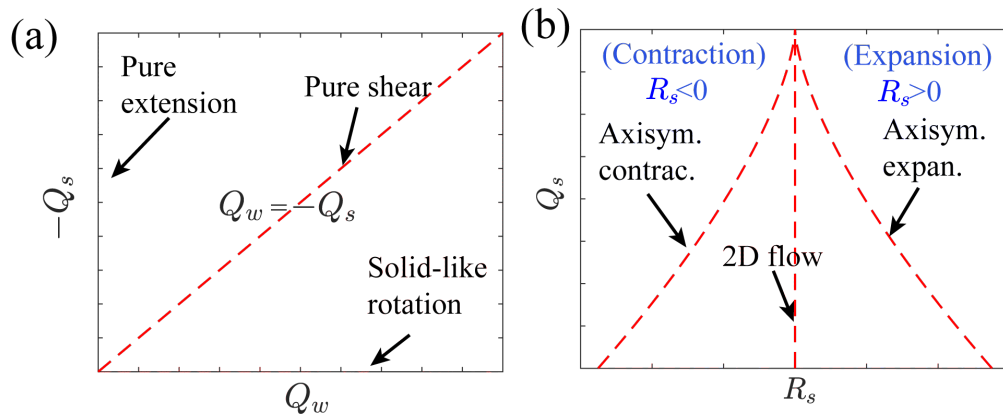


**Figure 3.18.** (a)  $(Q_w, -Q_s)$  and (b)  $(R_s, Q_s)$  map with the physical meanings for each zone. Pure extensional flow with large  $Q_s$ , zero  $Q_w$ , and negative  $R_s$  is considered most possible to unfold protein molecules.

A common way to investigate the invariants above is to plot the joint PDFs on maps of  $(Q_w, -Q_s)$  and  $(R_s, Q_s)$ . In the map of  $(Q_w, -Q_s)$  (Fig. 3.18(a)), x-axis represents solid-like rotation motion with high enstrophy and zero viscous dissipation. On the other hand, y-axis represents pure extensional flow with a high viscous dissipation and zero enstrophy. The line of  $Q_w = -Q_s$  represents a vortex sheet or a pure shear flow. In the map of  $(R_s, Q_s)$  (Fig. 3.18(b)), the left dashed red line represents the axisymmetric contraction flow. The red dashed line represents the axisymmetric expansion flow. The middle red dashed line represents 2D flows.

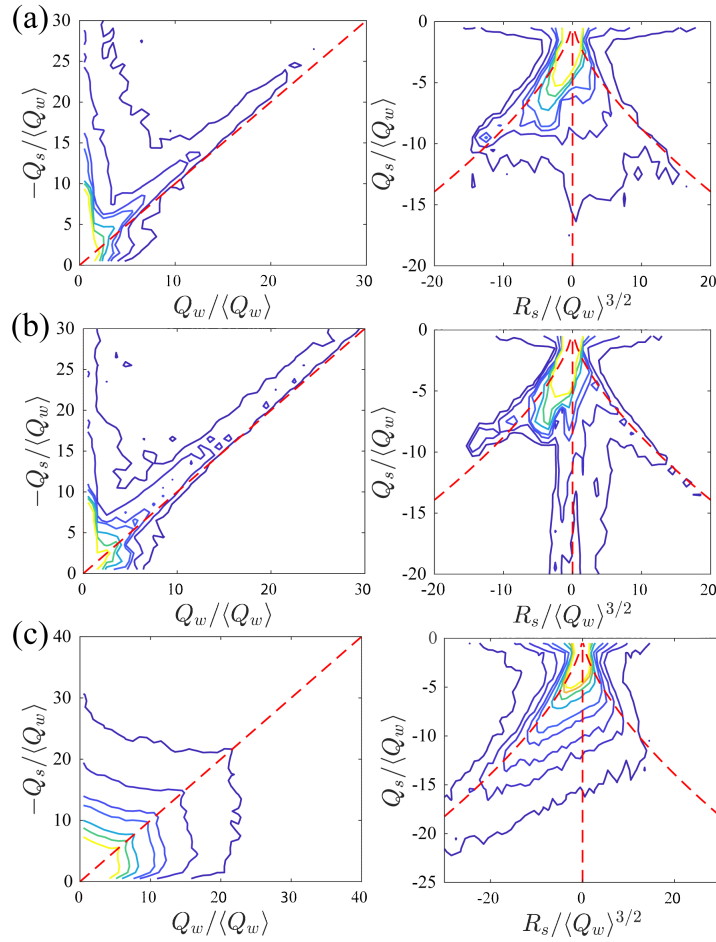


**Figure 3.19.** Joint PDFs on maps of  $(Q_w, -Q_s)$  and  $(R_s, Q_s)$  at  $t = 4$  ms for (a) baseline simulation, (b) higher viscosity  $\mu = 5$  cp, and (c) large tilt angle  $\theta_t = 60^\circ$ . The contour levels from blue to yellow are  $2 \times 10^{-5}$ ,  $6 \times 10^{-5}$ ,  $1.4 \times 10^{-4}$ ,  $2 \times 10^{-4}$ ,  $4 \times 10^{-4}$ ,  $6 \times 10^{-4}$ ,  $10^{-3}$ .  $\langle Q_w \rangle$  is the average  $Q_w$  for all the fluids, and is  $3.43 \times 10^5$ ,  $2.73 \times 10^5$ ,  $7.72 \times 10^5$   $\text{s}^{-2}$  for plot (a) (b) and (c), respectively.

For the baseline simulation (Fig. 3.19a), the joint PDF on  $(Q_w, -Q_s)$  map suggests that the dominant flow patterns in the liquid slosh are extensional flow and a flow close to pure shear flow. On the other hand, in the joint PDF on  $(R_s, Q_s)$  map, the axisymmetric contraction and 2D flows are dominant. During the slosh dynamics, pure shear 2D flow can be generated near the syringe wall and moving bubbles. Extensional flow, axisymmetric contraction flows can be generated during the rupture of the air-liquid interface. The other types of strain rate are less prevalent in the fluid and high strain rates only occurs near the wall and bubbles.

When liquid viscosity increases (Fig. 3.19b), pure shear and pure extensional flows become more important while other types of flow are less important. Here, the contour level for pure extensional and axisymmetric contraction flow is similar as those in baseline simulation, suggesting that more viscous solutions experience similar strength of extensional flow.

When the syringe is tilted, the joint PDF of invariants is quite different (Fig. 3.19c). In the  $(Q_w, -Q_s)$  map, various types of strain rate are prevalent in the liquids with pure extensional and shear flow showing a slight predominance. The distribution is similar to that of the isotropic turbulent [73], where the liquid motion is characterized by the chaotic changes in pressure and flow velocity. The joint PDF on  $(R_s, Q_s)$  map suggests the axisymmetric contraction is more important. Here, the stretching forces on drug molecules are more likely to be exerted in one dimension, which may be more detrimental to the stability of proteins.

The time evolution of strain rate can be investigated by analyzing the conditional mean values of the invariants. Here,  $\langle Q_s \rangle$ ,  $\langle Q_w \rangle$ ,  $\langle R_s \rangle$  are calculated, which are the mean values of  $Q_s$ ,  $Q_w$ ,  $R_s$  for fluids with  $Q_s > (D_0/2)^2$ , respectively. The time evolution of the mean invariants for  $\theta_t = 60^\circ$  are shown in Fig. 3.20. At state 1, the upper edge of the interface rises along the upper syringe wall, where the fluid motion is dominated by pure extensional flows. Then at state 2, the liquids near the wall is elongated and a large bulb forms at the top of the interface. The fluid strain rate and vorticity increase. The axisymmetric contraction flow is more important. At state 3, the strain rate and vorticity reach their maximum values. A strong shear flow is generated when the liquid on the top penetrates the liquid at the bottom. Here,  $\langle R_s \rangle < 0$ , suggesting that the tube-like contraction flow structure is more

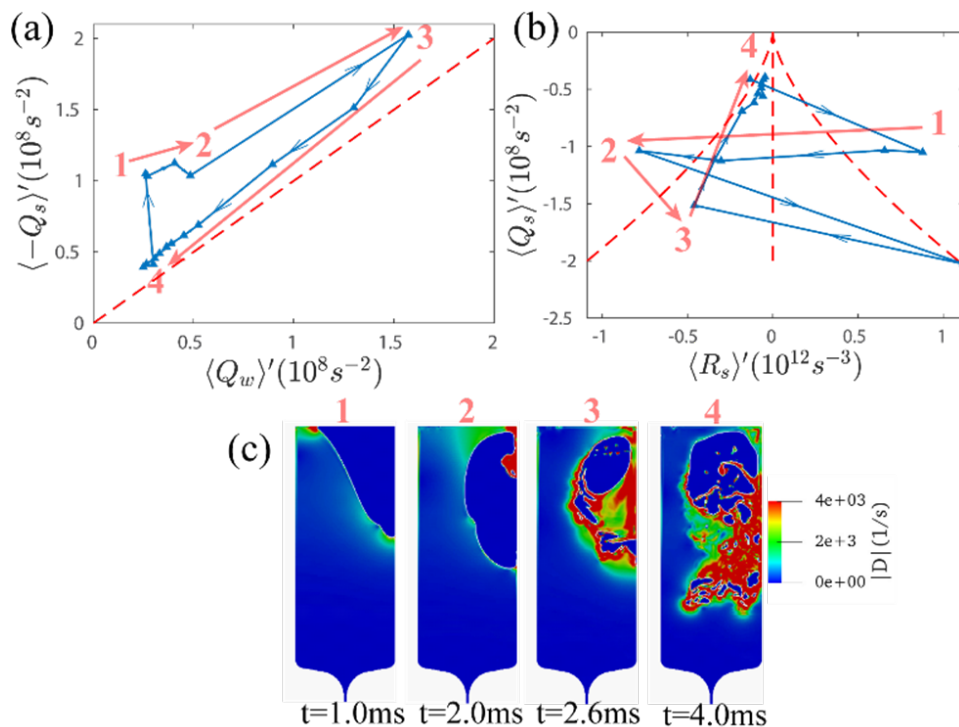


**Figure 3.20.** The trajectories of conditional mean on maps of (a)  $(Q_w, -Q_s)$  and (b)  $(R_s, Q_s)$  for tilt angle  $\theta_t = 60^\circ$ . The cross-sectional strain rate field for states 1~4 are shown in (c).

important in the liquid slosh. Then at state 4, the fluid kinematic energy is dissipated due to the viscous effects. The flow is dominant by the shear flow and contraction flow.

### 3.5 Discussion: effects of slosh on drug

From our calculation, typically  $\sim 1\%$  of protein solutions are subject to strain rate up to  $10^4 s^{-1}$ . This value is on the same order of magnitude as the strain rate created by the pumping and filtration process, where the shear forces on the protein molecules is on the order of 0.1 pN. This shear force is very small compared to the forces required to unfold proteins, approximately 20~150 pN [24], [74]. However, protein molecules have the propensity to be adsorbed by the air-liquid, solid-liquid and oil-liquid interfaces, where forces on molecules can be as large as 140 pN, which is within the range for unfolding [24], [74]. In most cases, the pure hydrodynamic shear is not the reason for denaturation, and the adsorption to the interfaces is a more important factor. Studies by Lin et al. suggest that the change of the

interface area is an important factor in protein aggregate formation [20]. In the experiment, air is pumped into a microbubble, where subvisible particles near the bubble surface is detected. The scaled interfacial area change  $\Delta A/A_0$  is 0.7 and the process occurs in  $\sim 70$  s, where  $\Delta A$  is the difference of the interfacial area and  $A_0$  is the initial interfacial area. In our case,  $\Delta A/A_0$  is 4 $\sim$ 10, and the process occurs in 40 ms. The time scale may seem too small for protein and surfactant molecules to be adsorbed by the air-liquid interface. However, the advective transport is dominant in our problem, meaning that the protein and surfactant molecules are moving with the flow and may still adsorb on the interface. Additionally, some of the formed bubbles may last long after the insertion process.

The time scale of insertion process is very short ( $\sim 40$  ms). However, there is still a possibility for subvisible particle formation including protein aggregation and silicone oil droplets. Our simulations investigate the insertion process where the air bubbles form, of the overall SQ injection process. Most of the bubbles still exist after the insertion process and may last until the drug solution is injected into the tissue. The lifetime of the bubbles is up to several seconds. In addition, the fluid motion can substantially enhance the adsorption of protein molecules on air-liquid interface, which is the main reason for protein aggregation. The Péclet number, which describes the ratio between advective, and diffusive transport can be used to describe the transport of protein and surfactant molecules. The Péclet is defined as  $Pe = U_s R_1 / D_t$ , where  $D_t$  is the diffusivity of solute molecules on the order of  $10^{-10}$  m<sup>2</sup>/s [75]. In our problem, the Péclet number is on the order of  $10^8$ , suggesting that the advective transport is dominant. As the protein molecules are transported by the bulk motion of the liquid, they are more likely to be adsorbed by the air-drug product interface and may form aggregates. There are strict requirements on the acceptable number of subvisible particulates in the drug product (USP<788> particulate matters in injections) as such particles created through protein aggregation or washing of silicone oil from the syringe wall may lead to undesirable immune response.

Cavitation can occur inside syringes during SQ injection [28], where the air-liquid interfaces can be detrimental to protein molecules, but its impact is not in-scope of this paper. Cavitation forms when the local pressure drops below the vapor pressure and the fluid vaporizes. Cavitation may happen during insertion process, when the syringe experiences the

largest acceleration and the liquid pressure at the bottom of the syringe can drop to low pressure values. The cavitation time scale ( 1 ms) is very small compared to the liquid slosh ( 40 ms). The smallest length scale in a turbulent flow can be estimated by the Kolmogorov length  $\eta = \left(\frac{\nu^3}{\epsilon}\right)^{1/4}$ , where  $\nu = \mu_l/\rho_l$  is the the kinematic viscosity of the liquid and  $\epsilon \sim v|\mathbf{D}|^2$  is the average kinetic energy dissipation per unit mass. In our problem, the magnitude of rate-of-strain tensor  $|\mathbf{D}|$  is on the order of  $10^3 \text{ s}^{-1}$ , and the Kolmogorov length is  $0.03\sim 0.14$  mm. The grid size of our simulation (1/12 mm) is in the middle of this range, suggesting that the simulations can fully resolve the turbulence for large viscosity solutions. However, some turbulence in low viscosity solutions has small length scale and may not be fully resolved due to the limitation of grid size.

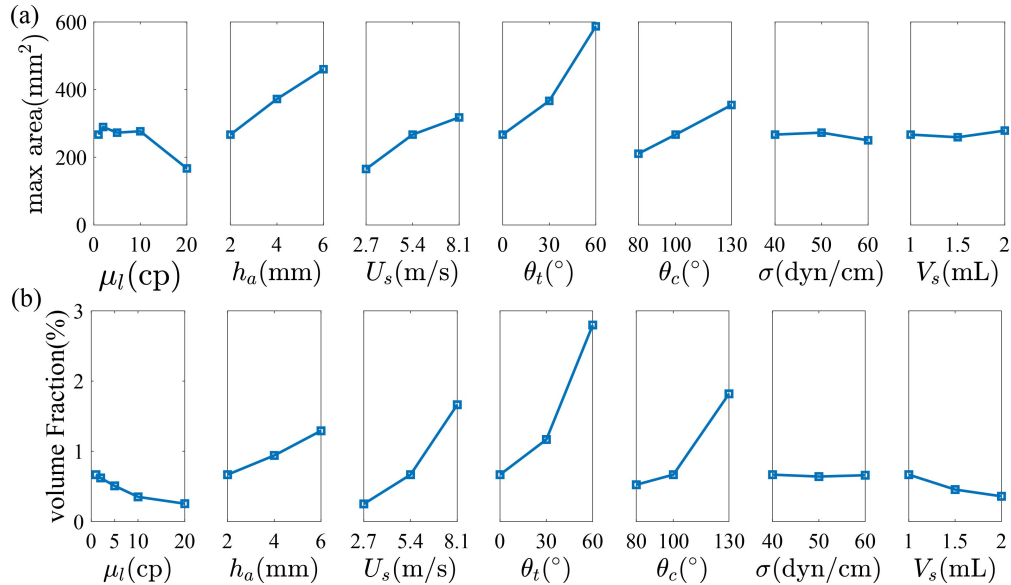


**Figure 3.21.** The summary of dependence of (a) the maximum interfacial area and (b) the volume fraction of liquids with  $|\mathbf{D}| > D_0$  on the liquid viscosity  $\mu_l$ , the air gap height  $h_a$ , the maximum syringe velocity  $U_s$ , the tilt angle  $\theta_t$ , contact angle  $\theta_c$ , surface tension  $\sigma$ , and the fill volume  $V_f$ .

Our results are summarized in Fig. 3.21 and the corresponding dimensionless results are in Fig. 3.22. The definition of the dimensionless numbers (Oh, We) can be found in Table 1. Here, the Ohnesorge number (Oh) is proportional to the fluid viscosity. The Weber number (We) is proportional to the square of syringe velocity. We do not use Reynolds number here because Reynolds number depends on both fluid viscosity and syringe velocity. Both the

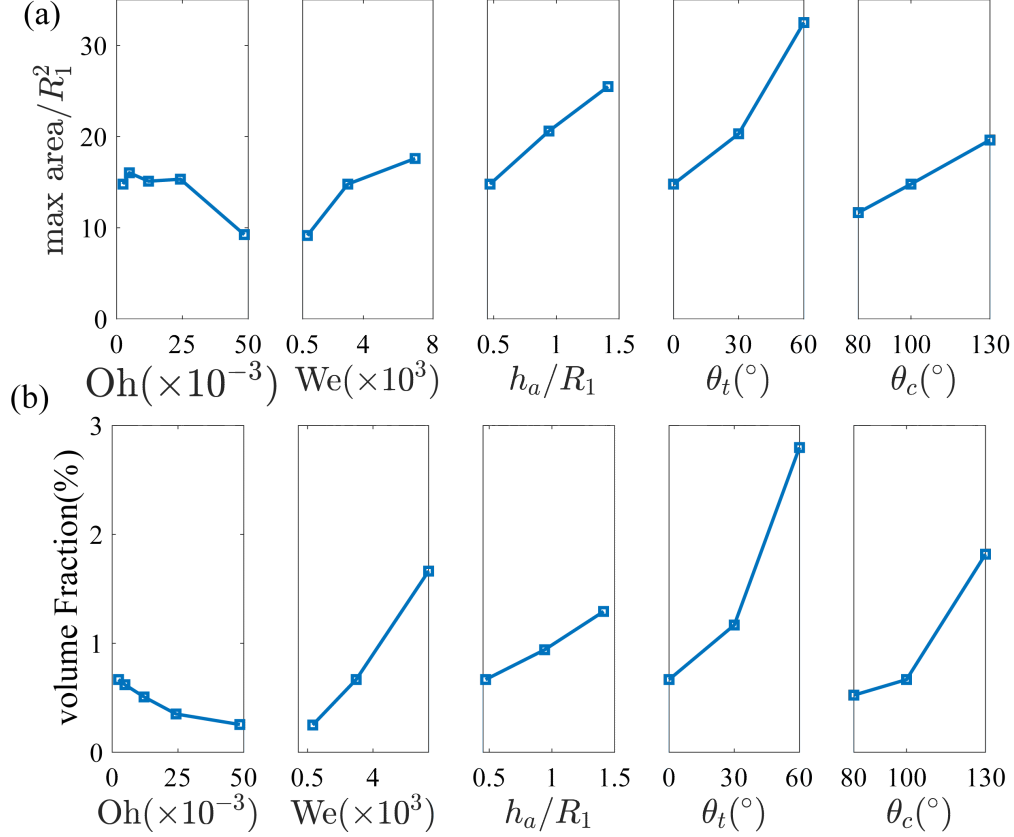


**Figure 3.22.** The summary of dependence of (a) max interfacial area and (b) the volume fraction of liquid with  $|\mathbf{D}| > D_0$  on dimensionless numbers. In (a), the interfacial area is scaled by the square of syringe inner radius.

interfacial area and the volume fraction subject to high strain rate decreases with Oh and increases with We. Increasing in surface tension decreases both Oh and We, thus, we see small effects of changing surface tension. The interfacial area and the volume fraction also change with the dimensionless air gap size  $h_a/R_1$ , contact angle and the syringe tilt angle. Other than the parameters above, the liquid slosh also depends on the acceleration and deceleration time, which can compose two dimensionless numbers. The gravity effects are evaluated by the Bond number. The definition of the Bond number is in Table 1 and its value is relatively small in the current study. In sum, the slosh dynamics can be fully characterized by 8 dimensionless numbers. Five of them (Oh, We,  $h_a/R_1$ ,  $\theta_t$  and  $\theta_c$ ) are investigated in the current study and their effects are presented in Fig. 3.22. A detailed dimensionless study on axisymmetric liquid jet formation process can be found in our previous study [76].

### 3.6 Conclusions

The area of air-liquid interface and the strain rate experienced by the liquid during the liquid slosh caused by autoinjector insertion is investigated, generating insights that may help in assessing the potential impact on protein molecules inside the syringe during autoinjector activation. The simulation results suggest that the interfacial area and amount of liquid subject to high strain rates decrease with the increase in solution viscosity, the air gap height, syringe velocity, tilt angle or wall hydrophobicity, but hardly change with the surface tension or fill volume for a fixed air gap height. Besides, the interface motion occurs mainly at the top of the syringe, and the liquid slosh is independent of the geometry of the needle. Analysis of the rate-of-strain tensor suggests that the increase in the solution viscosity is more effective in reducing the shear flow than the extensional flow, indicating the similar likelihood of damage due to extensional flow. Axisymmetric stretching of protein molecules is enhanced in tilted syringes, leading to more potential damage.

For a given volume of the protein drug solution, a slenderer syringe shape (smaller cross section radius and longer length) is helpful to reduce the interfacial effects and hydrodynamic stress in the liquid slosh, although it is constrained by the standardized design of prefilled syringes. The damage of protein molecules from liquid slosh can also be theoretically decreased by reducing the air gap height, surface hydrophobicity of the lubrication coating on inner wall. The orientation of syringe with respect to gravitational direction also plays an important role in the surface slosh. The least interface area is observed when the axis of syringe is aligned with the direction of gravity. Based on the current results, the tilted insertion with large air gap size and impact speed dictates the worst case in the insertion of auto-injectors, which generates the largest amount of interfacial area and hydrodynamic stress. Future studies on determining the impact of liquid slosh must encompass this worst case to guarantee the reliability of auto-injectors. Some of the findings from this study to reduce sloshing may not be practical for implementation. Please note that the orientation of autoinjector cannot be always in the vertical position in line with gravity due to ergonomic and human factor considerations. The air gap size is imposed by fill-finish equipment, injec-

tion dose requirements, syringe plunger glide force limitations, injection time requirements, and other factors.

Three types of strain rate experienced by the drug solutions are also explored. Strong shear flows occur near the syringe wall, the air-liquid interface and the small bubbles, while only a small volume of fluids is subject to extensional flow. The analysis of the invariants of the rate-of-strain and rate-of-rotation tensors shows (provided in the supplementary material) that for zero tilt angle, the flow is dominant by extensional flow and pure shear flow. While for large tilt angle, the flow patterns are closer to isotropic turbulence, indicating that the hydrodynamic stress environment is more complicated. The contraction tube-like flow structure is more important in the liquid slosh, suggesting that the protein molecules are more likely to be stretched than compressed by the hydrodynamic stresses.

## 4. MODELING CAVITATION BUBBLE DYNAMICS AND ITS IMPLICATION TO PROTEIN MOLECULES

*This chapter will be submitted to International Journal of Pharmaceuticals. The experiments are conducted by Zhongwang Dou.*

### 4.1 Summary

The collapse of cavitation bubbles induced by the acceleration of syringe in an autoinjector device can lead to protein aggregation. The detailed bubble dynamics is investigated using axisymmetric and three-dimensional simulations with passive tracers used to illustrate the transport of protein molecules. When a bubble near the syringe wall collapses, protein molecules are concentrated in the re-entrant jet, pushed toward the syringe wall and then spread across the wall, potentially leading to the protein adsorption and aggregation on walls. This phenomenon is more prominent for bubbles positioned close to the wall and lead to a large maximum radius. The bubble maximum radius decreases with the bubble distance to the syringe wall and air gap pressure and increases with the liquid column height and nucleus size. The strain rate induced by the bubble collapse is not large enough to unfold the proteins. When the re-entrant jet impacts the bubble surface or syringe wall, the bubble breaks up, generating small bubbles with high surface concentration of protein molecules, potentially inducing aggregation in the bulk. The bubble dynamics is influenced by the dimensionless distance of the nucleus from the wall normalized by the maximum bubble radius ( $\gamma$ ). The re-entrant jet velocity increases with  $\gamma$ . While the maximum liquid pressure, typically 100~1000 bar, first decreases and then increases with  $\gamma$ . This high pressure may potentially generate hydroxyl radicals. The coalescence of bubbles in the clouds can occur for bubbles that are very close to each other, leading to a higher pressure at the collapse.

### 4.2 Introduction

Autoinjectors are widely used for subcutaneous injections (SQ) due to their simplicity, reliability, and the ability to be used directly by the patients [50]. Typically, autoinjectors

are designed to deliver a small dose of drug (usually 2.0 mL or less), which are proteins, peptides, oligonucleotides, and amino acid derivatives, e.g., monoclonal antibodies (mAb), epinephrine and interferon [51]. In today's market, most autoinjectors are actuated by a pre-compressed spring. The administration of the drug product is primarily comprised of three phases: device activation, needle insertion and liquid injection (Fig. 4.1(a)) [6], [77]. At the start of needle insertion, the driving rod actuated by the spring strikes the plunger, leading to an abrupt acceleration of the syringe. The liquid pressure near the bottom wall of the syringe decreases and cavitation occurs. The propensity of cavitation depends on the kinematics of the syringe, the presence of nucleation sites (such as microbubbles, debris and surface roughness) and the geometry of the syringe. These cavitation bubbles appear for a very short time (typically on the order of 0.1 ms), where the cavitation bubbles grow and collapse rapidly. Upon the bubble collapse, high temperature and pressure can lead to the thermal dissociation of water into OH- radicals and H atoms. The hydroxyl radicals [14], [78], [79], vapor/air-liquid and oil/solid-liquid interfaces [5], [80] and the hydrodynamic stress [24] in the cavitation process are suggested as the potential causes for the denaturation and aggregation of therapeutic proteins. After the cavitation event, there is a liquid slosh inside the syringe, which can further enhance protein aggregation [77], [81]. The protein aggregates, as a potential trigger of the immunogenic responses in patients, are a great concern to product quality and patient safety [15], [17], [18]. Furthermore, for some autoinjectors, the pressure transient generated by cavitation can be large enough to break the glass and lead to the failure of the devices [3]. This study focuses on the computational fluid dynamics (CFD) simulations of the bubble dynamics and migration of proteins during the cavitation process and quantifies the pressure, air-liquid interface and shear stress to evaluate the effects of cavitation on drug molecules, such as proteins, peptides, oligonucleotides and etc.

Cavitation has been recognized as an important reason for the formation of protein aggregates [14], [78]–[80], [82], [83]. When a glass vial is dropped from a height as low as 10 inches to the ground, a mechanical shock is generated due to the impact, and that is sufficient to induce cavitation, potentially causing protein aggregation in the drug product. By using a high-speed camera, Randolph et al. [14] reported that these cavitation bubbles form within 30  $\mu$ s and then go through growth-collapse cycles periodically over a millisecond

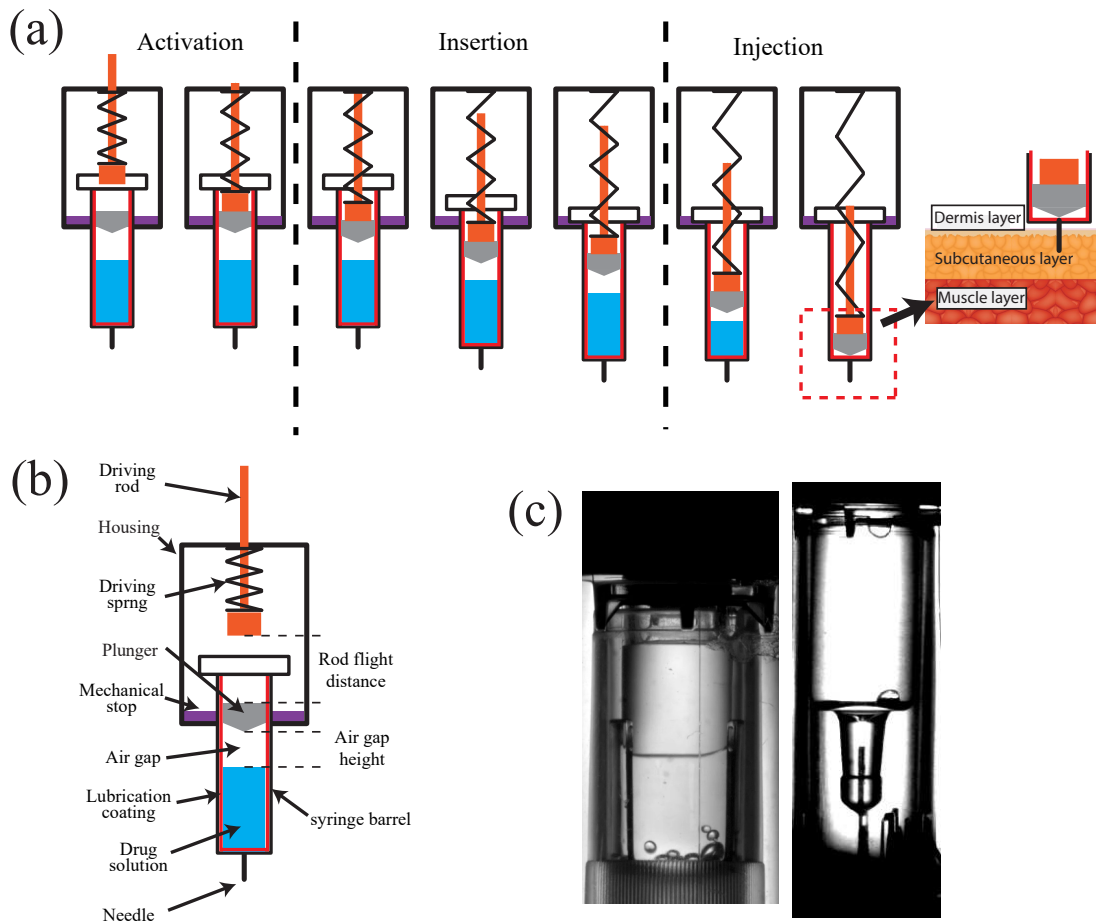


**Figure 4.1.** (a) The administration process is comprised of 3 stages: the activation, the insertion and the injection. The figure is reproduced with permission from [6]. (b) Schematic showing the structure of an autoinjector and the name of each components. (c) Cavitation at the start of the insertion process recorded by a high-speed camera for two different autoinjectors. The lifetime of cavitation bubbles is on the order of 0.1 ms.

time span. Subvisible particle counts increased in the solution and proteinaceous particles were found on the vial walls. The protein particles on the glass vial wall showed an increased level of oxidation, presumably by cavitation induced hydroxyl radicals. In the experiments by Torisu et al. [81], larger amount of subvisible particles were observed after repeated cycles of dropping and shaking at 50 rpm for 100 min and 400 min. The combined effects of dropping and shaking is more remarkable than shaking alone. They proposed that cavitation is important in unfolding the proteins. After unfolding, the denatured protein molecules have

a propensity to adsorb to the inner surface of the vial wall and then desorb into the solution during shaking [84], [85], which can lead to the formation of micron-sized particles. Pure shaking is less likely to generate protein aggregates since the shaking stress is not sufficient to unfold the proteins. However, no significant chemical degradation, including oxidation due to hydroxyl radicals, was detected in the protein aggregates or proteins in solution. Cavitation can be divided into two categories: acoustic cavitation that is generated by an ultrasound, and hydrodynamic cavitation that is generated due to the local pressure drop in a flowing liquid. There are several studies investigating the damaging effects of acoustic cavitation, where the free radicals and hydrodynamic shear can damage different types of protein [79], [86] and DNA molecules [87]. On the other hand, the hydrodynamic cavitation generated by a micro-orifice is characterized by slower dynamics and less hydrodynamic stress. This type of cavitation may not produce sufficient hydroxyl radicals, and the vapor-liquid interface was found there as the main reason for protein aggregation [80], [88].

The interaction between the cavitation bubble and boundaries, such as rigid walls, air-liquid interface and etc., has been extensively studied in the fluid mechanics community, which also provides some insights to understand the cavitation damage. When a bubble collapses in a quiescent fluid near a rigid wall, a re-entrant jet, directed toward to the wall, can form on the bubble surface. The jet attains a high speed in the early stage of the bubble collapse and long before the volume reaches the minimum size [89]. The re-entrant jet can penetrate the other side of the bubble surface and strike the wall if the distance from the wall is sufficiently small. The bubble deforms into an toroidal cavity moving towards the wall while shrinking in volume and may break into small bubbles afterwards [90], [91]. The induced pressure decreases with the distance to the wall for small distances and then increases for large distances, and the highest pressure on wall is detected when the nucleus is attached to the wall [90]. A convex boundary induces a more intense bubble collapse than a flat boundary [92]. Numerical studies also investigate the particle pathlines on the bubble surface. Interestingly, almost all the particles on the bubble surface are transported into the re-entrant jet at the bubble collapse [89], [91], [93]. For protein and surfactant molecules near a cavitation bubble, we expect the same behavior because the time scale of the collapse of cavitation bubble is so small that advection is much more important than diffusion. When

a cloud of cavitation bubbles are generated, the bubble dynamics is also modified by the bubble-to-bubble interactions. The natural frequency of micro-bubble clouds can increase with the bubble concentration, leading to the suppression of the bubble collapse except at the resonant condition [94].

Cavitation bubbles inside the syringe within an activated autoinjector occurs over a very short time ( $\sim 0.1\text{ms}$ ), which is comparable to the time needed for pressure waves to travel through the liquid column - from the bottom wall of the syringe to the top surface of liquid near the syringe plunger [3]. During this small time scale, the pressure in the liquid column is non-uniform, resulting in cavitation formation in some regions of the syringe. Because of its potential impact to the drug products, the mitigation of cavitation damage should be an important consideration in the design of autoinjectors, where the geometry of the syringe, the materials of construction of the syringe components (barrel/plunger) and the method of actuation are crucial to the product reliability and patient safety. In this work, we use computational fluid dynamics simulations of multi-phase, compressible flows to investigate the bubble dynamics in an autoinjector with passive tracers inserted to understand the migration of protein molecules on the bubble surface. In Section 4.4.1, we validate our numerical model by comparing the predicted bubble shape with results of ex-situ experiments (barebone auto-injector removing components that prevent imaging of syringe and solution via block of view). In Section 4.4.2, a one-dimensional (1D) calculation is performed to estimate the bubble radius under the assumption of spherical collapse, which can be used to understand the bubble dynamics away from syringe walls. In Section 4.4.4, axisymmetric simulations are used to investigate the distance of the nuclei from the wall, liquid column height, air gap pressure and nucleus size on the maximum bubble radius and peak pressure. In Section 4.4.5, three-dimensional (3D) simulations are performed to quantify the fully resolved bubble shape and pressure for a single cavitation bubble and for a cluster of bubbles.

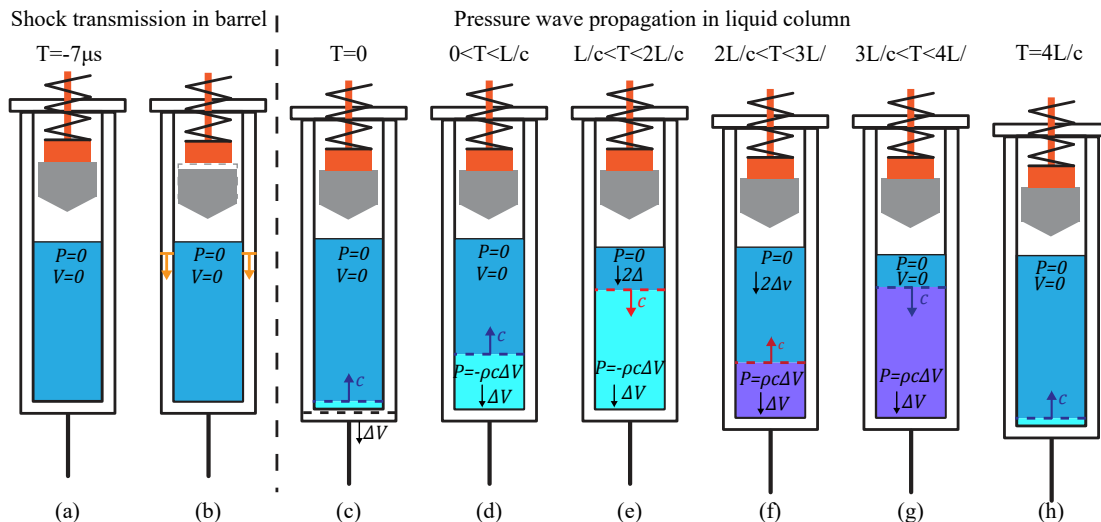


**Figure 4.2.** A schematic of pressure wave propagation in the syringe after the driving rod strikes the plunger.

### 4.3 Method

#### 4.3.1 Problem Definition

Fig. 4.2 shows the shock transmission in the syringe barrel and the propagation of pressure waves in the liquid column after the driving rod strikes the plunger. After the driving rod strikes the plunger, a mechanical shock is generated and transmitted through the syringe barrel. Since the sound speed in the glass is  $\sim 5\text{km/s}$ , the time for this process is only  $\sim 7\mu\text{s}$ . Because we are only interested in the pressure variation in the liquid column, we set time to zero when the syringe bottom starts to move. The syringe bottom gains a downward velocity of magnitude  $\Delta V$  at  $T = 0$  and friction is neglected. The propagation of pressure waves has a period of  $4L/c$  [95], where  $L$  is the liquid column height and  $c$  is the wave speed, approximating the sound speed in water. For  $0 < T < L/c$ , the expansion wave (the pressure behind the expansion wave is lower than that in front of the wave) originated from the syringe bottom travels to the top with the wave speed  $c$ . The liquid behind this wave has a flow velocity  $\Delta V$  and pressure change  $-\rho c \Delta V$ . At  $T = L/c$ , the wave reaches the top air-liquid interface, where the pressure on the air side is zero while the pressure on the liquid side is  $-\rho c \Delta V$ . Due to the pressure difference, the velocity of the liquid near

the interface changes from  $\Delta V$  to  $2\Delta V$  and a compression wave (the pressure behind the compression wave is higher than that in front of the wave) travels from the top toward the syringe bottom. At  $T = 2L/c$ , the compression wave is reflected by the syringe bottom and travels toward the top, where the liquid behind the wave has the pressure  $P = \rho c\Delta V$ . At  $T = 3L/c$ , the wave is reflected by the top air-liquid interface and travels towards the syringe bottom. The liquid behind the wave has zero velocity. At  $T = 4L/c$ , the velocity in the liquid column is zero. The conditions of the liquid column are the same as those at  $T = 0$  and the wave propagation continues as these events repeat with a period of  $4L/c$ . For autoinjectors, the time of acceleration is larger than  $4L/c$ , and we can consider that a series of pressure waves are generated from the syringe bottom at different times. The resulting pressure is the sum of the pressure change induced by the pressure waves. For longer times, the friction becomes important and the pressure waves damp out.

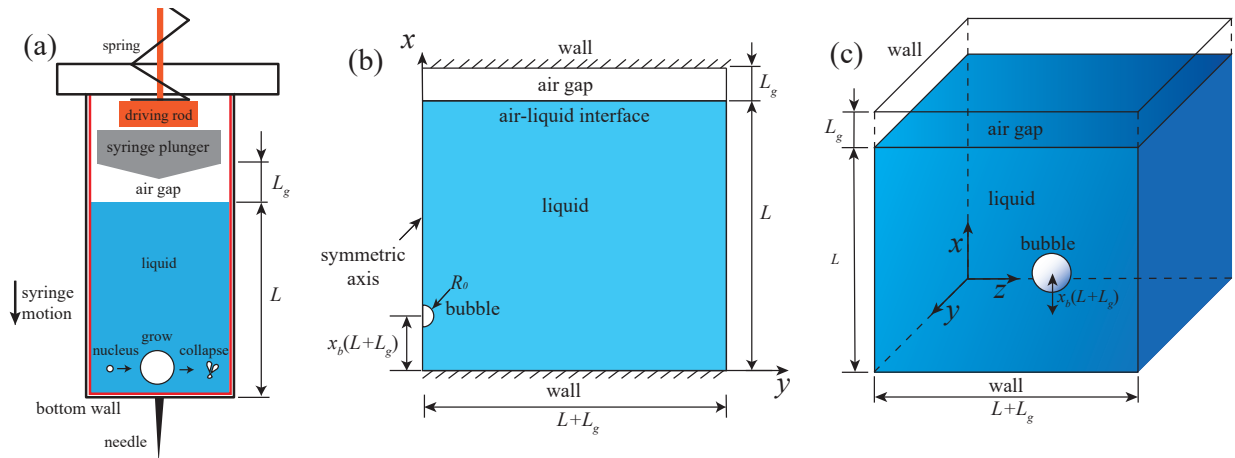


**Figure 4.3.** (a) Schematic of cavitation generation in the syringe. When the bottom syringe wall (near the needle) gains speed, the pressure variation due to pressure waves leads to the bubble growth and collapse. The geometry setup in axisymmetric and 3D simulations are shown in (b) and (c), respectively.

This study focuses on the dynamics of a gas bubble in a container that is partially filled with the drug product leaving a small air gap on the top and is subjected to a sudden motion (Fig. 4.3(a)). The motion generates pressure waves propagating inside the liquid column that are reflected by the top air-liquid interface and the bottom wall, resulting in multiple reverberations of the pressure waves. The acceleration of the syringe bottom wall,

**Table 4.1.** Parameters and fluid properties in the current work.

Parameters	Symbol	Value
liquid column height	$L$	20~50 mm
nucleus radius	$R_0$	0.01~0.2 mm
nucleus location	$x_b$	0~1
syringe inner diameter	$D$	8 mm
air gap size	$L_g$	2 mm
air gap pressure	$P_g$	1~2 bar
surface tension	$\sigma$	72 mN/m
liquid sound speed	$c$	1463.8 m/s
liquid density	$\rho_l$	$10^3$ kg/m <sup>3</sup>
liquid kinematic viscosity	$\nu_l$	$10^{-6}$ m <sup>2</sup> /s
liquid dynamic viscosity	$\mu_l$	$10^{-3}$ Pa·s
gas density	$\rho_g$	1.2 kg/m <sup>3</sup>
gas dynamic viscosity	$\mu_g$	$10^{-5}$ Pa·s

which is used as an input in the simulations, is measured using an accelerometer in ex-situ experiments described in Sec. 4.3.2, where the syringe is set in motion in the same way as in an autoinjector. We consider the wall to be fully rigid and neglect the elastic deformation of the glass syringe wall (heat resistant borosilicate glass, Young’s Modulus 64GPa, thickness 1.11mm) resulting from the propagation of stress waves and the changes in liquid pressure. The nucleus is located at the centerline of the cylindrical syringe with a distance  $x_b(L+L_g)$  away from the bottom wall, and far away from the side walls. We include the effects of the liquid viscosity, the surface tension and the liquid compressibility, but we neglect heat diffusion, phase change and mass transfer effects due to the short time scale of the bubble collapse. In the 1D calculation, the bubble is assumed to remain spherical, thus the loss of symmetry during collapse due to the presence of the wall is not included. This situation is representative of a bubble collapsing in an unconfined domain, which is a good approximation of the physics when the bubble is sufficiently far from the walls. Asymmetric and 3D simulations investigate the non-spherical bubble collapse, where the presence of the bottom wall impedes the bubble growth and collapse and breaks the symmetry of bubble dynamics. The list of parameters are shown in table 4.1.

### 4.3.2 Ex-situ experiment

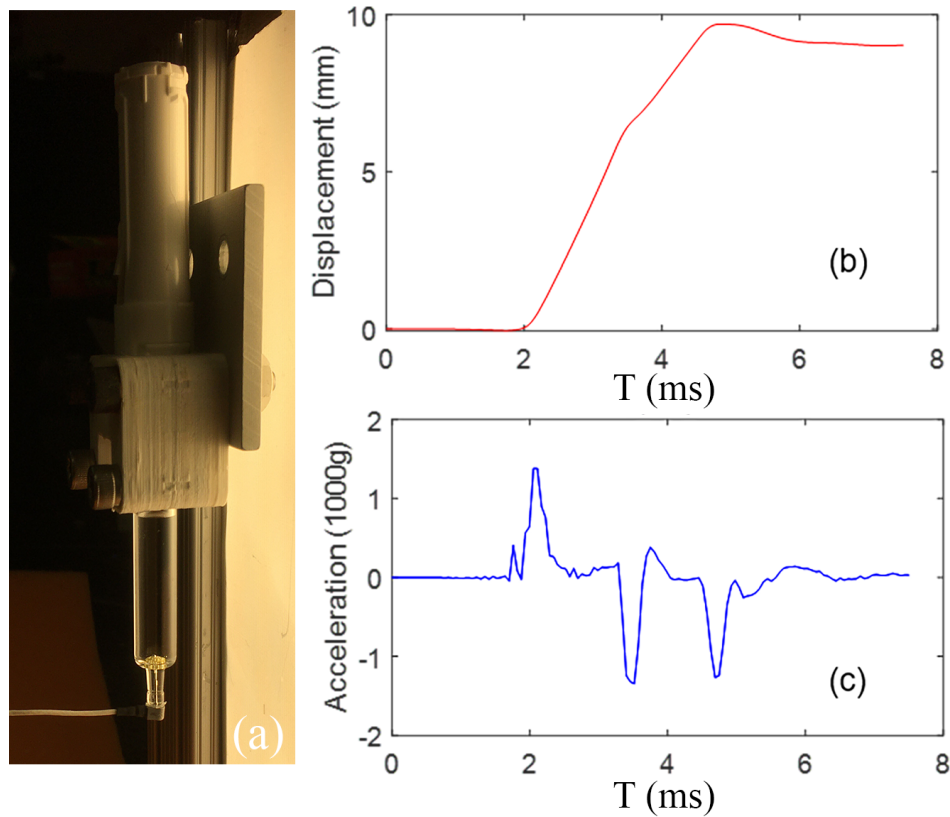


**Figure 4.4.** Experimental setup for simultaneous measurement of displacement and acceleration of syringe using a high-speed camera and accelerometer, respectively. (a) Snapshot of ex-situ autoinjector setup with an accelerometer mounted at the bottom of the syringe. (b) and (c) show the example data of displacement (from the camera) and acceleration (from the accelerometer) of the syringe, respectively.

To validate the numerical model, we conduct ex-situ experiments to obtain the bubble shape and compare it against the numerical results for the same syringe kinematics. To accurately measure the displacement and acceleration of the syringe in an autoinjector, we employ a high-speed camera and an accelerometer in this study. A detailed description of the setup for obtaining the displacement of the syringe using an ex-situ autoinjector characterization setup is given in the previous work [6], [77]. Briefly, to mimic the operating procedures of a single-spring actuated autoinjector, a simplified autoinjector platform is implemented to study the key kinematics during the insertion and injection of the autoinjector

device. The driving rod, spring, and syringe are mounted on a 3D-printed fixture and imaged using an ultra-high-speed camera (Phantom V 2640, Vision Research Inc). An LED light source (Flashlight 300, LaVision) accompanied by a light diffuser (DG100X100-1500, ThorLabs, Inc.) is used to achieve uniform background illumination of the pre-filled syringe. The motion of the driving rod, plunger, and syringe is captured at a rate of 20,000 frame/s. The resolution of each frame is  $15.6 \mu\text{m}/\text{pixel}$  and  $1960 \times 656$  pixels.

To measure the acceleration of the syringe in the autoinjector, an ultra-miniature Integrated Electronics Piezo-Electric (IEPE) accelerometer (Dytran 3224A2) is employed. The experiment uses a 2.25 mL long glass syringe (BD Neopak) with an inner diameter of 8.5 mm. The spring force before release is 12N. The needle of the syringe is removed and the bottom of the syringe is polished to flat using a 320 grid sandpaper so a flat bottom of the syringe can be utilized to mount the accelerometer (Fig. 4.4a). We further block the syringe outlet using glue so that the accelerometer is not pushed by the liquid. Note that this study is mainly focused on the needle insertion phase of actuation of the autoinjector, when no liquid flows through the needle yet. Therefore, the blockage of the syringe outlet does not affect the syringe kinematic. Besides, since the mass of the accelerometer and the syringe with the drug product is 0.2 g and 8 g, respectively, the accelerometer causes only a 2.5% weight increase of the ex-situ autoinjector system. We therefore neglect the effect on the inertia of the system caused by adding the accelerometer. The accelerometer is sampled at 17,066 Hz via a modular data acquisition (DAQ) system (NI 9174, 9250, 9260) via the Data Acquisition Toolbox in MATLAB (R2018b, MathWorks, Inc.). To ensure the same time zero for measurement using the high-speed camera and accelerometer, we synchronize them via the same DAQ system [96]. When the recording of the accelerometer signal starts, the DAQ system also sends a trigger signal to the high-speed camera to initialize the image recording. The data of displacement and acceleration is given in Fig. 4.4 (b) and (c). All the testing instrumentations are calibrated and carefully tested before each experiment. In the current study, we are not able to control the number of nuclei and the location of nuclei. For the purpose of validation, we only use the experimental runs where only one cavitation bubble forms. Then, the distance between the bubble and the bottom syringe wall is measured and used as an input for the simulations.

### 4.3.3 One-dimensional equation for bubble dynamics

One-dimensional (1D) equations are used to estimate the pressure wave propagation in the syringe and the dynamics of a spherical bubble collapse. The propagation speed of the pressure wave in the liquid is assumed to be the speed of sound in water. For real syringes, the wave speed can be slightly lower than the sound speed due to the elasticity of the syringe wall [95]. If air bubbles exist in the liquid, the air contents can also decrease the wave speed. To simplify the problem, we make the variables dimensionless by dividing by the scales listed in table 4.1.

**Table 4.2.** Non-dimensionalization in the 1D calculation.

Dimensionless variables	Symbol	Scale
Distance	$x$	$L$
Fluid velocity	$v$	$c$
Time	$t$	$L/c$
Pressure	$p$	$\rho c^2$
kinematic viscosity	$\nu$	$cL$
surface tension	$\sigma$	$\rho c^2 L$

When the syringe is subjected to a sudden acceleration, a water hammer or pressure wave is generated. The pressure change caused by the pressure wave is a function of location and time, denoted as  $p_w(x, t)$  and governed by the following equation set [95]

$$\text{Continuity: } \frac{\partial p_w}{\partial t} = -\frac{\partial v}{\partial x}, \quad (4.1)$$

$$\text{Momentum: } \frac{\partial v}{\partial t} = -\frac{\partial p_w}{\partial x} - m_f, \quad (4.2)$$

$$\text{Initial Conditions: } p_w(x, 0) = 0, \quad v(x, 0) = 0, \quad (4.3)$$

$$\text{Boundary Conditions: } v(0, t) = -v_s(t), \quad p_w(1, t) = p_g, \quad (4.4)$$

where  $x = 0$  is located at the bottom wall, and  $x = 1$  is located at the air-liquid interface on the top,  $m_f = \frac{fL}{2D}|v|v$  accounts for the friction between the liquid and the syringe wall,  $f$  is the Darcy–Weisbach friction factor [95],  $v_s(t)$  is the syringe velocity, measured from our experiments (Fig. 4.5),  $p_g$  is the air gap pressure and  $v$  is the fluid velocity in the laboratory reference frame. The role of gravity is negligible and the pressure wave is hardly damped by

the wall friction, thus  $m_f$  is neglected in our calculation. The absolute pressure of the liquid is

$$p = p_w + p_r, \quad (4.5)$$

where  $p_r$  is the reference pressure, which is the atmosphere pressure (1 bar) in the current calculation.

Assuming the nucleus to be a small gas bubble, we use the liquid pressure  $p$  to calculate the time evolution of the bubble radius using the Keller-Miksis equation, which describes the dynamics of a cavitation bubble in a compressible liquid [97], [98]:

$$(1 - \dot{r}) r \ddot{r} + \frac{3}{2} \dot{r}^2 (1 - \dot{r}) = (1 + \dot{r}) [p_B(t) - p(t)] + r \frac{dp_B}{dt} \quad (4.6)$$

where  $r(t)$  is the dimensionless bubble radius as a function of time and dots indicate the time derivative,  $p$  is the liquid pressure from Eq. 4.5 evaluated at the nucleus site. The initial condition on the bubble radius is  $r(0) = R_0/L$  and  $\dot{r}(0) = 0$ . The pressure on the liquid side of the bubble interface is

$$p_B(t) = p(0) \left( \frac{r}{r(0)} \right)^{-3k} - 2 \frac{\sigma}{r} - 4\nu \frac{\dot{r}}{r}, \quad (4.7)$$

where  $p(0) = p_r + 2\sigma/r(0)$  is the gas pressure inside the bubble at  $t = 0$ ,  $k = 1.4$  is the polytropic exponent for an adiabatic process. The effects of surface tension and viscosity are usually negligible for large bubbles and only affect the dynamics of very small bubbles. When the rate of change of bubble radius is much smaller than the sound speed, i.e.  $\dot{r} \ll 1$ , this equation reduces to the Rayleigh-Plesset equation, which accounts for the bubble dynamics in an incompressible liquid.

The equation set (Eq. 4.1-4.4) for wave propagation is solved using the finite difference method on a staggered grid. The liquid column is discretized into 50 cells with the pressure data stored at the cell center and the velocity stored on the cell face. Derivatives with respect to space are calculated using the central difference scheme and the explicit Euler method is used for the time integration. The convergence of the equation set is subjected to the CFL condition  $\text{Co}_{acoustic} = \Delta t/\Delta x \leq 1$ , where  $\text{Co}_{acoustic}$  is the acoustic Courant number,  $\Delta t$  is

the time step,  $\Delta x$  is the cell size. The time step is  $\Delta t = \Delta x = 1/50$ . Equation 4.6 is an ordinary differential equation and the bubble radius is integrated with respect to time using an explicit 3rd-order Runge-Kutta method [99].

#### 4.3.4 Axisymmetric and 3D simulations of bubble collapse

The compressible multiphase flow solver in Basilisk [100] is used, which is an extension of the all-Mach semi-implicit solver using the Volume-of-Fluid method [101] to resolve the gas-liquid interface. The solver supports adaptive mesh refinement and utilizes the interface reconstruction method to improve the accuracy of the volume fraction fields. Liquid compressibility is considered so that acoustic waves are captured in the solver. The thermal diffusion and mass transfer inside the bubble are neglected due to the short time scale of interest. The non-dimensionalization introduced in 1D calculation is not used in this section. The governing equations, which are derived from the continuity and momentum equations, are

$$\frac{\partial C}{\partial t} + \nabla \cdot (\mathbf{v}C) = C\nabla \cdot \mathbf{v}, \quad (4.8)$$

$$\frac{\partial \rho \mathbf{v}}{\partial t} + \nabla \cdot (\rho \mathbf{v} \mathbf{v}) = -\nabla P + \nabla \cdot \boldsymbol{\tau} + \sigma \kappa \nabla C - \rho \mathbf{a}_s, \quad (4.9)$$

where  $C$  is the liquid volume fraction, which is 1 for the liquid phase and 0 for the gas,  $\mathbf{v}$  is the flow velocity vector,  $P$  is the pressure, and  $\boldsymbol{\tau} = \mu (\nabla \mathbf{v} + \nabla \mathbf{v}^T) - \frac{2}{3} \mu (\nabla \cdot \mathbf{v}) \mathbf{I}$  is the viscous stress tensor with  $\mathbf{I}$  being the identity matrix,  $\kappa$  is the curvature of the interface,  $\nabla C$  calculates the gradient of  $C$  and is normal to the interface,  $\mathbf{a}_s$  is the syringe acceleration. The mixture density and viscosity are  $\rho = C\rho_f + (1 - C)\rho_g$ ,  $\mu = C\mu_f + (1 - C)\mu_g$ , respectively. Because the cavitation occurs in a very short time, the fluid is assumed to undergo an adiabatic process. The equation of state for both the liquid and gas is

$$\frac{P + \Pi}{\rho^k} = \text{constant}, \quad (4.10)$$

where for gas  $\Pi = 0$  and  $k = 1.4$ , for liquid water  $\Pi = 3 \times 10^8$  Pa and  $k = 7.14$  [102], [103]. The numerical schemes are the same as in the work by Fuster et al. [101] except that we

do not solve the energy equation and assume both liquid and gas to undergo an adiabatic process.

Both axisymmetric and 3D simulations (Fig. 4.3) are conducted in the reference frame of the syringe. For axisymmetric simulations, the domain is a square of size  $L + L_g$  and for 3D simulations, it is a cube of size  $L + L_g$ . The nucleus bubble is initially placed at the origin and the lower boundary of the domain, which is positioned at  $x = -x_b(L + L_g)$ , is the bottom syringe wall. An air gap of height  $L_g$  with the initial pressure  $P_g$  is added on the top of the simulation domain. The initial gas pressure inside the bubble is  $p_r + 2\sigma/R_0$ . We assume that the acoustic impedance of the top and bottom walls is infinite and neglect the coupling of the air gap and the plunger motion. No-slip no-penetration boundary conditions are applied for the bottom and top boundaries and side boundaries are free-slip walls. The maximum bubble diameter is typically less than 0.1 of the domain size so the bubble can be considered unbounded in y and z directions. The parameters and fluid properties are shown in Table. 4.1.

An adaptive mesh refinement is used in the simulations and the grid is refined by limiting the error on the volume fraction, the fluid flux, the density and the pressure to be smaller than a predefined threshold. The error on each variable for each cell is calculated based on the absolute change of the variable after the cell is refined by one level. The grid size far away from the bubble surface is large,  $1/2^6$  of the system size, while the grid size near the bubble surface and in regions of large pressure variation is small with the minimum size  $\Delta x$ , which is  $1/2^{13}$  for axisymmetric simulations, and  $1/2^{11}$  for 3D simulations. The time step size is controlled by constraining the maximum acoustic Courant number  $Co_{acoustic} = c\Delta t/\Delta x \leq 5$  and the maximum Courant number  $Co = v_{max}\Delta t/\Delta x \leq 1$ , where  $v_{max}$  is the maximum flow velocity in the simulation. The solver requires the Courant number to be less than or equal to 1, but allows the acoustic Courant number to be larger than 1. A large acoustic Courant number can cause numerical dissipation resulting in the smoothing of sharp wave-fronts, but this effect has been mitigated by refining the mesh in the vicinity of the wave front [101].

Surfactants and protein molecules have a propensity to adsorb to gas-liquid interfaces. To investigate the migration of surfactants and protein molecules near the bubble surface, we add inertia-less passive tracers on the bubble interface at  $t = 0$ . Due to small errors in the

Volume of Fluid method, some tracers may depart from the interface. In the simulation, we correct the tracer position at each time step by adding a small displacement normal to the reconstructed interface to make sure the tracers remain attached to the gas-liquid interface. The tracers are initialized at  $(R_0 \cos \phi, R_0 \sin \phi)$  for axisymmetric simulations, and  $(R_0 \cos \phi, R_0 \sin \phi \cos \theta, R_0 \sin \phi \sin \theta)$  for 3D simulations, where  $\phi$  is the azimuthal angle uniformly spaced in the range  $[0, \pi]$ , and  $\theta$  is the polar angle uniformly spaced in the range  $[0, 2\pi]$ .

## 4.4 Results

### 4.4.1 Validation against experiments using axisymmetric simulations

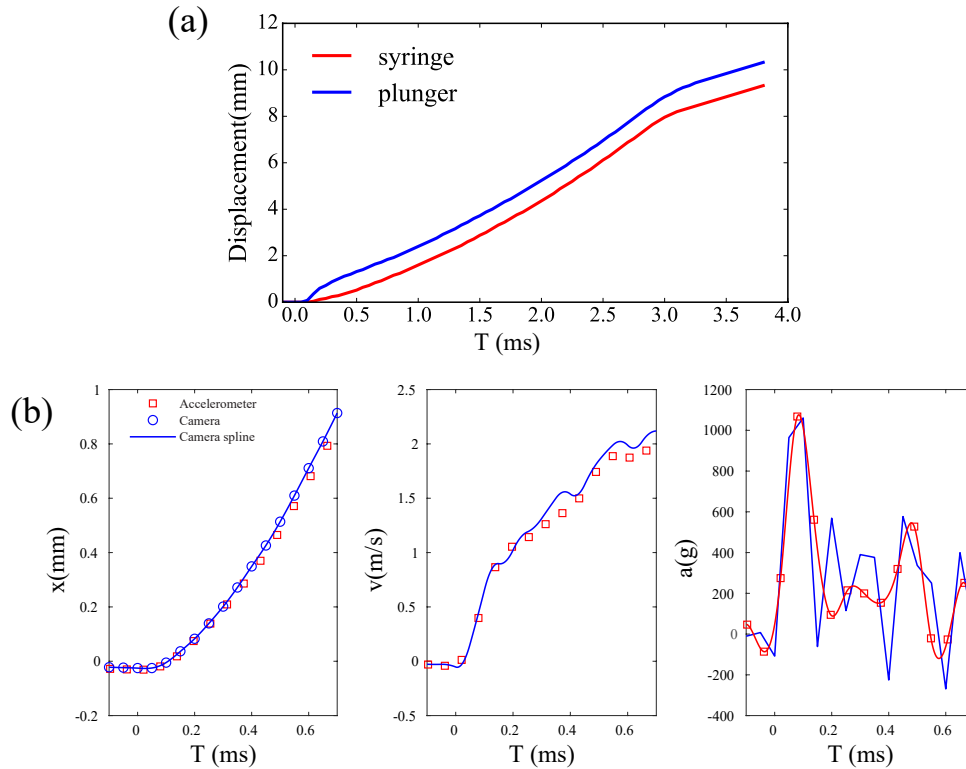


**Figure 4.5.** (a) Displacement of the plunger and the syringe bottom recorded by the camera in ex-situ experiments. When the driving rod impacts the plunger, the plunger is pushed and the air on top of the solution is compressed. Later, the plunger and syringe move together with the same speed. (b) The syringe displacement, velocity and acceleration upon impact.

Fig. 4.5(a) shows the displacement of the plunger and the syringe bottom during the start of the spring-driven needle insertion process. We set the time zero at the instant when the driving rod strikes the plunger. Here, the plunger has a larger displacement than the syringe, indicating the plunger is moving relative to the syringe and the air gap on the top is being compressed. Shortly afterwards, the syringe accelerates and moves together with the plunger. The air gap is around 2.8 mm at the start and then decreases to 2.2 mm as the driving rod pushes on the plunger. Given that the initial air gap pressure is the atmosphere pressure (1 bar) and the air gap undergoes an adiabatic process, we derive the air gap pressure after the impact, which is  $(2.8/2.2)^{1.4} = 1.4$  bar. This value is used as the initial air gap pressure in the simulations validated against experiments. Here, the compression of the air gap occurs in  $\sim 0.2$ ms. In the simulations, this process is assumed to occur instantly after the impact and the air gap pressure undergoes a step change. This pressure change can induce a pressure wave inside the liquid column, competing against the expansion waves originating from the bottom, reducing the bubble growth and contributing to an early collapse of the cavitation bubbles. In simulations, the wave front of pressure wave generated by the top air gap is sharper than that in the experiments. But since the pressure magnitude of this wave is much weaker than that generated by the bottom wall, the increase of sharpness has a small effect on the pressure field and bubble dynamics. In Fig. 4.5(b), we measured the displacement using the camera and the acceleration using the accelerometer. Because cavitation occurs over a very short time and only a limited number of data points are collected within the interested time frame, we use cubic smoothing spline fitting in MATLAB to recover the displacement and acceleration curve. For data points  $(x_i, y_i)$ , the resulting spline function  $f(x)$  is obtained by minimizing  $\sum_i (f(x_i) - y_i)^2 + \lambda \int f(x)^2 dx$ , where  $\lambda$  is the smoothing parameter and is  $10^{-6}$  and  $10^{-8}$  for displacement and acceleration spline curves, respectively. By taking the 1st and 2nd order derivatives of the displacement curve, we get the velocity and acceleration based on the camera. By integrating the acceleration data, we get the velocity and displacement based on the accelerometer. The simulations use the smoothing spline fit of the acceleration measured with the accelerometer as an input. Parameters used in the simulations are: the liquid column height  $L = 34$  mm, air gap size is  $L_g = 2$  mm. The center of the nucleus bubble is 0.648 mm away from the bottom syringe

wall, i.e.,  $x_b = 0.018$ . The experiments cannot provide a measurement of the nuclei size and we use very small nuclei size  $R_0 = 0.05\text{mm}$  in simulations. The simulation results suggest that nucleus size smaller than this value hardly changes the bubble dynamics. Other parameters are listed in Table. 4.1.

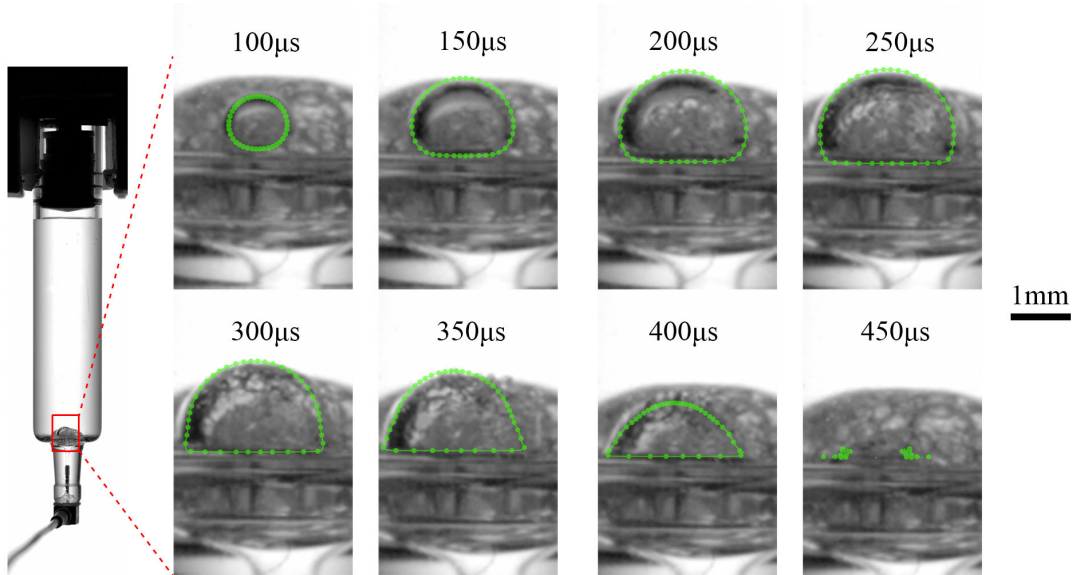


**Figure 4.6.** Experimental images of a cavitation bubble compared with the simulation results (green line). Passive tracers (green dots) are added in the simulations to illustrate the protein migration on the bubble surface.

The cavitation bubble shape observed in the experiments is compared with the simulation results in Fig. 4.6. Even if the fluid used in the experiments is water, we still add the passive tracers in simulations to indicate the proposed protein migration on the bubble surface. The rod strikes the plunger at  $t = 0$  and the syringe starts to accelerate after  $\sim 10\mu s$ . At  $t = 100\mu s$ , the cavitation bubble appears and grows until  $t = 330\mu s$ . After  $t = 330\mu s$ , the syringe acceleration oscillates with a smaller amplitude and the pressure inside the syringe can increase due to wave reflection or the decrease of syringe acceleration at some instant, which causes the bubble to collapse. The lower side of the bubble is bounded by the syringe wall and tracers are focused into the re-entrant jet formed on the upper side of the bubble surface. The bubble collapses in a very short time ( $\sim 10\mu s$ ). The details of bubble collapse will be discussed in section 4.4.4 and 4.4.5.

#### 4.4.2 1D calculation of bubble dynamics

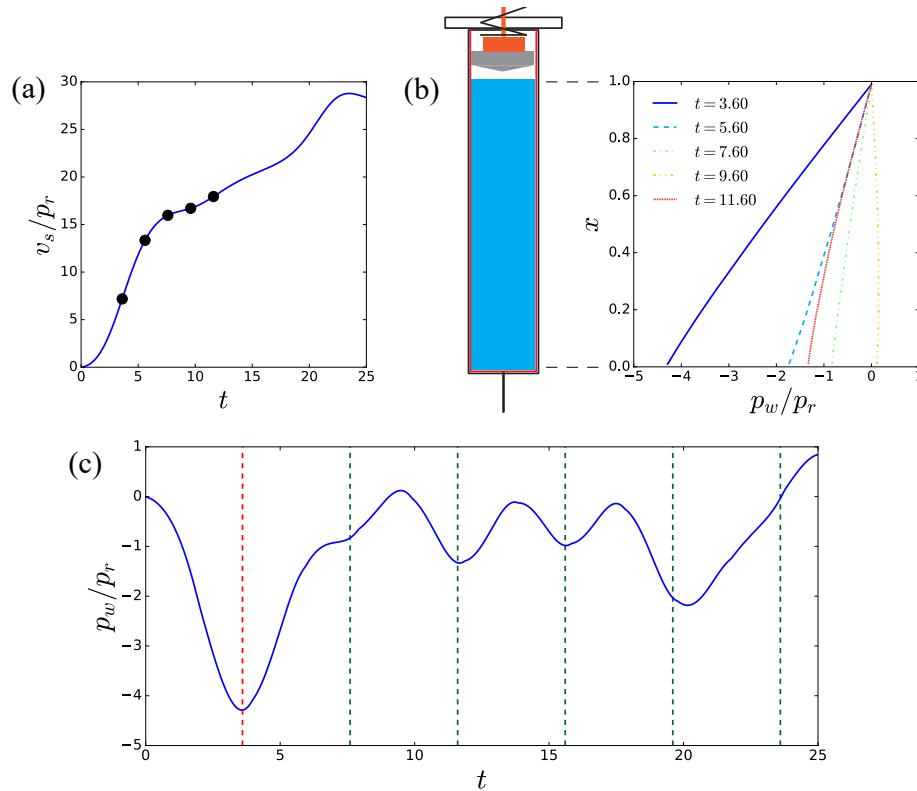


**Figure 4.7.** (a) The dimensionless syringe velocity  $v_s$  normalized by the dimensionless atmosphere pressure  $p_r$ .  $v_s/p_r = 1$  corresponds to the velocity change to induce a pressure drop of one atmosphere pressure. (b) The pressure variation in the liquid column with height  $L = 34\text{mm}$  due to the propagation of the pressure wave. (c) The pressure change at the syringe bottom,  $x = 0$ . The maximum acceleration occurs at  $t = 4.6$ , inducing the strongest pressure drop (red dashed line). The oscillation of pressure wave causes the pressure inside the syringe to oscillate with a period of  $4L/c$ . Pressure wave induced by the first acceleration peak can be reflected by the syringe bottom inducing subsequent pressure drops (green dashed line).

Fig. 4.7(a) shows the syringe velocity  $v_s(t)$  obtained by integrating the acceleration measured with the accelerometer. Fig. 4.7(b) shows the spatial distribution of pressure in the liquid column at different times obtained using Eq. 4.1-4.4. Values are reported in dimensionless form following Table 4.2. The change of syringe velocity can generate expansion pressure waves that travel inside the liquid column and is reflected by the bottom syringe wall and air-liquid interface on the top. As we discussed previously, the oscillation of

the pressure wave has a period of 4 (time unit is  $L/c$ ). In Fig. 4.5(b), the maximum syringe acceleration occurs at  $T = 84$  ms, which is  $t = 3.6$  after scaling. At the same moment, the pressure at the syringe bottom reaches its minimum, which is about 4 bar below the atmosphere pressure. The expansion wave induced by this acceleration impulse travels from the bottom syringe wall towards the top air-liquid interface and is reflected as a compression wave traveling back to the bottom syringe wall. Thus, the syringe bottom experiences high pressure at  $t = 5.6, 9.6, 13.6$ , etc (Fig. 4.7(c)). Then, the pressure wave is reflected by the bottom syringe wall and travels back to the bottom wall, inducing low pressure at  $t = 7.6, 11.6, 15.6$ , etc. The low pressure values enhance the cavitation bubble growth, while the high pressure values hinder the bubble growth and contribute to the bubble collapse. When the pressure variation is large enough, the bubble becomes unstable and collapses to very small sizes. Typically, cavitation bubbles are dominated by inertia and they are more likely to collapse after a high pressure and before a low pressure, which is the time interval  $[9.6, 11.6], [13.6, 15.6]$ , etc. At around  $t = 20.6$ , there is a secondary peak in the acceleration profile (Fig. 4.5(b)), where the pressure further decreases and the bubble can experience a second growth.

Fig. 4.8 shows the pressure experienced by the bubble and the corresponding time evolution of the bubble radius. Due to the propagation of pressure waves, the pressure experienced by the bubble oscillates with a period of  $4L/c$ . Meanwhile, the bubble also undergoes growth-collapse cycles, whose frequency is dependent on the wave magnitude and bubble size. Under certain conditions, the two processes can resonate, resulting in a stronger collapse and higher pressure. Bubbles positioned further away from the bottom syringe wall experience smaller pressure variations (Fig. 4.8), therefore, the maximum bubble size and the duration of the growth-collapse cycle decreases. This is because the pressure at the top air-liquid interface is always the same as the air gap pressure, so that bubbles closer to the top experience smaller pressure variations. This result is consistent with the experiments of Kiyama et al. [41], where cavitation bubbles were generated in a free falling tube that hit the ground. The maximum bubble size in the experiments decreased with the distance from the tube bottom. When the liquid column height  $L$  increases, the magnitude of pressure variation increases (Fig. 4.8(b)). The pressure variation can be considered as a sum of

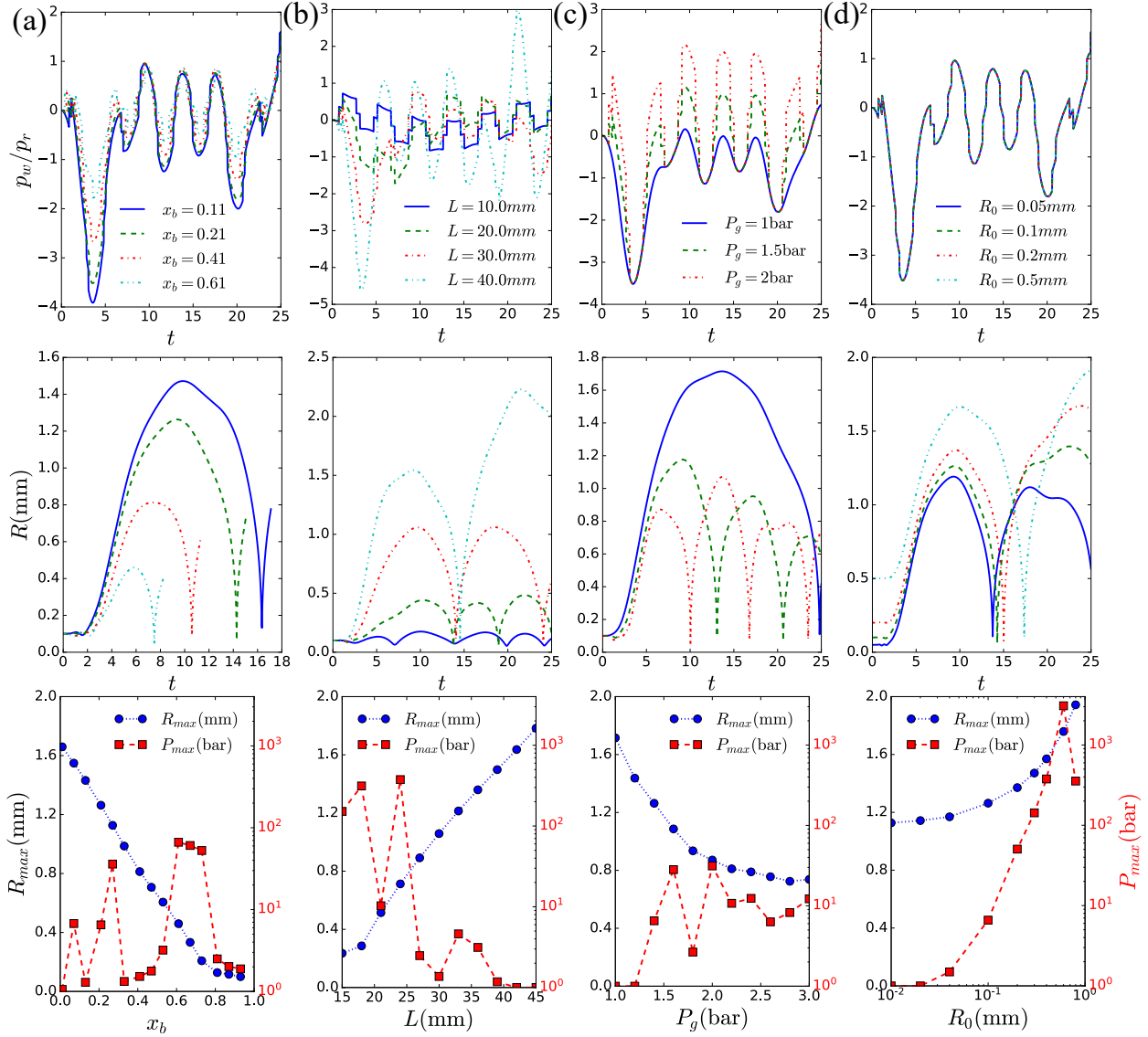


**Figure 4.8.** Pressure variation experienced by the nucleus, radius and the maximum radius for different (a) nucleus location  $x_b$ , (b) liquid column height  $L$ , (c) air gap pressure  $P_g$  and (d) nucleus size  $R_0$ . The second row shares the legend with the first row. Default parameters are  $x_b = 0.2$ ,  $L = 34$  mm,  $P_g = 1.4$  bar,  $R_0 = 0.1$  mm. The pressure is greatly underestimated here, because 1D calculation assumes the bubble to be spherical. Scaling of the dimensionless variables are listed in Table 4.2.  $r$  and  $r_{max}$  are dimensionless radii normalized by  $R_0$ .

pressure induced by a series of pressure waves described in Fig. 4.2. The pressure drop at the syringe bottom is  $-\rho c \Delta V$ , where  $\Delta V$  is the velocity change of the syringe bottom in a half period  $2L/c$ . When the liquid column height increases,  $\Delta V$  increases and the syringe bottom experiences a larger pressure drop. The bubble size and the time of bubble growth-collapse cycle also increases with the liquid column height. When the air gap on the top is compressed, a compression pressure wave is generated at the top and propagates towards the syringe bottom, contributing to some pressure peaks (Fig. 4.8(c)). When the air gap pressure increases, the maximum bubble size and the duration of bubble growth-collapse cycle decreases abruptly. The nucleus size  $R_0$  does not affect the pressure variations (Fig. 4.8(d)). When the size of nucleus bubble is smaller than  $0.05mm$ , the maximum bubble size does not depend on the nucleus size. While for larger nucleus bubbles, the maximum bubble size increases with the nucleus size. Here, the bubbles are assumed to be spherical. The proximity to the walls and the presence of pressure waves can break the spherical symmetry, leading to the formation of re-entrant jets. The calculations using 1D equations provide an insight on the bubble collapse in the bulk liquid far away from walls caused by a smooth acceleration, where the spherical symmetry is not violated. For non-spherical bubble collapse, this 1D calculation greatly underestimates the pressure and the results of axisymmetric simulations are applicable which are discussed in the next section.

#### 4.4.3 Mesh dependence of axisymmetric simulations

An adaptive mesh refinement is used in our simulations, where the grid is refined based on the error of the volume fraction, fluid flux and density. Away from the bubble, the grid size is large and is  $1/2^6$  of the system size, while near the bubble the grid size is small with the minimum size  $\Delta x$ . To assure the results are independent of the grid resolution, we conducted axisymmetric simulations for  $\Delta x = 1/2^{12}$ ,  $1/2^{13}$ ,  $1/2^{14}$ . In Fig. 4.9(a), the interface shape and the location of passive tracers are similar for three different grid sizes before the first collapse of the toroidal bubble ( $t \leq 439.2\mu s$ ). After the bubble collapse, small bubbles are generated and bubble dynamics may slightly changes with the minimum grid size. The bubble radius, jet velocity and the maximum liquid pressure for  $\Delta = 1/2^{12}$ ,

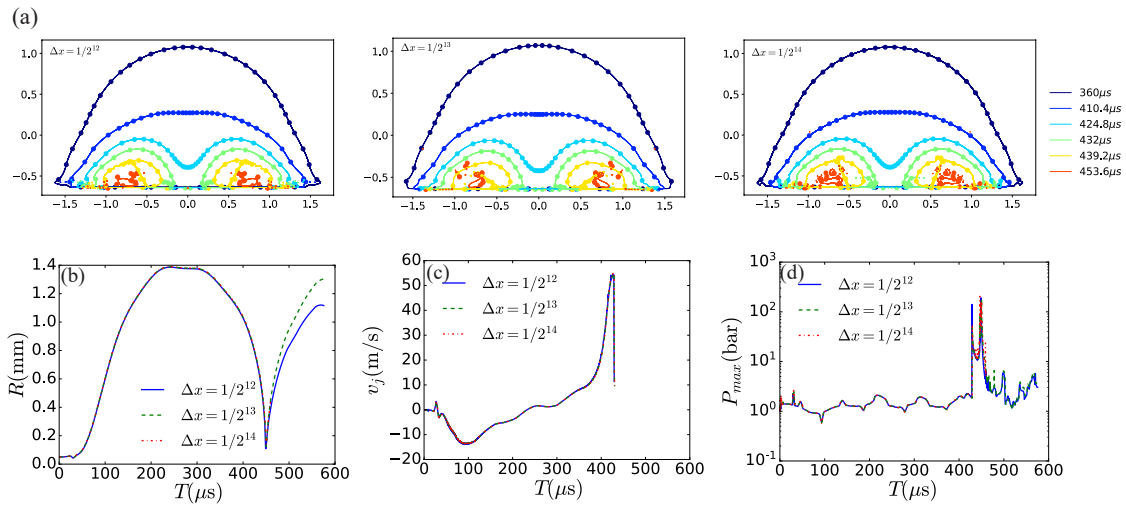


**Figure 4.9.** Mesh dependence of the axisymmetric simulations. (a) The interface shape and tracer locations for different grid sizes and (b) the corresponding bubble radius, (c) jet velocity and (d) maximum liquid pressure.

$1/2^{13}$  and  $1/2^{14}$  also show a good agreement. This indicates that our results converge with the grid size and the current simulations with the grid resolution  $\Delta = 1/2^{13}$  are independent of the grid size.

#### 4.4.4 Axisymmetric simulation for a non-spherical collapse

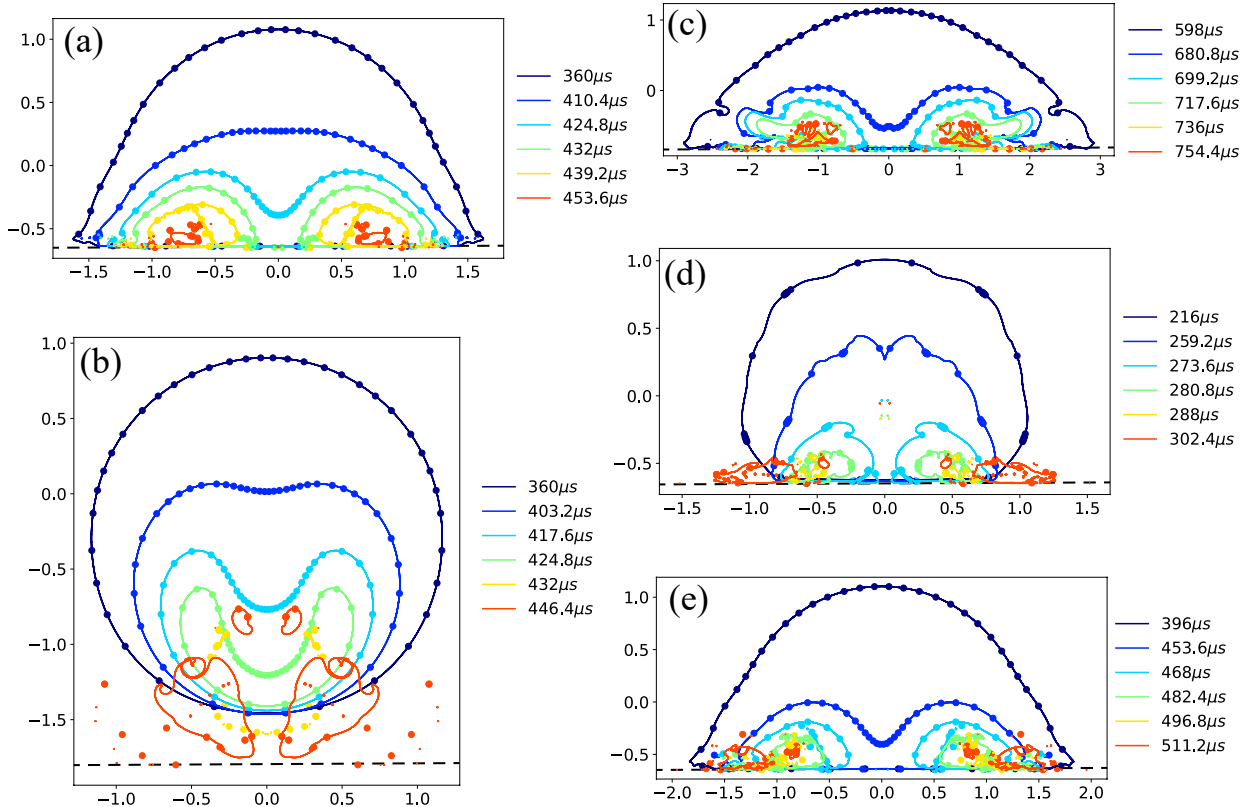


**Figure 4.10.** Time evolution of the bubble surface and tracers (indicated by dots) for (a) baseline simulation, (b) larger distance of the nucleus from the wall,  $x_b = 0.05$ , (c) larger liquid column height  $L = 44$  mm, (d) larger air gap pressure  $P_g = 2$  bar and (e) larger nucleus size  $R = 0.2$  mm. The bottom syringe wall is indicated by the horizontal dashed line, which is  $x = -0.648$  in (a) and (c-d), and  $x = -1.8$  in (b). Length is in unit of millimeter. Default parameters are  $x_b = 0.018$ ,  $L = 34$ mm,  $R = 0.05$ mm.

Axisymmetric simulations are conducted to investigate the effects of the re-entrant jet formation due to the impedance of the wall and the formation of the pressure waves. We start with a baseline simulation with the same setup as the validation simulation ( $x_b = 0.018$ ,

$L = 34$  mm,  $R = 0.05$  mm), and vary only one parameter at a time to study the effect of each variable. Here, 40 tracers are uniformly placed on the bubble surface at the start of simulation to illustrate the migration of protein molecules on the bubble surface.

When a cavitation bubble collapses near the syringe bottom wall, a re-entrant jet forms on the bubble surface that is far away from the wall (Fig. 4.10 (a)). The tracers follow the flow and are concentrated in the re-entrant jet, suggesting that the protein molecules near the cavitation bubble are entrained by the re-entrant jet. The increase in the local concentration of protein molecules can potentially induce protein aggregation [20]. Then the re-entrant jet impacts the syringe wall, where the protein molecules can be adsorbed by the syringe wall or silicone oil layer on the syringe wall [5], [104]. The bubble deforms into a toroid with part of it broken into smaller bubbles. The toroid continues to collapse. As the re-entrant jet strikes the syringe wall, a stagnation point arises in the flow, which rotates the toroid and spreads tracers and bubbles across the syringe wall. These phenomena of protein migration due to the collapse of cavitation bubbles may explain the formation of a proteinaceous film on the syringe or vial walls observed in various experiments [14], [81], [84].

For bubbles with a larger distance to the bottom syringe wall (Fig. 4.10(b)), the re-entrant jet may not directly hit the syringe wall but can penetrate the other side of the bubble surface. The bubble collapses to its minimum size and then rebound bubble becomes a toroid. Part of the bubble is broken into smaller bubbles with a surface covered by highly concentrated protein molecules. When the liquid column height increases (Fig. 4.10(c)), the duration of the bubble growth-collapse cycle increases and the bubble becomes more sensitive to the subsequent secondary peaks in the acceleration profile. The secondary peaks in the acceleration profile cause the bubble shape to deform into an irregular shape at  $T = 680\mu s$ . When the air gap pressure increases (Fig. 4.10(d)), the pressurization of the air gap results in the formation of a stronger compression wave propagating from the top surface to the bottom wall. This compression wave overcomes the expansion wave generated by the syringe acceleration at the start of the rod impact, causing the nucleus to shrink and lose its spherical symmetry. Later on, the syringe acceleration increases and bubble grows. The protein molecules are concentrated in the concave regions of the bubble surface at  $T = 260\mu s$ .

The nucleus size has relatively small effects on the bubble shape and migration of protein molecules (Fig. 4.10(e)).

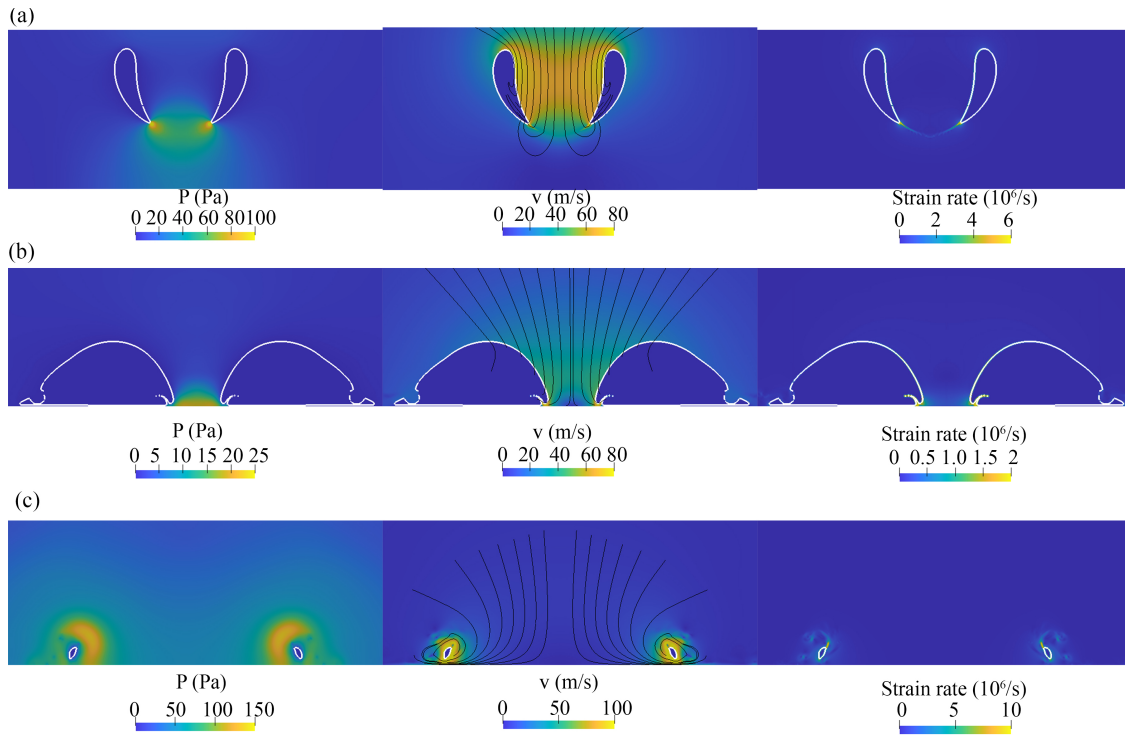


**Figure 4.11.** The pressure, flow and strain rate fields at the instant when the pressure peaks are generated: (a) The jet impacts the bubble surface for a large distance to the wall  $x_b = 0.05$  at  $428.4 \mu\text{s}$ , (b) The jet impacts the bottom syringe wall in the baseline simulation at  $432 \mu\text{s}$  and (c) the toroidal bubble collapses into the minimum size in the baseline simulation at  $450 \mu\text{s}$ . Streamlines are indicated by black curves.

For bubbles far away from the wall, a high pressure is generated when the re-entrant jet impacts the bubble surface (Fig. 4.11(a)). Here, the high-speed re-entrant jet suddenly impacts the other side of the bubble surface, generating a strong pressure wave on the order of  $\rho cv_j/2 \sim 100 \text{ bar}$ , where  $v_j$  is the jet velocity at the impact [105]. The impact also generates a strain rate on the order of  $10^6 \text{ s}^{-1}$ . For the baseline simulation, where the bubble is closer to the bottom wall, there are two pressure peaks. The first pressure peak occurs when the re-entrant jet impacts the syringe wall (Fig. 4.11(b)). The generated pressure wave is on the order of  $\rho cv_j$ . The second pressure peak occurs when the toroidal bubble collapses to its minimum size (Fig. 4.11(c)). There is a stagnation point in the flow at the

center of the toroid. The toroidal bubble rotates with a high speed and spreads across the syringe wall. High pressure is generated in the inner rim of the toroidal bubble. Here, the strain rate is on the order of  $10^6\text{s}^{-1}$  and only lasts for  $\sim 10\ \mu\text{s}$ . It has been reported that the pure strain rate required for unfolding protein molecules is as high as  $5 \times 10^7\ \text{s}^{-1}$  [24]. Given that the strain rate lasts for a very short time and does not reach the required value for protein unfolding, the hydrodynamic shear near the cavitation bubbles may not be sufficient for protein denaturation.

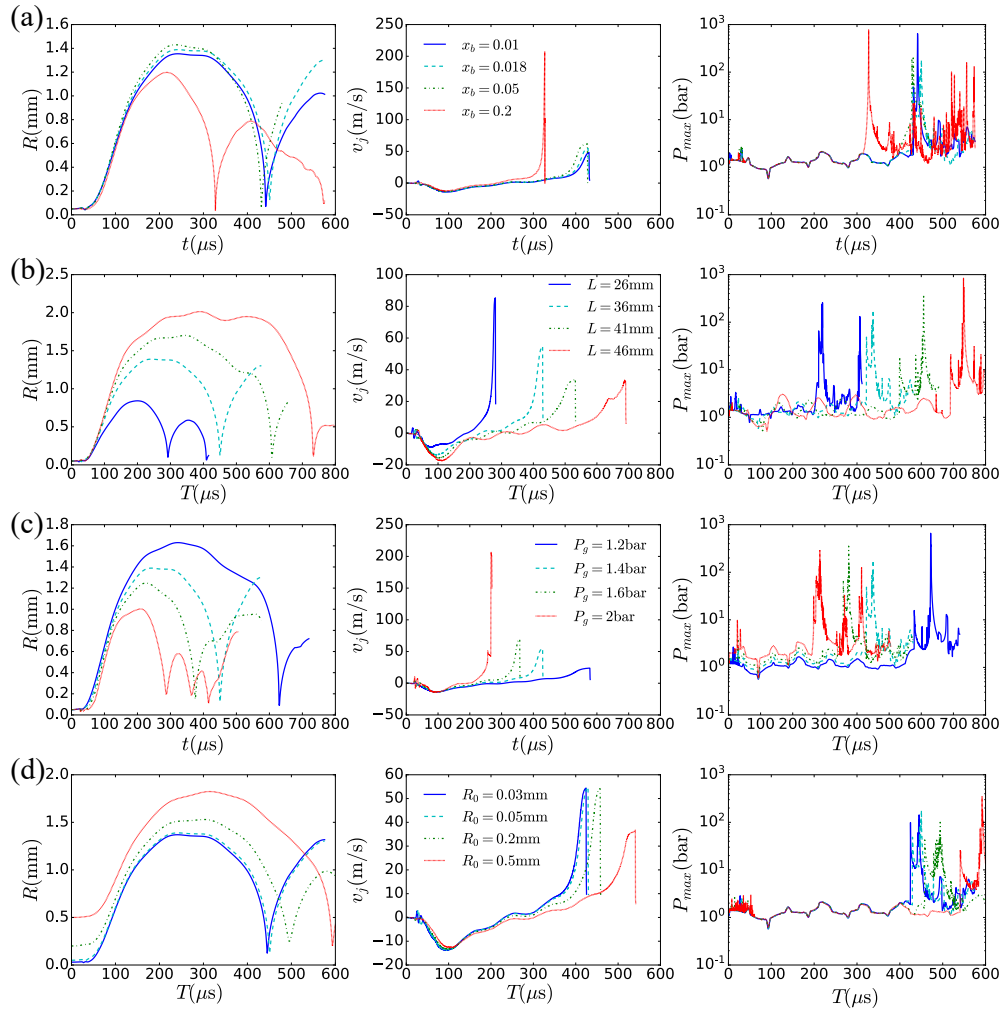


**Figure 4.12.** Time evolution of equivalent bubble radius, re-entrant jet velocity, maximum liquid pressure for different values of (a) distance to the bottom syringe wall, (b) liquid column height, (c) air gap pressure and (d) nucleus size. The first and third columns share the same legend as the second column.

The time evolution of the bubble radius is similar to those from the 1D calculation (Fig. 4.12), which is characterized by the bubble growth-collapse cycle superimposed with the oscillation induced by the change of acceleration and pressure wave propagation. In the axisymmetric simulations, an increase of bubble distance to the bottom syringe wall reduces the impedance effects of the wall (fig. 4.12(a)), leading to an increase of the re-entrant jet velocity. For a bubble far away from the wall ( $x_b > 0.01$ ), the highest pressure is generated when the re-entrant jet impacts the bubble surface. This pressure peak increases with the jet velocity, and thus increases with the distance to wall. While for a bubble close to the wall ( $x_b < 0.01$ ), the maximum pressure increases with a decrease in bubble distance to the bottom syringe wall. This agrees with the experimental results of laser-induced bubble near rigid walls, where the pressure first decreases with the distance to the wall and then increases [90].

When the liquid column height increases (Fig. 4.12(b)) or the air gap pressure decreases (Fig. 4.12(c)), the bubble can grow to a larger size and the time of bubble growth-collapse cycle increases. It takes a longer time for the bubble to collapse and during the bubble collapse, the re-entrant jet can be slowed by the low pressures generated by the pressure waves reflection and noises in the syringe acceleration. The re-entrant jet velocity decreases and the first pressure peak, which is generated due to the jet impact on the bottom syringe wall, also decreases. However, a high pressure can still be generated in the subsequent pressure peaks, when the toroidal bubble or smaller bubbles collapse to their minimum size. Therefore, a high pressure is also observed for a high liquid column height and low air gap pressure. The bubble size and the time of growth-collapse cycle increase with the nucleus size for large nuclei (Fig 4.12(d)). The jet velocity and maximum pressure also decrease. Here, the equivalent bubble radius is defined as  $R = (3V/4\pi)^{1/3}$ , where  $V$  is the bubble volume. The re-entrant jet velocity is measured from the flow velocity on the axis at the bubble surface that is away from the wall. We only measure the jet velocity until it impacts with the bubble surface or the bottom syringe wall.

The results of the maximum bubble radius, jet velocity and maximum liquid pressure for different parameters are summarized in Fig. 4.13. The maximum bubble radius slightly increases with the distance of the bubble from the bottom syringe wall for a very small

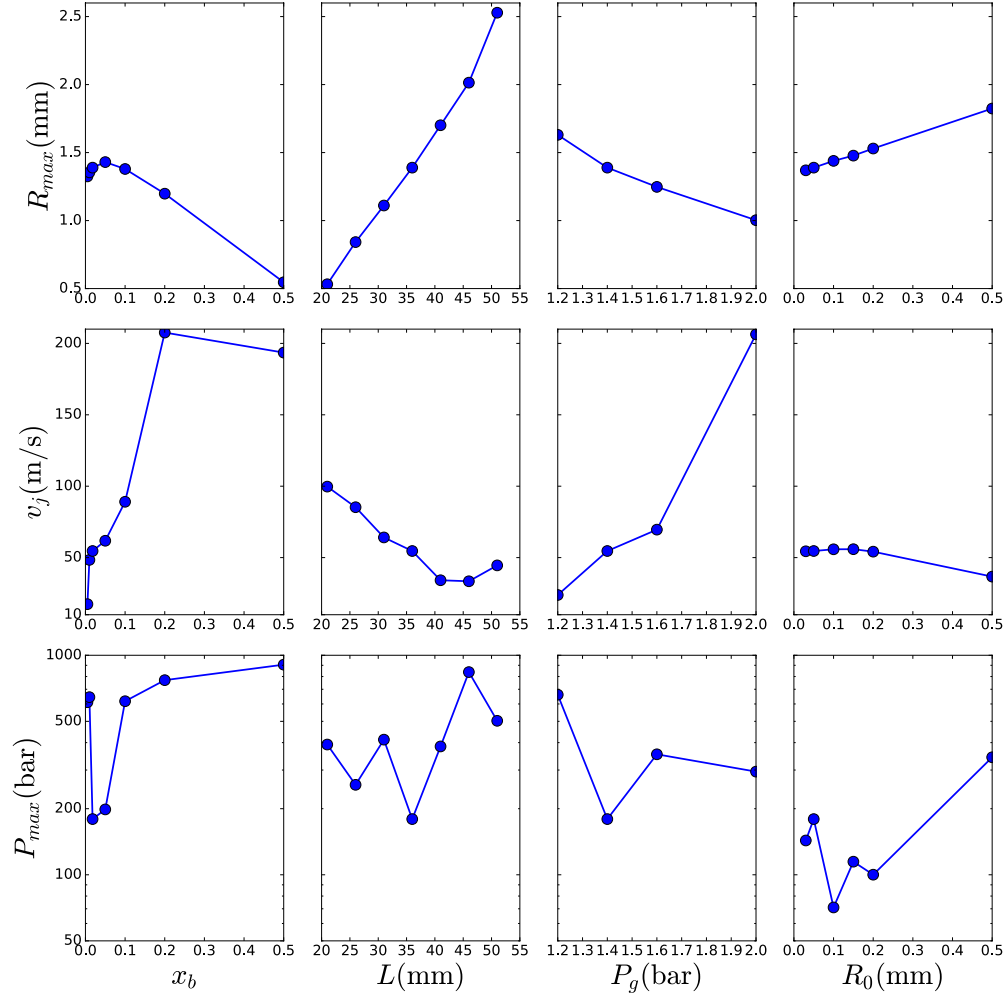


**Figure 4.13.** The dependence of bubble radius  $R_{max}$ , jet velocity  $v_j$ , and liquid pressure  $P_{max}$  on the nucleus location  $x_b$ , liquid column height  $L$ , air gap pressure  $P_g$  and nucleus size  $R_0$ . Other parameters are the same as the baseline simulation ( $x_b = 0.018$ ,  $L = 36$  mm,  $P_g = 1.4$  bar,  $R_0 = 0.05$  mm).

distance and then decreases. The bubble radius also increases with the liquid column height and nucleus size but decreases with the air gap pressure. These trends agree with the results calculated using the 1D model. The jet velocity decreases with the maximum bubble radius, but a high liquid pressure is present for both small and large bubbles. The first pressure peak is usually generated by the re-entrant jet impacting on the bubble surface or syringe wall, which is more prominent for smaller bubbles. Subsequent to the first peak, the toroidal bubble can collapse and break into smaller bubbles that also undergo growth-collapse cycles.

The pressure due to the bubble collapse is more prominent for large cavitation bubbles. The results can also be described by a dimensionless variable  $\gamma = x_b(L + L_g)/R_{max}$ , which is defined as the ratio of the distance of bubble center from the bottom syringe wall over the maximum bubble radius. Here, larger  $\gamma$  indicates that the bubble is far away from the bottom wall and its growth and collapse are less affected by the wall. The variable  $\gamma$  is proportional to  $x_b$ . Thus, the jet velocity increases with  $\gamma$  and pressure decreases with  $\gamma$  for  $\gamma < 0.4$  and increases with  $\gamma$  for  $\gamma > 0.4$ . When the liquid column height increases,  $R_{max}$  undergoes a stronger increase, thus  $\gamma$  slightly decreases and the jet velocity decreases. When the nucleus size  $R_0$  increases, the maximum bubble radius  $R_{max}$  slightly increases, thus,  $\gamma$  slightly decreases and the jet velocity also decreases.

#### 4.4.5 3D simulations of bubble dynamics

To study the fully-resolved bubble shape near the bottom wall, we conduct 3D simulations with 400 tracers (20 for the azimuth and 20 for polar angles) added on the initial interface. Here, we use a larger nucleus size ( $R_0 = 0.2\text{mm}$ ) due to the limitation of grid resolution and other parameters are the same as the validation simulation. The bubble shape is similar to our axisymmetric simulation results but also includes non-axisymmetric instabilities on the bubble surface. At  $T = 454 \mu\text{s}$ , the re-entrant jet starts to form on the bubble surface that is away from the wall with the tracers concentrated at the jet tip. Then the jet strikes the bottom syringe wall at  $T = 468 \mu\text{s}$ , and the bubble collapses into a small toroid at  $T = 497 \mu\text{s}$ . After the collapse, small bubbles with high protein concentrations are generated at the outer rim of the toroidal bubble. Then, the toroidal bubble grows with its bottom surface carrying passive tracers to rapidly spread across the wall. Some small bubbles are advected to the top of the toroidal bubble. The bubble shape shows a qualitative agreement with those of axisymmetric simulations and experimental observations. The results suggest that the collapse of cavitation bubbles near the wall pushes the protein molecules toward the wall and spreads them across the wall surface. Small bubbles with a high protein concentration on the surface may also be generated during the process.

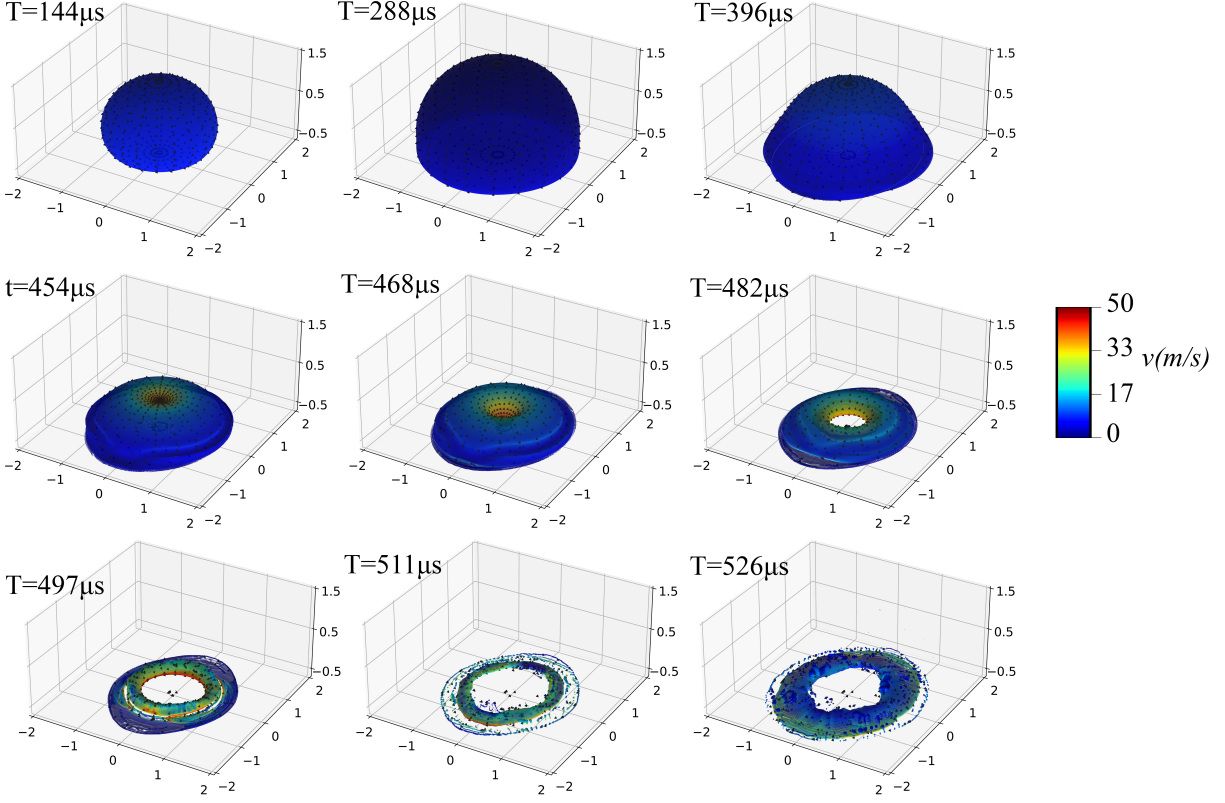


**Figure 4.14.** The interface shape and passive tracers (black dots) for a bubble collapse in a 3D simulation. The face color of the interface indicates the magnitude of the flow velocity. Length is in the unit of millimeter. Here,  $x_b = 0.018$ ,  $L = 34\text{mm}$ ,  $P_g = 1.4\text{bar}$ , and  $R_0 = 0.2\text{mm}$ .

In most of cases in our experiments, there are multiple nuclei inside the liquid and a cloud of cavitation bubbles occur near the syringe bottom. We also investigated the bubble dynamics of a bubble cloud consisting of 4 nuclei initialized at random locations. We added 400 tracers (20 for azimuth and 20 for polar angles) on each bubble. The shape of each bubble is different and dependent on the the bubble-bubble and bubble-wall interactions. In Fig. 4.15, the left three bubbles are close to their nearby bubbles compared to the one on the right. The growth and collapse of the left three bubbles are more impeded by the nearby bubbles, exhibiting longer duration of the growth-collapse cycle. For a bubble cloud, the proximity of nearby bubbles can generate re-entrant jets pointing toward the nearby bubbles, and thus towards the cloud center [106]. Here, the bubble cloud is close to the

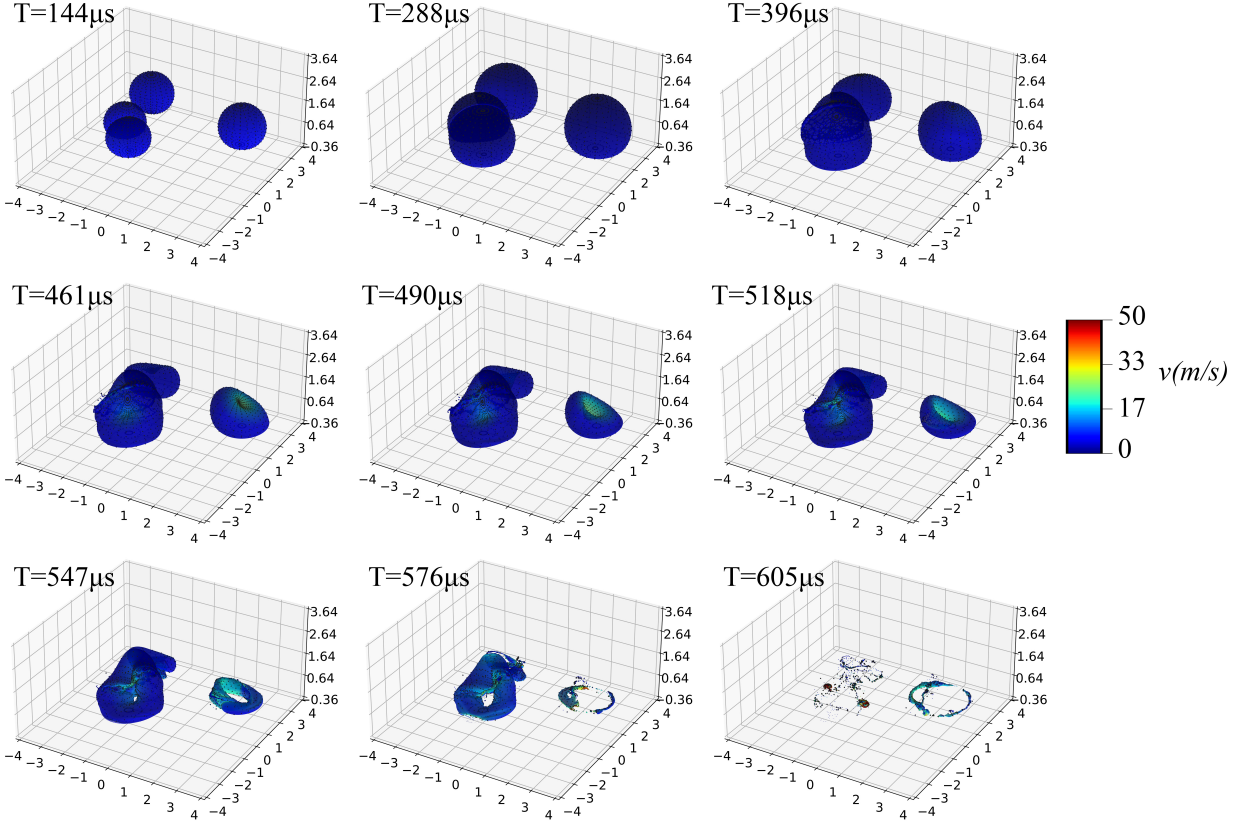


**Figure 4.15.** The interface shape and passive tracers (black dots) for a bubble cloud consisting of 4 nuclei of size  $R_0 = 0.2$  mm. The face color of the interface indicates the magnitude of the flow velocity. Length is in unit of millimeter.

bottom syringe wall, the re-entrant jets shoot towards somewhere between the cloud center and the wall. The passive tracers, or protein molecules, are concentrated in the jet and pushed toward the nearby bubbles and the wall. When two bubbles are very close to each other, coalescence can occur during the bubble growth. This results in a larger bubble and a higher pressure at the bubble collapse. Here, the liquid column height is  $L = 34$  mm. The air gap size is  $L_g = 2$  mm with pressure  $P_g = 1.4$  bar. The four nuclei are of the same radius 0.2 mm and location  $x_b \in [0.01, 0.04]$ :  $(0.42, -1.49, -0.047)$ ,  $(0.80, -2.08, 2.70)$ ,  $(0.54, -1.98, 0.60)$ ,  $(0.66, 2.15, 2.44)$  in unit of millimeter. The wall is positioned at  $x = -0.36$  mm.

In comparison to the collapse of a single nucleus bubble, the bubble clouds generate more pressure peaks, thus high liquid pressures are sustained for a longer time period (Fig. 4.16). The highest pressure is generated due to the collapse of the large bubble resulting from the

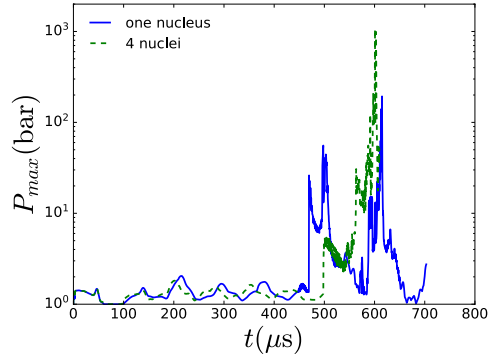


**Figure 4.16.** The maximum liquid pressure for a single nucleus and a bubble cloud of 4 nuclei.

bubble coalescence. The highest pressure is approximately 1000 bar and is larger than that of a single nucleus bubble.

## 4.5 Discussion

### 4.5.1 Implication to drug molecules

The syringe configuration such as the liquid column height, air gap size and the acceleration when the driving rod impacts the plunger are important factors in the cavitation inception in autoinjectors. The simulation suggests that the bubble size increases with the liquid column height and decreases with the air gap pressure. From ideal gas law, the air gap pressure is inversely related to the air gap size. For a given plunger displacement during the rod impact, a smaller air gap leads to a stronger pressure, mitigating the cavitation formation in the liquid. For the syringe acceleration investigated in the current study, the cavitation bubble growth is mainly determined by both the magnitude and timing of the first acceleration peak that occurs about  $85 \mu\text{s}$  after the driving rod hits the plunger. Subsequent acceleration peaks have relatively small influence on the bubble dynamics, but can still enhance the bubble growth, especially for large bubbles with a long growth-collapse time.

The dynamics of cavitation bubble is dependent on the dimensionless variable  $\gamma = x_b(L + L_g)/R_{max}$ . During the administration of drug product with an autoinjector device, the liquid in the vicinity of the syringe bottom wall are subjected to the largest pressure variation, thus,

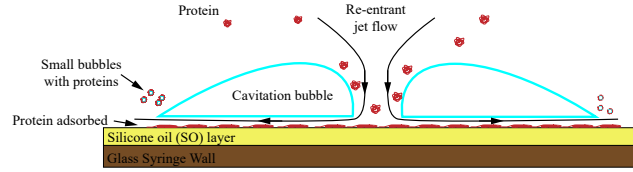


**Figure 4.17.** Schematic demonstrating the proposed protein aggregation process during the collapse of a cavitation bubble near the syringe wall.

most cavitation bubbles are described by a small  $\gamma$ . On the other hand, an increase in the maximum cavitation bubble size  $R_{max}$  also decreases  $\gamma$ , thus, the impedance effects of the wall are more prominent for large cavitation bubbles. Based on the simulation results, we propose the following pathway for protein aggregation induced by the collapse of cavitation bubbles near the syringe wall (Fig. 4.17): the acceleration of the bottom syringe wall creates an expansion wave propagating inside the liquid column and reflected by the top air-liquid interface and the syringe wall. The bubble grows under expansion waves and collapses when a strong enough compression wave reaches the bubble. The re-entrant jet forms on the bubble surface that is away from the wall with protein molecules focused inside the jet and pushed toward the syringe wall. The re-entrant jet also induces a stagnation point in the flow and spreads the protein molecules across the wall. Since for pre-filled glass syringes, the wall is usually coated with a thin layer of silicone oil for lubrication between the plunger and syringe, the protein molecules can adsorb to the silicone oil-liquid interface and form a protein adsorption layer on the syringe wall, leading to potential protein aggregation [22], [23], [27]. The silicone oil-free polymer-based syringes have been reported to be more resilient to protein aggregation compared to the silicone oil-lubricated glass syringes [22]. On the other hand, small bubbles with a high surface concentration are also released at the outer rim of the toroidal bubble, where the surface concentration may reach the saturation concentration and result in the formation of protein aggregates in the bulk [20]. High pressure on the order of 100 bar is generated when the toroidal bubble collapses to the minimum size, where hydroxyl radicals can be produced, which may oxidize the protein molecules.

For bubbles positioned away from the wall, cavitation bubbles are usually smaller and it also takes less time for the bubble to grow and collapse. The re-entrant jet has higher

velocity and the highest pressure is generated due to the jet impact on the bubble surface or the syringe wall. Protein molecules are also concentrated inside the jet and pushed toward the syringe wall but may not reach the syringe wall. The small bubbles with high a protein surface concentration are generated, which may lead to the protein aggregation in the bulk. The strain rate, or hydrodynamic shear, involved in the cavitation bubble collapse is typically in the order of  $10^6 \text{ s}^{-1}$  and lasts for  $\sim 10 \mu\text{s}$ , which may not be sufficient for protein aggregation.

In most of our simulations, cavitation bubbles do not touch the wall and there is a thin liquid film between the toroidal bubble and the syringe wall. But for very small  $\gamma$  ( $x_b \leq 0.005$  or  $\gamma \leq 0.13$ ), the toroid bubble touches to the wall and the bubble dynamics is also dependent on the three-phase (silicone oil-water-air) contact line. The motion of the contact line, which is dependent on the hydrophobicity and roughness of the surface, is also a possible source of protein aggregation [22], [27]. The number of nuclei and pre-existing bubbles are also important in the cavitation formation. The flow near the short-time cavitation bubbles is dominated by inertia. The bubble dynamics is hardly modified for varying liquid viscosity and surface tension. However, the presence of surfactant molecules will suppress the protein adsorption on the interfaces and reduce the chance of protein aggregation [107]. Furthermore, our simulations assume that an air gap is present on the top of the syringe and the syringe is placed vertically. If the top air gap is removed, or if the syringe is placed horizontally with air entrained at the center of the syringe, the plunger motion can potentially induce a compression pressure wave propagating from the syringe top. This pressure wave is usually stronger than the wave generated by the top air gap and can prevent the cavitation bubble formation [3].

## 4.6 Conclusion

We conducted 1D calculations as well as axisymmetric and 3D simulations to investigate the cavitation bubble dynamics during the needle insertion process that occurs upon activation of a spring-driven autoinjector device. The 1D calculations provide a good estimation of the bubble size but cannot include the effects of non-spherical collapse. The axisymmetric

simulation is validated against the bubble shape observed in experiments. The migration of protein molecules are demonstrated by using passive surrogate tracers positioned on the bubble surface. The effect of bubble distance from the wall, liquid column height, air gap pressure and nucleus size is investigated. The bubble size first slightly increases with the distance and then decreases, and it also increases with the liquid column height, decreases with the air gap pressure and increases with the nucleus size.

The strain rate in a cavitation bubble is  $\sim 10^6 \text{ s}^{-1}$  and lasts for  $\sim 10 \mu\text{s}$ , which is insufficient to induce protein aggregation. The main reason for aggregation is probably the migration of proteins toward the syringe wall surface and its adsorption to the silicone oil interface[23], which can be alleviated by adding surfactants [107]. The bubble collapse also releases small bubbles with high concentrations of proteins, potentially leading to protein aggregation in the bulk. A high pressure between 100 and 1000 bar is also observed, where hydroxyl radicals can be generated which may oxidize the protein molecules [78], [79]. The protein migration, re-entrant jet velocity and maximum liquid pressure are dependent on the dimensionless variable  $\gamma$ , which is the ratio of the distance of bubble center to the wall over the maximum bubble size. The jet velocity increases with  $\gamma$ , while the maximum pressure first decreases and then increases with  $\gamma$ . For bubble clouds, bubble coalescence can occur for bubbles that are very close to each other, leading to a larger cavitation bubble and generation of a larger peak pressure upon collapse.

Filling the syringes with lower liquid column height can reduce the pressure variation during the rod impact on the plunger, thus decreasing the likelihood of generation of large cavitation bubbles. When the driving rod hits the plunger, the pressure increase in the air gap impedes the cavitation bubble growth. Thus, the cavitation effects may be more prominent if the initial air gap size increases or the air gap is less compressed during the rod impact. The acceleration profile of the syringe features a large peak followed by an oscillatory acceleration of lower amplitudes. The pressure wave generated by the first peak is the cause for cavitation. Therefore, the cavitation can also be prevented by reducing the magnitude of the initial acceleration during the insertion process of the needle. Since protein aggregation induced by cavitation may be exacerbated by protein adsorption to the syringe wall, the properties of syringe wall (e.g., surface energy) are also important.

Thus, removing the silicone oil coating or changing the syringe inner wall surface material may also be helpful to reduce cavitation-induced protein aggregation. On the other hand, adding surfactants into the drug solution can mitigate the adsorption of protein molecules on air-liquid and silicone oil-liquid interfaces [107]. The motion of tracers in our simulation suggests that the protein molecules on the bubble surface can be concentrated on the re-entrant jet, subjected to adsorption on the syringe walls. The addition of surfactants can reduce the protein concentration on the bubble surfaces and thus decreases the amount of protein aggregation.

## 5. SUMMARY AND FUTURE WORK

### 5.1 Overview

We conducted experimentally validated high-fidelity simulations to study the liquid jet formation, liquid slosh and cavitation in an autoinjector. The study of the liquid jet is mostly focused on the fluid dynamics in a simplified geometry, providing limited information regarding to the autoinjectors. But the simulations of liquid slosh and cavitation are based on a syringe geometry and focus on the problems most relevant to pharmaceuticals. Because our study is based on analysis and simulations, the results do not directly address whether or not the protein aggregates are formed in the autoinjectors. However, these results provides insights on the most unfavorable conditions, where violent liquid slosh and cavitation are generated in syringe. The results can also guide future experiments to build controllable systems that emulate the flow of liquid slosh and cavitation in syringes.

### 5.2 Liquid jet due to acceleration-deceleration motion

Our study of the liquid jet mainly focuses on the fluid dynamics aspects. We investigated the liquid jet deformed from an initially concave meniscus inside a test tube that is impacted by a moving rod and slowly stopped by friction. For small deceleration time and liquid viscosity, the velocity of the contact line between the liquid and the wall is dominated by inertial effects and approximates the tube velocity. The jet velocity is mainly dependent on five dimensionless parameters: the Weber number ( $We$ ), the Ohnesorge number ( $Oh$ ), the Bond number ( $Bo$ ), dimensionless deceleration time ( $\tau_d$ ) and acceleration time ( $\tau_a$ ). We proposed a scaling law for the jet velocity without gravity effects, and provided a modified form to address the gravity effects in the small Bond number regime. The jet formation mechanism is different for small and large Bond numbers: at small  $Bo$ , the jet forms due to the focusing flow, while at large  $Bo$ , the jet is induced by the collapse of capillary waves. We use the critical Weber number  $We_c$  to evaluate the critical velocity for jet breakup, which exhibit a scaling with the Ohnesorge number and deceleration time.

### 5.3 Liquid slosh

The liquid slosh during the insertion process is investigated using 3D simulations. The simulations are validated against the ex-situ experiments, where the syringe kinematics and geometry emulates those of an autoinjector except that the drug solution is replaced by silicone oil. We carried out a parameter study by performing high-fidelity three-dimensional simulations with a similar setup to the real syringes. Typically, about  $\sim 0.3\%$  of liquids are subject to strain rate over  $10^4 \text{ s}^{-1}$  for  $\sim 30 \text{ ms}$ , which is not sufficient for substantial unfolding of proteins. The motion of air-liquid interface is considered the most possible reason for protein denaturation. The interfacial area and fluid volume subject to high strain rate decreases with the solution viscosity, increases with the air gap size, syringe velocity, tilt angle and syringe inner wall hydrophobicity, and hardly changes with the surface tension and liquid column height. High hydrodynamic strain rate usually resides near the syringe wall and bubbles.

### 5.4 Cavitation

Axisymmetric simulations are built to study the bubble dynamics at the start of the insertion process. The simulations show good agreement with the bubble shape observed in ex-situ experiments. When a cavitation bubble near the syringe wall collapses, protein molecules are focused in the re-entrant jet and then pushed toward the syringe wall. The stagnation flow after the bubble collapse also helps to spread the protein molecules across the wall, potentially leading to the protein adsorption and aggregation on the syringe inner wall. This migration of drug molecules is considered the most possible cause for protein denaturation and is more predominant for large bubbles with a small distance to the syringe wall. The maximum bubble radius decreases with the wall distance and air gap pressure and increases with liquid column height and nucleus size, while the jet velocity shows an opposite trend. High pressures can be generated when the re-entrant jet impacts the bubble surface or syringe wall, or when the bubble collapses to the minimum volume. The pressure generally shows non-monotonic dependencies on wall distance, liquid column height, air gap

pressure and nucleus size. Cavitation is an inertia-dominated process, therefore the liquid viscosity and surface tension hardly change the bubble dynamics.

The strain rate near a collapsing bubble is on the order of  $10^6 \text{ s}^{-1}$  and only lasts for  $\sim 10 \mu\text{s}$ , which is not sufficient to unfold a substantial amount of protein drugs. During the bubble collapse, small bubbles are also released, where the surface concentration of protein molecules can reach the saturation, inducing protein aggregates in the bulk.

We also build 3D simulations to study the bubble dynamics in a cavitation bubble cloud. The bubble-bubble interaction can impede bubble growth and collapse. However, bubbles too close to each other can coalesce and form a larger bubble, which can elicit a stronger pressure at the collapse. The highest pressure for a cavitation bubble cloud is up to 1000 bar, which is possible to generate hydroxyl radicals and oxidize the protein molecules.

## 5.5 Mitigation

Decreasing the air gap size can both mitigate the liquid slosh and cavitation formation. When the driving rod hits the plunger, the plunger can be slightly displaced and the pressure increases in the air gap can impede the cavitation bubble growth. Reducing the air gap size help to increase the pressure in air gap and thus prevent the cavitation generation. Similarly, the plunger displacement due to the impact of the driving rod can increase the air gap pressure and impede the cavitation formation. For a fixed dose, the effects of liquid slosh is reduced for larger liquid column height and smaller radius, while the mitigation of cavitation prefers syringes with smaller liquid column height. Thus, the optimal syringe radius and the liquid column height may depend on whether liquid slosh or cavitation is more important. The syringe kinematics plays a vital importance in both liquid slosh and cavitation. Cavitation formation can be mitigated by smoothing the first acceleration peak induced by the impact of the driving rod, which occurs about 0.1 ms after the rod impact. While the effects of liquid slosh can be reduced by decreasing the maximum speed of the syringe, which occurs about 2 ms after the rod impact.

The property of the syringe inner wall is also important for both liquid slosh and cavitation bubble dynamics. An increase of the wall hydrophobicity or an increase of the contact

angle can enhance the motion of the air-liquid interface during the liquid slosh. Wall hydrophobicity also stabilizes the bubbles attached to the wall and may introduce more nuclei for cavitation inception. On the other hand, when cavitation bubble collapses, protein molecules are pushed toward the wall and may interact with the silicone oil layer on the wall, where the effects of silicone oil lubrication need further investigation. The silicone oil droplets may be released due to the strong flow near the wall during the cavitation or liquid slosh process. Since the interfacial effects are considered an important reason for denaturation for both liquid slosh and cavitation, surfactants in the drug solution can help to mitigate the damage on protein molecules. Furthermore, the tilt angle of the syringe during the administration can enhance the liquid slosh. We recommend to administer the syringe vertically in line with gravity but this may be impractical due to ergonomic and human factor considerations.

## 5.6 Future work

In our simulations of cavitation bubble dynamics, we used passive tracers for illustrating the migration of protein molecules. But for better accuracy, the future work on both liquid slosh and cavitation can use certain transport equations to model the concentration of protein molecules and surfactants both in the bulk and on the interfaces. Most syringes in autoinjectors are lubricated with a thin silicone oil film, which is not considered in our current model. The thickness of silicone layer is much smaller than the flow length scale, which makes the computations challenging. Our current cavitation study only investigates the syringes placed vertically, which is easier to control. Further studies may work on syringe administered horizontally or tilted with a certain angle. The shape of the needle entry can also affect the cavitation bubble dynamics [3], which can be a topic for future research. The effects of heat transfer and mass transfer, such as vaporization, for cavitation bubbles can also be investigated in the future studies.

Our simulations provide insights on building and setting up future experiments. For example, our studies have suggest that the liquid slosh mainly occurs on the top of the syringe, while the cavitation occurs at the bottom of the syringe. Thus, if protein particles

attached to the syringe bottom are found, these particles are more likely to be generated by the cavitation bubbles. If more protein aggregates are found on the top region of liquid solution or the syringe wall, then liquid slosh may be the primary reason for the protein aggregation. Future experiments may also reproduce a similar flow environment, such as the shear condition and flow patterns, to determine whether protein molecules are denatured in autoinjectors and the corresponding mechanism.

## REFERENCES

- [1] S. Wray, R. Armstrong, C. Herrman, J. Calkwood, M. Cascione, E. Watsky, B. Hayward, B. Mercer, and F. Dangond, “Results from the single-use autoinjector for self-administration of subcutaneous interferon beta-1a in patients with relapsing multiple sclerosis (mosaic) study,” *Expert opinion on drug delivery*, vol. 8, no. 12, pp. 1543–1553, 2011.
- [2] I. Thompson and J. Lange, “Pen and autoinjector drug delivery devices,” in *Sterile product development*, Springer, 2013, pp. 331–356.
- [3] J.-C. Veilleux and J. E. Shepherd, “Pressure and stress transients in autoinjector devices,” *Drug delivery and translational research*, vol. 8, no. 5, pp. 1238–1253, 2018.
- [4] F. M. Insights, “Auto-injectors market: Rising incidence of anaphylaxis attack among the adult population expected to elevate the demand for auto-injectors: Global industry analysis and opportunity assessment 2016-2026,” *Tech. rep.*, 2017. [Online]. Available: <https://www.futuremarketinsights.com/reports/auto-injectors-market>.
- [5] C. Thomas and D. Geer, “Effects of shear on proteins in solution,” *Biotechnol. Lett.*, vol. 33, no. 3, pp. 443–456, 2011, ISSN: 0141-5492.
- [6] X. Zhong, T. Guo, P. Vlachos, J. Veilleux, G. Shi, D. Collins, and A. Ardekani, “An experimentally validated dynamic model for spring-driven autoinjectors.,” *International Journal of Pharmaceutics*, pp. 120 008–120 008, 2020.
- [7] D. L. French and J. J. Collins, “Advances in parenteral injection devices and aids,” *Pharmaceutical Dosage Forms, Parenteral Medications*, vol. 3, pp. 71–75, 2016.
- [8] R. Ferrandiz, “Cartridge vs syringe auto-injectors: A misleading discussion,” *On the WWW*.<https://www.emerade.com/hcp/articles/cartridge-vs-syringe-auto-injectors>. Accessed March 17, 2021, 2014.
- [9] J. T. Jørgensen, J. Rømsing, M. Rasmussen, J. Møller-Sonnergaard, L. Vang, and L. Musæus, “Pain assessment of subcutaneous injections,” *Annals of Pharmacotherapy*, vol. 30, no. 7-8, pp. 729–732, 1996.
- [10] L. Li, S. Kumar, P. M. Buck, C. Burns, J. Lavoie, S. K. Singh, N. W. Warne, P. Nichols, N. Luksha, and D. Boardman, “Concentration dependent viscosity of monoclonal antibody solutions: Explaining experimental behavior in terms of molecular properties,” *Pharmaceutical research*, vol. 31, no. 11, pp. 3161–3178, 2014.

- [11] S. Yadav, S. J. Shire, and D. S. Kalonia, "Factors affecting the viscosity in high concentration solutions of different monoclonal antibodies," *Journal of pharmaceutical sciences*, vol. 99, no. 12, pp. 4812–4829, 2010.
- [12] K. D. Wiley, "Clean vs sterile," *Materials Today*, vol. 16, no. 6, pp. 249–250, 2013.
- [13] S. Kiese, A. Papppenberger, W. Friess, and H.-C. Mahler, "Shaken, not stirred: Mechanical stress testing of an igg1 antibody," *J. Pharm. Sci.*, vol. 97, no. 10, pp. 4347–4366, 2008.
- [14] T. W. Randolph, E. Schiltz, D. Sederstrom, D. Steinmann, O. Mozziconacci, C. Schöneich, E. Freund, M. S. Ricci, J. F. Carpenter, and C. S. Lengsfeld, "Do not drop: Mechanical shock in vials causes cavitation, protein aggregation, and particle formation," *Journal of pharmaceutical sciences*, vol. 104, no. 2, pp. 602–611, 2015.
- [15] A. S. Rosenberg, "Effects of protein aggregates: An immunologic perspective," *The AAPS journal*, vol. 8, no. 3, E501–E507, 2006.
- [16] P. Frei, B. Benacerraf, and G. Thorbecke, "Phagocytosis of the antigen, a crucial step in the induction of the primary response," *Proceedings of the National Academy of Sciences of the United States of America*, vol. 53, no. 1, p. 20, 1965.
- [17] E. M. Moussa, J. P. Panchal, B. S. Moorthy, J. S. Blum, M. K. Joubert, L. O. Narhi, and E. M. Topp, "Immunogenicity of therapeutic protein aggregates," *Journal of pharmaceutical sciences*, vol. 105, no. 2, pp. 417–430, 2016.
- [18] A. Braun, L. Kwee, M. A. Labow, and J. Alsenz, "Protein aggregates seem to play a key role among the parameters influencing the antigenicity of interferon alpha (ifn- $\alpha$ ) in normal and transgenic mice," *Pharmaceutical research*, vol. 14, no. 10, pp. 1472–1478, 1997.
- [19] S. Charm and B. Wong, "Enzyme inactivation with shearing," *Biotechnology and Bioengineering*, vol. 12, no. 6, pp. 1103–1109, 1970.
- [20] G. L. Lin, J. A. Pathak, D. H. Kim, M. Carlson, V. Rigüero, Y. J. Kim, J. S. Buff, and G. G. Fuller, "Interfacial dilatational deformation accelerates particle formation in monoclonal antibody solutions," *Soft Matter*, vol. 12, no. 14, pp. 3293–3302, 2016.
- [21] K. Nakanishi, T. Sakiyama, and K. Imamura, "On the adsorption of proteins on solid surfaces, a common but very complicated phenomenon," *Journal of bioscience and bioengineering*, vol. 91, no. 3, pp. 233–244, 2001.

- [22] E. Krayukhina, K. Tsumoto, S. Uchiyama, and K. Fukui, “Effects of syringe material and silicone oil lubrication on the stability of pharmaceutical proteins,” *Journal of pharmaceutical sciences*, vol. 104, no. 2, pp. 527–535, 2015.
- [23] R. Dandekar and A. M. Ardekani, “Monoclonal antibody aggregation near silicone oil–water interfaces,” *Langmuir*, 2021.
- [24] J. S. Bee, J. L. Stevenson, B. Mehta, J. Svitel, J. Pollastrini, R. Platz, E. Freund, J. F. Carpenter, and T. W. Randolph, “Response of a concentrated monoclonal antibody formulation to high shear,” *Biotechnology and bioengineering*, vol. 103, no. 5, pp. 936–943, 2009.
- [25] J. Dobson, A. Kumar, L. F. Willis, R. Tuma, D. R. Higazi, R. Turner, D. C. Lowe, A. E. Ashcroft, S. E. Radford, N. Kapur, *et al.*, “Inducing protein aggregation by extensional flow,” *Proceedings of the National Academy of Sciences*, vol. 114, no. 18, pp. 4673–4678, 2017.
- [26] L. Xing, Y. Li, and T. Li, “Local concentrating, not shear stress, that may lead to possible instability of protein molecules during syringe injection: A fluid dynamic study with two-phase flow model,” *PDA journal of pharmaceutical science and technology*, vol. 73, no. 3, pp. 260–275, 2019.
- [27] A. Gerhardt, N. R. McGraw, D. K. Schwartz, J. S. Bee, J. F. Carpenter, and T. W. Randolph, “Protein aggregation and particle formation in prefilled glass syringes,” *Journal of pharmaceutical sciences*, vol. 103, no. 6, pp. 1601–1612, 2014.
- [28] J.-C. Veilleux and J. E. Shepherd, “Impulsive motion in a cylindrical fluid-filled tube terminated by a converging section,” *Journal of Pressure Vessel Technology*, vol. 141, no. 2, 2019.
- [29] J. Eggers and E. Villermaux, “Physics of liquid jets,” *Rep. Prog. Phys.*, vol. 71, no. 3, p. 036 601, 2008.
- [30] A. Woodcock, C. Kientzler, A. Arons, and D. Blanchard, “Giant condensation nuclei from bursting bubbles,” *Nature*, vol. 172, no. 4390, p. 1144, 1953.
- [31] E. Ghabache and T. Séon, “Size of the top jet drop produced by bubble bursting,” *Phys. Rev. Fluids*, vol. 1, no. 5, p. 051 901, 2016.
- [32] A. M. Gañán-Calvo, “Revision of bubble bursting: Universal scaling laws of top jet drop size and speed,” *Phys. Rev. Lett.*, vol. 119, no. 20, p. 204 502, 2017.

- [33] L. Deike, E. Ghabache, G. Liger-Belair, A. K. Das, S. Zaleski, S. Popinet, and T. Séon, “Dynamics of jets produced by bursting bubbles,” *Phys. Rev. Fluids*, vol. 3, no. 1, p. 013 603, 2018.
- [34] A. M. Gañán-Calvo, “Scaling laws of top jet drop size and speed from bubble bursting including gravity and inviscid limit,” *Phys. Rev. Fluids*, vol. 3, no. 9, p. 091 601, 2018.
- [35] C.-Y. Lai, J. Eggers, and L. Deike, “Bubble bursting: Universal cavity and jet profiles,” *Phys. Rev. Lett.*, vol. 121, no. 14, p. 144 501, 2018.
- [36] J. M. Gordillo and J. Rodríguez-Rodríguez, “Comment on “revision of bubble bursting: Universal scaling laws of top jet drop size and speed”,” *Phys. Rev. Lett.*, vol. 121, p. 269 401, 26 Dec. 2018. DOI: [10.1103/PhysRevLett.121.269401](https://doi.org/10.1103/PhysRevLett.121.269401). [Online]. Available: <https://link.aps.org/doi/10.1103/PhysRevLett.121.269401>.
- [37] J. Gordillo and J. Rodríguez-Rodríguez, “Capillary waves control the ejection of bubble bursting jets,” *J. Fluid Mech.*, vol. 867, pp. 556–571, 2019.
- [38] A. M. Ganán-Calvo and J. M. Lopez-Herrera, “Capillary soft singularities and ejection: Application to the physics of bubble bursting,” *arXiv preprint arXiv:1911.08844*, 2019.
- [39] M. Utsumi, “Low-gravity propellant slosh analysis using spherical coordinates,” *J. Fluids Struct.*, vol. 12, no. 1, pp. 57–83, 1998.
- [40] A. Antkowiak, N. Bremond, S. Le Dizès, and E. Villiermaux, “Short-term dynamics of a density interface following an impact,” *J. Fluid Mech.*, vol. 577, pp. 241–250, 2007.
- [41] A. Kiyama, Y. Tagawa, K. Ando, and M. Kameda, “Effects of a water hammer and cavitation on jet formation in a test tube,” *J. Fluid Mech.*, vol. 787, pp. 224–236, 2016.
- [42] H. Onuki, Y. Oi, and Y. Tagawa, “Microjet generator for highly viscous fluids,” *Phys. Rev. Appl.*, vol. 9, no. 1, p. 014 035, 2018.
- [43] S. Popinet, “An accurate adaptive solver for surface-tension-driven interfacial flows,” *J. Comput. Phys.*, vol. 228, no. 16, pp. 5838–5866, 2009.
- [44] S. Afkhami, J. Buongiorno, A. Guion, S. Popinet, Y. Saade, R. Scardovelli, and S. Zaleski, “Transition in a numerical model of contact line dynamics and forced dewetting,” *J. Comput. Phys.*, vol. 374, pp. 1061–1093, 2018.
- [45] J. Bostwick and P. Steen, “Dynamics of sessile drops. part 1. inviscid theory,” *J. Fluid Mech.*, vol. 760, pp. 5–38, 2014.

- [46] Y. Chen and P. Steen, “Dynamics of inviscid capillary breakup: Collapse and pinchoff of a film bridge,” *J. Fluid Mech.*, vol. 341, pp. 245–267, 1997, ISSN: 0022-1120.
- [47] R. F. Day, E. J. Hinch, and J. R. Lister, “Self-similar capillary pinchoff of an inviscid fluid,” *Phys. Rev. Lett.*, vol. 80, no. 4, pp. 704–707, 1998, ISSN: 0031-9007.
- [48] J. Eggers, “Universal pinching of 3d axisymmetric free-surface flow,” *Phys. Rev. Lett.*, vol. 71, no. 21, p. 3458, 1993.
- [49] S. Wilson, “The slow dripping of a viscous fluid,” *J. Fluid Mech.*, vol. 190, pp. 561–570, 1988, ISSN: 0022-1120.
- [50] R. Mathaes, A. Koulov, S. Joerg, and H.-C. Mahler, “Subcutaneous injection volume of biopharmaceuticals—pushing the boundaries,” *Journal of pharmaceutical sciences*, vol. 105, no. 8, pp. 2255–2259, 2016.
- [51] M. X. Yang, B. Shenoy, M. Disttler, R. Patel, M. McGrath, S. Pechenov, and A. L. Margolin, “Crystalline monoclonal antibodies for subcutaneous delivery,” *Proceedings of the National Academy of Sciences*, vol. 100, no. 12, pp. 6934–6939, 2003.
- [52] H.-C. Mahler, R. Müller, W. Frieß, A. Delille, and S. Matheus, “Induction and analysis of aggregates in a liquid igg1-antibody formulation,” *European journal of pharmaceuticals and biopharmaceutics*, vol. 59, no. 3, pp. 407–417, 2005.
- [53] I. B. Bekard, P. Asimakis, J. Bertolini, and D. E. Dunstan, “The effects of shear flow on protein structure and function,” *Biopolymers*, vol. 95, no. 11, pp. 733–745, 2011.
- [54] V. Sluzky, A. M. Klibanov, and R. Langer, “Mechanism of insulin aggregation and stabilization in agitated aqueous solutions,” *Biotechnology and bioengineering*, vol. 40, no. 8, pp. 895–903, 1992.
- [55] H. Baldascini and D. B. Janssen, “Interfacial inactivation of epoxide hydrolase in a two-liquid-phase system,” *Enzyme and Microbial Technology*, vol. 36, no. 2-3, pp. 285–293, 2005.
- [56] S. R. Brych, Y. R. Gokarn, H. Hultgen, R. J. Stevenson, R. Rajan, and M. Matsumura, “Characterization of antibody aggregation: Role of buried, unpaired cysteines in particle formation,” *Journal of pharmaceutical sciences*, vol. 99, no. 2, pp. 764–781, 2010.
- [57] J. Roenby, H. Bredmose, and H. Jasak, “A computational method for sharp interface advection,” *Royal Society open science*, vol. 3, no. 11, p. 160405, 2016.
- [58] R. Mead-Hunter, A. J. King, and B. J. Mullins, “Plateau rayleigh instability simulation,” *Langmuir*, vol. 28, no. 17, pp. 6731–6735, 2012.

- [59] A. Q. Raeini, M. J. Blunt, and B. Bijeljic, “Modelling two-phase flow in porous media at the pore scale using the volume-of-fluid method,” *Journal of Computational Physics*, vol. 231, no. 17, pp. 5653–5668, 2012.
- [60] P. Koukouvini, M. Gavaises, O. Supponen, and M. Farhat, “Simulation of bubble expansion and collapse in the vicinity of a free surface,” *Physics of Fluids*, vol. 28, no. 5, p. 052103, 2016.
- [61] S. Amin, G. V. Barnett, J. A. Pathak, C. J. Roberts, and P. S. Sarangapani, “Protein aggregation, particle formation, characterization & rheology,” *Current Opinion in Colloid & Interface Science*, vol. 19, no. 5, pp. 438–449, 2014.
- [62] M. M. Castellanos, J. A. Pathak, and R. H. Colby, “Both protein adsorption and aggregation contribute to shear yielding and viscosity increase in protein solutions,” *Soft Matter*, vol. 10, no. 1, pp. 122–131, 2014.
- [63] V. Sharma, A. Jaishankar, Y.-C. Wang, and G. H. McKinley, “Rheology of globular proteins: Apparent yield stress, high shear rate viscosity and interfacial viscoelasticity of bovine serum albumin solutions,” *Soft matter*, vol. 7, no. 11, pp. 5150–5160, 2011.
- [64] J. U. Brackbill, D. B. Kothe, and C. Zemach, “A continuum method for modeling surface tension,” *Journal of computational physics*, vol. 100, no. 2, pp. 335–354, 1992.
- [65] H. Ding, P. D. Spelt, and C. Shu, “Diffuse interface model for incompressible two-phase flows with large density ratios,” *Journal of Computational Physics*, vol. 226, no. 2, pp. 2078–2095, 2007.
- [66] J.-L. Guermond and L. Quartapelle, “A projection fem for variable density incompressible flows,” *Journal of Computational Physics*, vol. 165, no. 1, pp. 167–188, 2000.
- [67] G. Tryggvason, “Numerical simulations of the rayleigh-taylor instability,” *Journal of Computational Physics*, vol. 75, no. 2, pp. 253–282, 1988.
- [68] Z.-Q. Wen, A. Vance, F. Vega, X. Cao, B. Eu, and R. Schulthesis, “Distribution of silicone oil in prefilled glass syringes probed with optical and spectroscopic methods,” *PDA Journal of Pharmaceutical Science and Technology*, vol. 63, no. 2, pp. 149–158, 2009.
- [69] A. Eifert, D. Paulssen, S. N. Varanakkottu, T. Baier, and S. Hardt, “Simple fabrication of robust water-repellent surfaces with low contact-angle hysteresis based on impregnation,” *Advanced Materials Interfaces*, vol. 1, no. 3, p. 1300138, 2014.

- [70] A. F. Azarbayjani, A. Jouyban, and S. Y. Chan, “Impact of surface tension in pharmaceutical sciences,” *Journal of pharmacy & pharmaceutical sciences*, vol. 12, no. 2, pp. 218–228, 2009.
- [71] A. Ooi, J. Martin, J. Soria, and M. S. Chong, “A study of the evolution and characteristics of the invariants of the velocity-gradient tensor in isotropic turbulence,” *Journal of Fluid Mechanics*, vol. 381, pp. 141–174, 1999.
- [72] J. S. Lee, R. Dylla-Spears, N. P. Teclemariam, and S. J. Muller, “Microfluidic four-roll mill for all flow types,” *Applied physics letters*, vol. 90, no. 7, p. 074 103, 2007.
- [73] C. B. da Silva and J. C. Pereira, “Invariants of the velocity-gradient, rate-of-strain, and rate-of-rotation tensors across the turbulent/nonturbulent interface in jets,” *Physics of fluids*, vol. 20, no. 5, p. 055 101, 2008.
- [74] A. Hawe, M. Wiggenghorn, M. van de Weert, J. H. Garbe, H.-c. Mahler, and W. Jiskoot, “Forced degradation of therapeutic proteins,” *Journal of pharmaceutical sciences*, vol. 101, no. 3, pp. 895–913, 2012.
- [75] J. V. Nauman, P. G. Campbell, F. Lanni, and J. L. Anderson, “Diffusion of insulin-like growth factor-i and ribonuclease through fibrin gels,” *Biophysical journal*, vol. 92, no. 12, pp. 4444–4450, 2007.
- [76] Y. Zhang, T. Guo, P. Vlachos, and A. M. Ardekani, “Velocity scaling and breakup criteria for jets formed due to acceleration and deceleration process,” *Physical Review Fluids*, vol. 5, no. 7, p. 074 003, 2020.
- [77] Y. Zhang, D. Han, Z. Dou, J.-C. Veilleux, G. H. Shi, D. S. Collins, P. P. Vlachos, and A. M. Ardekani, “The interface motion and hydrodynamic shear of the liquid slosh in syringes,” *Pharmaceutical Research*, pp. 1–19, 2021.
- [78] P. Riesz, D. Berdahl, and C. Christman, “Free radical generation by ultrasound in aqueous and nonaqueous solutions.,” *Environmental Health Perspectives*, vol. 64, pp. 233–252, 1985.
- [79] P. Riesz and T. Kondo, “Free radical formation induced by ultrasound and its biological implications,” *Free Radical Biology and Medicine*, vol. 13, no. 3, pp. 247–270, 1992.
- [80] M. Duerkop, E. Berger, A. Dürauer, and A. Jungbauer, “Influence of cavitation and high shear stress on hsa aggregation behavior,” *Engineering in life sciences*, vol. 18, no. 3, pp. 169–178, 2018.

- [81] T. Torisu, T. Maruno, Y. Hamaji, T. Ohkubo, and S. Uchiyama, “Synergistic effect of cavitation and agitation on protein aggregation,” *Journal of pharmaceutical sciences*, vol. 106, no. 2, pp. 521–529, 2017.
- [82] C. Li, F. Yang, Y. Huang, C. Huang, K. Zhang, L. Yan, *et al.*, “Comparison of hydrodynamic and ultrasonic cavitation effects on soy protein isolate functionality,” *Journal of Food Engineering*, vol. 265, p. 109 697, 2020.
- [83] J. Chandrapala, B. Zisu, M. Palmer, S. Kentish, and M. Ashokkumar, “Effects of ultrasound on the thermal and structural characteristics of proteins in reconstituted whey protein concentrate,” *Ultrasonics sonochemistry*, vol. 18, no. 5, pp. 951–957, 2011.
- [84] T. Perevozchikova, H. Nanda, D. P. Nesta, and C. J. Roberts, “Protein adsorption, desorption, and aggregation mediated by solid-liquid interfaces,” *Journal of pharmaceutical sciences*, vol. 104, no. 6, pp. 1946–1959, 2015.
- [85] A. S. Sediq, R. B. van Duijvenvoorde, W. Jiskoot, and M. R. Nejadnik, “No touching! abrasion of adsorbed protein is the root cause of subvisible particle formation during stirring,” *Journal of pharmaceutical sciences*, vol. 105, no. 2, pp. 519–529, 2016.
- [86] M. N. Islam, M. Zhang, and B. Adhikari, “The inactivation of enzymes by ultrasound—a review of potential mechanisms,” *Food Reviews International*, vol. 30, no. 1, pp. 1–21, 2014.
- [87] Y. Lentz, T. Anchordoquy, and C. Lengsfeld, “Dna acts as a nucleation site for transient cavitation in the ultrasonic nebulizer,” *Journal of pharmaceutical sciences*, vol. 95, no. 3, pp. 607–619, 2006.
- [88] M. Duerkop, E. Berger, A. Dürauer, and A. Jungbauer, “Impact of cavitation, high shear stress and air/liquid interfaces on protein aggregation,” *Biotechnology journal*, vol. 13, no. 7, p. 1 800 062, 2018.
- [89] C. E. Brennen, *Cavitation and bubble dynamics*. Cambridge University Press, 2014.
- [90] A. Vogel, W. Lauterborn, and R. Timm, “Optical and acoustic investigations of the dynamics of laser-produced cavitation bubbles,” *J. Fluid Mech*, vol. 206, pp. 299–338, 1989.
- [91] J. R. Blake and D. Gibson, “Cavitation bubbles near boundaries,” *Annual review of fluid mechanics*, vol. 19, no. 1, pp. 99–123, 1987.

- [92] Y. Tomita, P. Robinson, R. Tong, and J. Blake, “Growth and collapse of cavitation bubbles near a curved rigid boundary,” *Journal of Fluid Mechanics*, vol. 466, p. 259, 2002.
- [93] O. V. Voinov and V. Voinov, “Numerical method of calculating nonstationary motions of an ideal incompressible fluid with free surfaces,” in *Doklady Akademii Nauk*, Russian Academy of Sciences, vol. 221, 1975, pp. 559–562.
- [94] K. Yasui, J. Lee, T. Tuziuti, A. Towata, T. Kozuka, and Y. Iida, “Influence of the bubble-bubble interaction on destruction of encapsulated microbubbles under ultrasound,” *The Journal of the Acoustical Society of America*, vol. 126, no. 3, pp. 973–982, 2009.
- [95] M. H. Chaudhry, *Applied hydraulic transients*. Springer, 1979.
- [96] Z. Dou, J. Eshraghi, T. Guo, J.-C. Veilleux, K. H. Duffy, G. H. Shi, D. S. Collins, A. M. Ardekani, and P. P. Vlachos, “Performance characterization of spring actuated autoinjector devices for emgality and aimovig,” *Current Medical Research and Opinion*, vol. 36, no. 8, pp. 1343–1354, 2020.
- [97] D. F. Gaitan, L. A. Crum, C. C. Church, and R. A. Roy, “Sonoluminescence and bubble dynamics for a single, stable, cavitation bubble,” *The Journal of the Acoustical Society of America*, vol. 91, no. 6, pp. 3166–3183, 1992.
- [98] J. B. Keller and M. Miksis, “Bubble oscillations of large amplitude,” *The Journal of the Acoustical Society of America*, vol. 68, no. 2, pp. 628–633, 1980.
- [99] P. Bogacki and L. F. Shampine, “A 3 (2) pair of runge-kutta formulas,” *Applied Mathematics Letters*, vol. 2, no. 4, pp. 321–325, 1989.
- [100] S. Popinet, “A quadtree-adaptive multigrid solver for the serre–green–naghdi equations,” *Journal of Computational Physics*, vol. 302, pp. 336–358, 2015.
- [101] D. Fuster and S. Popinet, “An all-mach method for the simulation of bubble dynamics problems in the presence of surface tension,” *Journal of Computational Physics*, vol. 374, pp. 752–768, 2018.
- [102] S. Fujikawa and T. Akamatsu, “Effects of the non-equilibrium condensation of vapour on the pressure wave produced by the collapse of a bubble in a liquid,” *Journal of Fluid Mechanics*, vol. 97, no. 3, pp. 481–512, 1980.
- [103] Q. Wang and J. Blake, “Non-spherical bubble dynamics in a compressible liquid. part 1. travelling acoustic wave,” *Journal of Fluid Mechanics*, vol. 659, pp. 191–224, 2010.

- [104] A. Baszkin, M. Boissonnade, A. Kamyshny, and S. Magdassi, “Native and hydrophobically modified human immunoglobulin g at the air/water interface: Sequential and competitive adsorption,” *Journal of colloid and interface science*, vol. 239, no. 1, pp. 1–9, 2001.
- [105] E. Johnsen and T. Colonius, “Numerical simulations of non-spherical bubble collapse,” *Journal of fluid mechanics*, vol. 629, p. 231, 2009.
- [106] G. L. Chahine and R. Duraiswami, “Dynamical interactions in a multi-bubble cloud,” *Journal of Fluids Engineering-transactions of The Asme*, vol. 114, no. 4, pp. 680–686, 1992.
- [107] A. Kannan, I. C. Shieh, D. L. Leiske, and G. G. Fuller, “Monoclonal antibody interfaces: Dilatation mechanics and bubble coalescence,” *Langmuir*, vol. 34, no. 2, pp. 630–638, 2018.

# VITA

## EDUCATION

Ph.D. in Mechanical Engineering, Purdue University, West Lafayette, Aug. 2016 – Present

B.S. in Mechanical Engineering, Purdue University, West Lafayette, Aug. 2014 – May 2016

B.S. in Mechanical Engineering, Jiao Tong University, Shanghai, Aug. 2012 – May 2014

## WORK EXPERIENCE

Software Engineer, TigerGraph, Redwood City, CA May 2020 – Aug. 2020

Software Engineer, TigerGraph, Redwood City, CA May 2019 – Aug. 2019

Research Assistant, Purdue University, West Lafayette, IN Aug. 2016 – Present

## HONORS

Andrew's fellowship, Purdue University, Aug. 2016

National scholarship, Shanghai Jiao Tong University, Aug. 2012

## PUBLICATIONS

**Zhang, Y.**, Han, D., Dou, Z., Veilleux, J.C., Shi, G.H., Collins, D.S., Vlachos, P.P. and Ardekani, A.M., 2021. The Interface Motion and Hydrodynamic Shear of the Liquid Slosh in Syringes. *Pharmaceutical Research*, 38(2), pp.257-275.

Gopinath, A., Tamayo, J., **Zhang, Y.**, Ardekani, A.M. and Patteson, A.E., 2020. Swarming bacterial fronts: Dynamics and morphology of active swarm interfaces propagating through passive frictional domains. preprint available at <https://www.biorxiv.org/content/10.1101/2020.04.18.048637v3>

**Zhang, Y.**, Guo, T., Vlachos, P. and Ardekani, A., 2018. Dynamics of liquid-air interface following vertical acceleration-deceleration motion. *Bulletin of the American Physical Society*, 63.

**Zhang, Y.**, Li, G. and Ardekani, A.M., 2018. Reduced viscosity for flagella moving in a solution of long polymer chains. *Physical Review Fluids*, 3(2), p.023101.

**Zhang, Y.**, 2017. Simulation of Oil Droplets Through Porous Media Using Dissipative Particle D. *The Journal of Purdue Undergraduate Research*, 7(1), p.25.